MULTI-BODY MISSION DESIGN IN THE SATURNIAN SYSTEM WITH EMPHASIS ON ENCELADUS ACCESSIBILITY

A Thesis

Submitted to the Faculty

of

Purdue University

by

Todd S. Brown

In Partial Fulfillment of the

Requirements for the Degree

of

Master of Science

December 2008

Purdue University

West Lafayette, Indiana

"My Guide and I crossed over and began
to mount that little known and lightless road
to ascend into the shining world again.
He first, I second, without thought of rest
we climbed the dark until we reached the point
where a round opening brought in sight the blest
and beauteous shining of the Heavenly cars.
And we walked out once more beneath the Stars."

-Dante Alighieri (*The Inferno*)

Like Dante, I could not have followed the path to this point in my life without the tireless aid of a guiding hand. I owe all my thanks to the boundless support I have received from my parents. They have never sacrificed an opportunity to help me to grow into a better person, and all that I know of success, I learned from them. I'm eternally grateful that their love and nurturing, and I'm also grateful that they instilled a passion for learning in me, that I carry to this day. I also thank my sister, Alayne, who has always been the role-model that I strove to emulate.

ACKNOWLEDGMENTS

I would like to acknowledge and extend my thanks my academic advisor, Professor Kathleen Howell, for both pointing me in the right direction and giving me the freedom to approach my research at my own pace. Prof. Howell was the first person to introduce me to the Enceladus mission design problem that I have wholeheartedly investigated for the last two years. I selected Purdue for my graduate study largely because I was drawn to Prof. Howell's research, and I have relished the opportunities that I have been given to investigate the restricted three-body problem and other astrodynamics topics here at Purdue.

I would also like to acknowledge the financial support that has been instrumental in my ability to pursue graduate study at Purdue. I would like to thank John L. and Patricia R. Rich for the scholarship that supported my first year of study at Purdue University. My graduate study was also supported by the Ross Fellowship I received from the Purdue University Graduate School. An acknowledgment is also owed to the Purdue Aeronautics and Astronautics Engineering department for the teaching assistantship they provided me during my first year at Purdue.

I would also like to thank Rune and Barbara Eliasen for their investment in visualization technology for the Aeronautical and Astronautical Engineering department at Purdue. It has been a wonderful experience to work in the Rune and Barbara Eliasen Visualization Laboratory during the last two years, and I thank them both for their financial support of my graduate study. I consider myself inordinately fortunate to have been given the opportunity to use cutting-edge visualization technology on a daily basis for my research. Indeed, many of the plots in my thesis are a direct result of the computational capabilities of Eliasen Visualization Laboratory.

I would also like to acknowledge the tireless support of my friends and fellow graduate students in Prof. Howell's research group: Diane Craig Davis, Dawn Gordon, Daniel Grebow, Aurelie Heritier, Lucia Irrgang, Masaki Kakoi, Amanda Knutson, Lindsay Millard, Zubin Olikara, Martin Ozimek, Chris Patterson, Tom Pavlak, Raoul Rausch, Wayne Schlei, Cody Short, Mar Vaquero, Matt Vavrina, and Geoff Wawrzyniak. Every one of the members of our research group has aided me in my research during the last two years. My research group friends and colleagues shouldered the majority of the questions and quandaries that I encountered during the course of my research at Purdue.

TABLE OF CONTENTS

Page

Page

LIST OF TABLES

LIST OF FIGURES

Figure Page

Figure Page

Figure Page

ABSTRACT

Brown, Todd S. M.S., Purdue University, December, 2008. Multi-Body Mission Design in the Saturnian System with Emphasis on Enceladus Accessibility. Major Professor: Kathleen C. Howell.

Recent discoveries regarding Saturn's moon, Enceladus, have transformed the small icy moon into one of the most desirable solar system destinations for future robotic reconnaissance. In designing a mission to Enceladus, the insignificant size of Enceladus and its close proximity to Saturn combine to create a remarkably challenging multi-body problem. This investigation offers an overview of three key aspects of the Enceladus transfer problem including: the design of an Enceladus science orbit, the design of Saturnian orbits that permit periodic encounters with Enceladus and additional Saturnian moons, and the design of gravity-assist flyby sequences in the Saturnian system involving five of Saturn's most massive moons: Enceladus, Tethys, Dione, Rhea, and Titan. Although focused specifically on the design problem associated with supporting a mission in the Saturnian system, the Enceladus transfer problem is analyzed from a multi-body perspective. A substantial portion of this investigation involves the application of the Circular Restricted Three-Body Problem (CR3BP) to the Saturnian system, though the dynamics of the Saturnian system are also investigated using a six-body dynamical model. A technique is introduced to design a sequence of gravity-assist flybys by incorporating multiple gravity fields and applying a scheme that adjusts only one initial variable to yield a trajectory with multiple flybys. The capabilities of the trajectory design algorithm are demonstrated through the design of specific gravity-assist flyby sequences that are used to reduce the orbital energy of a spacecraft in a large Saturnian orbit to an energy level that is closer to the level of Enceladus' Saturnian orbit.

1. INTRODUCTION

Of all the countless small bodies in the solar system – be they comets, asteroids, planets, dwarf planets, or moons – Enceladus, the diminutive moon of Saturn, may initially seem to be one of the most insignificant. Enceladus remains unremarkable in its size, composition, and location. However, even prior to the first forays into the outer solar system by Earth-born robotic explorers, Enceladus piqued the interest of astronomers who noted the moon's unusually high visual albedo (or surface reflectivity) [1] and who also concluded that Enceladus' reflectance spectrum was dominated by one of the most enticing substances in the solar system: pure water ice [2]. Close observations of Enceladus in recent years [3], using a variety of instruments onboard interplanetary spacecraft, have catapulted the small moon from the role of an astronomical curiosity to one of the few select places in the solar system that apparently support the conditions where life, as we know it, *could* both survive and thrive. With the possibility of life-sustaining conditions on Enceladus, there has been a strong push from the scientific community for NASA to send another robotic spacecraft to perform an in-depth, and preferably dedicated, study of the water-rich moon [4, 5]. However, despite the immense interest in Enceladus from the scientific community, the complexities and expense to orbit or land on Enceladus requires a mission that would be arguably the most ambitious robotic mission NASA has yet undertaken.

Enceladus is perched precariously inside the tenuous outer rings of Saturn, barely beyond Saturn's main rings, and still deep within the gravity well of Saturn. Any robotic spacecraft entering the Saturnian system must lose an enormous amount of orbital energy relative to Saturn to approach Enceladus at a sufficiently low relative velocity to allow for orbital insertion or low speed flyby reconnaissance. The vast reduction in orbital energy relative to Saturn could potentially be accomplished with a propulsive maneuver

of extremely large magnitude, but a more practical solution includes some use of gravity-assist flybys of Saturn's moons as a means to accomplish a propellant-free reduction in orbital energy at the cost of an increased time-of-flight. From the viewpoint of a spacecraft mission designer, the Saturnian system thus becomes an astrodynamical laboratory; it is ripe with the challenges and opportunities usually encountered in interplanetary mission design, though occurring on a much smaller scale and shorter time interval.

1.1 Problem Definition

The purpose of this analysis is the application of multi-body mission design tools to the problem of designing a mission in the Saturnian system that includes flybys of several Saturnian moons and that concludes with an Enceladus orbital phase. The fundamental question concerns the potential to gain additional insight or solutions to the Enceladus arrival trajectory problem by using dynamical models of the Saturnian system that incorporate more gravity fields than in a patched conic analysis. Of course, a patched conic approach to mission design is very successful in modeling the Saturnian system. Indeed, at least one point solution to this very mission design problem was accomplished using traditional mission design tools [4]. However, the transfer to Enceladus poses a unique challenge due to the small mass of most of the moons available for gravity-assist flybys. It remains possible that solutions to the Enceladus mission design problem exist in a region of the solution space that is inaccessible under patched conic assumptions. This investigation offers some of the very first steps into the ultimately open-ended problem of multi-body mission design in the Saturnian system, with emphasis on Enceladus accessibility.

1.2 Multi-Body Mission Design in the Saturnian System

Any mission design strategy in the Saturnian system, or any other planetary system for that matter, always originates with the selection of the dynamical model. Dynamical analysis from the multi-body perspective is frequently dependent on the formulation of the model; the model impacts the fundamental characteristics of both individual solutions and the entire solution space. As previously demonstrated by other researchers, it is possible to successfully design a mission to Enceladus using only patched conic assumptions and techniques [4]. However, it is also possible that there are solutions that can only be exposed within the contexts of a multi-body model.

Many problems in astrodynamics will inevitably possess an infinite number of solutions of varying feasibility and optimality. In this investigation the multi-body solution space is probed for additional insight concerning the delivery of a spacecraft to Enceladus; such insight may only be gained from a model that incorporates multiple gravity fields simultaneously. Of course, there is no guarantee that a multi-body analysis will reveal any previously unknown results or that assumptions in formulating a multi-body model will not exclude possible solutions. Nevertheless, a multi-body analysis is explored to identify new options to this challenging problem.

To select a dynamical model that succeeds in approaching the Enceladus mission design problem from a multi-body perspective, it is necessary to carefully consider the balance between the computational speed offered by a simplified model and the accuracy provided by a model of higher fidelity. To determine a spacecraft trajectory to Enceladus, two dynamical regimes are of primary importance; both environments merit specific consideration and separate dynamic models. First, consider the environment where the spacecraft spends substantial time in the vicinity of a single Saturnian moon, while never closely approaching any additional moon; this scenario reflects the portion of an Enceladus mission where the spacecraft is in orbit around Enceladus, or even in a resonant orbit with a single Saturnian moon. Note that, even while in close proximity to Enceladus, the gravitational perturbation due to nearby Saturn should never be neglected. Such an environment is modeled by use of the circular restricted three-body problem.

This formulation of the three-body problem allows Saturn's perturbing influence to be continuously modeled for all spacecraft motion in the vicinity of Enceladus.

The second dynamical regime to be encountered in this analysis occurs during any Saturnian tour that incorporates flybys of several moons to alter the spacecraft's trajectory. The gravity of all such moons involved in the encounters must be included in the dynamical model. The traditional patched conic approach approximates the impact of the gravity from these moons by switching between conic models such that only one gravity field is included during any time interval. The model used to simulate this environment continually incorporates the influence of Saturn and five of its larger inner moons: Enceladus, Tethys, Dione, Rhea, and Titan. Though there are several ways to model the motion of the Saturnian moons, as well as Saturn, this investigation assumes that the orbits of the Saturnian moons are coplanar. This assumption is remarkably accurate for the moons used in this investigation, since all of the orbital inclinations associated with these moons are less than 1.1 degrees [6].

1.3 Historical Contributions

A spacecraft in close proximity to a single Saturnian moon is modeled in this analysis within the context of the Circular Restricted Three-Body Problem (CR3BP). The CR3BP is actually a dynamical model with a surprisingly long and storied past, having been examined by some of the greatest minds in the history of dynamics. Newton published his famous *Philosophiæ Naturalis Principia Mathematica* in 1687; it includes a treatment of the general *n*-body problem, describing the motion through time of an arbitrary number of self-gravitating particles [7, 8]. In particular, Newton examined the three-body problem in an attempt to explain the observed motion of the Moon around the Earth, a problem of such purported difficulty that historical records claim the studies drove Newton's head to "ache" [8].

Euler first examined the three-body problem in 1760. Euler proposed a highly simplified model of the problem that describes the motion of a small particle under the influence of two fixed-position gravitational sources [7]. An assumption of stationary

positions for the massive particles is common in many formulation of the three-body problem, however, Euler's early work neglected the centripetal and Coriolis accelerations. Euler later amended his model to include these latent acceleration terms and this modification led to the formulation of the circular restricted three-body problem that is familiar today, though the name would not be coined by Poincaré for almost 100 years [8]. One of Euler's most significant contributions to the study of the three-body problem was the introduction of a synodic (or rotating) reference frame, one in which the massive particles in the system remain motionless and equilibrium point solutions do exist. Euler's published theory on the motion of the Moon (1772), the manuscript for which Euler is credited with the discovery of the three collinear equilibrium points, shared the *Prix de l'Académie de Paris* with Lagrange [8]. Lagrange's own award-winning manuscript (1772) contained a separate treatment of the restricted three-body problem, one in which Lagrange successfully reduced the system from order 18 to order seven and further identified all five of the Lagrange (or libration) equilibrium point solutions to the CR3BP.

The next major contribution to the CR3BP was supplied by Jacobi (1843). Jacobi not only reduced the order of the system in the restricted three-body problem to 6, but also identified a single integral of motion, later labeled the Jacobian Integral [8, 9]. The full importance of the Jacobian Integral (or Jacobi Constant) was first demonstrated by an astronomer, Hill (1878), who defined physical regions of exclusion where the massless third body in the CR3BP could not exist for some fixed value of Jacobi Constant. Applying his observations of these forbidden regions to the Sun-Earth-Moon system, Hill argued that the Moon was bounded to remain within some fixed distance of the Earth and could not depart this region so long as the Jacobi Constant remained, as the name suggests, constant [9].

One of the greatest contributors to the understanding of the CR3BP was Poincaré, whose 1899 work *Méthodes Nouvelles* [10] was the most important qualitative treatise of the CR3BP to be undertaken up to that time [9]. Poincaré used a qualitative analysis of the CR3BP to successfully prove that the problem is non-integrable by techniques that use traditional integrals of motion [7]. However, Poincaré argued that, despite the lack of

a closed-form solution, there remains an infinite number of periodic solutions in the CR3BP, including those he labeled "doubly asymptotic" and which, today, would be commonly described as chaotic [8].

The CR3BP received its first major contribution of the 20th century from Moulton (1920) who used linearized approximations of the motion of a particle relative to the Lagrange points to prove the existence of three types of three-dimensional periodic orbits in the vicinity of the collinear Lagrange points [11]. Between 1897 and 1911, Darwin studied the "evolution" of periodic solutions to the CR3BP [7], and by 1922 Strömgren and his colleagues in Denmark had undertaken the numerically laborious task of identifying over a dozen categories of orbits in the restricted three-body problem, though a more thorough numerical investigation would wait for the advent of the digital computer [11].

It should be noted that, in 1912, Sundman succeeded in deriving a convergent power series solution to the restricted three-body problem [7, 8]. However, the series solution from Sundman suffers from very slow convergence. As a result, while Sundman effectively "solved" the non-integrable three-body problem, his solution offered virtually no additional insight into the dynamical nature of the CR3BP. The use of Sundman's solution in modern dynamical studies of the CR3BP is particularly rare.

In 1967, Szebehely published his *Theory of Orbits*, which would come to be regarded as the definitive text on the circular restricted three-body problem. Although Szebehely's text is now out-of-print, it remains a common reference on the three-body problem. The application of the restricted three-body problem moved into the space-age in the 1960's when, considering the possible use of a Lagrange point orbiting relay spacecraft for use by NASA's Apollo program, Breakwell was joined at Stanford University by Farquhar. They suggested the use of the out-of-plane "halo" orbits that exist in the CR3BP as a solution to the lunar communications problem [11]. While the analytic approximations later used by Farquhar and Kamel (1973) [12] tend to break down as the size of the halo orbits increases, Howell (1984) undertook a largely numerical study to extend the families of halo orbits beyond the ranges of those previously computed [13]. While never employed for the Apollo program, the halo orbits originally identified by Farquhar

and Breakwell (1970) [14, 15] and the halo families later expanded by Farquhar and Kamel [12], as well as Howell [13], would ultimately see flight by a number of robotic spacecraft including ISEE-3 [16], WIND [17], SOHO [18], ACE [19], MAP [20], and Genesis [21]. As many as four additional Lagrange point missions are at various phases of design or fabrication and all are scheduled to launch by 2013 [22].

1.4 Focus of this Work

Building on the solid historical basis of the circular restricted three-body problem, the current investigation endeavors to apply established mission design techniques from the restricted three-body problem to the problem of mission design in the Saturnian system, with Enceladus as a specific target of interest. In addition to a reliance on a rich background relating to the dynamical systems used throughout this investigation, an alternative method of mission design is also explored. However, the core of this analysis is the application of multi-body dynamics to a very real physical problem in this solar system, and dynamical tools, therefore, are developed for the express purpose of probing the Saturnian system.

This investigation is organized as follows:

- Chapter 2: The necessary background regarding the formulation of the circular restricted three-body problem is developed. A derivation of the State Transition Matrix (STM) associated with various periodic orbits in the three-body problem is included as well as a discussion of the application of the STM in targeting closed periodic orbits in the restricted three-body problem. Two-body mean motion orbital resonance is introduced and compared to orbital resonance in the restricted three-body problem. A method to identify and correct resonant orbits in the circular restricted three-body problem is detailed. A discussion relating to the mechanics of gravity-assist flyby trajectories is provided both for the patched conic model as well

as multi-body models. A means of quantifying the effect of a gravity-assist flyby in a multi-body dynamical model is introduced.

- Chapter 3: A preliminary examination of orbits in the vicinity of Saturn's moon, Enceladus, is described. The orbits of interest include families of periodic Lagrange point trajectories, both planar and three-dimensional, as well as nearly "conic" circular orbits. The sensitivity of low Enceladus orbits is demonstrated through sample numerical integration.

- Chapter 4: Resonant orbits, and a means to calculate such orbits, are introduced both for the two-body as well as the three-body model. Families of resonant orbits are constructed as a demonstration of their utility to the problem of identifying a spacecraft trajectory that will frequently fly by Enceladus. An additional model of the Saturnian system, one that includes the gravitational influence of Saturn and five of its larger inner moons, is introduced; trajectories computed in the restricted three-body problem are integrated into this six-body model to illustrate differences between the models.

- Chapter 5: An optimization-based algorithm to design a sequence of flybys of the Saturnian moons is developed and implemented to design trajectories in the multi-body Saturnian model. The formulation of the trajectory design algorithm is detailed and flyby sequences that result from this algorithm are demonstrated. The advantages and disadvantages of this multi-body trajectory design algorithm are discussed in comparison to patched conic mission analysis

- Chapter 6: The final chapter includes a summary of the major results of the investigation. Also included is a discussion of possible future work to extend the results.

2. BACKGROUND

2.1 The Circular Restricted Three-Body Problem (CR3BP)

This investigation will make frequent use of the restricted three-body problem in modeling a system that includes both Saturn and one of its moons. To facilitate a better understanding of the results drawn from this model when it is applied specifically to the Saturnian system, the full formulation of the circular restricted three-body problem is first introduced.

2.1.1 Assumptions

The general three-body problem offers a framework to determine the motion, as a function of time, of a particle, P_3 of mass m_3, under the gravitational influence of two larger particles, P_1 and P_2, of masses m_1 and m_2, respectively. The general three-body problem is a reduced model in the *n*-body problem of celestial mechanics, where $n = 3$. The positions of each of the particles are measured in a coordinate system with an inertially fixed base point, O, as apparent in Figure 2.1. In celestial mechanics, the problem that represents the motion of n bodies possesses a closed-form analytical solution only for the case of two bodies (i.e., $n = 2$). However, the solution to even the two-body problem requires the introduction of a specific formulation, that is, relative motion as opposed to absolute motion. As such, it is not surprising that the addition of a third gravitational source in the general three-body problem results in a dynamical system of equations that cannot be solved analytically in closed form. In this case, the equations

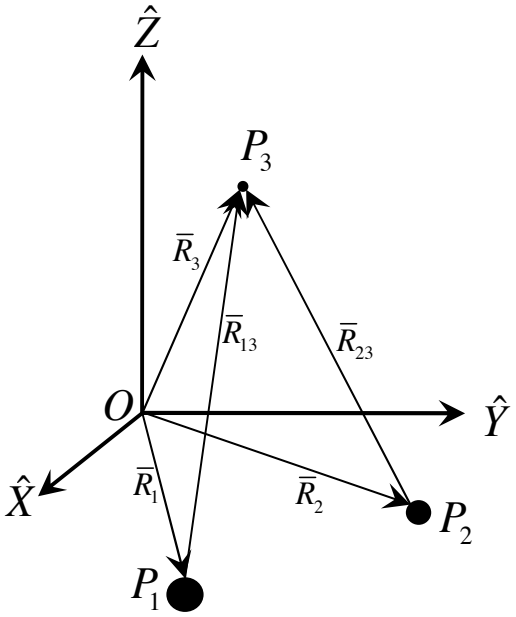

Figure 2.1 Formulation of the general three-body problem.

of motion (EOM) governing the system behavior can be easily derived by combining the vector forms of Newton's second law with Newton's law of universal gravitation to yield the following,

$$m_3\overline{R}_3'' = -\frac{Gm_3m_1}{R_{13}^{\ 3}}\overline{R}_{13} - \frac{Gm_3m_2}{R_{23}^{\ 3}}\overline{R}_{23}, \tag{2.1}$$

where overbars indicate vector quantities. In Equation 2.1, prime denotes a time derivative with respect to an inertially fixed base point and the position vectors are defined in Figure 2.1. Based on the laws of Newtonian mechanics, the linear momentum, angular momentum, and total energy of the system combine to produce a total of 10 scalar integrals of the motion. However, given the dependent variables in Equation 2.1, a complete solution requires 18 integrals of the motion. Since the required number of constants to solve Equation 2.1 is greater than the number of integrals that are available based on mechanics, the general three-body problem is non-integrable.

Despite the fact that the general three-body problem cannot be solved analytically in closed form, it is possible to reduce the problem with the aid of simplifying assumptions. The assumptions consistent with the Circular Restricted Three-Body Problem (CR3BP)

are generally very successful in decreasing the complexity of the problem. The first assumption involves the mass of the particle of interest, P_3. The mass m_3 is assumed to be infinitesimal in relation to the masses of the other two particles: $m_3 << m_1, m_2$. Effectively, this assumption implies that the two remaining particles, P_1 and P_2, exert a gravitational influence on each other as well as on the particle of interest, P_3, but the third particle will not affect the motion of the two larger bodies. Thus, P_1 and P_2 move in two-body conic orbits. The reduced formulation reflected in the CR3BP offers additional dynamical insight, although an analytical solution to the problem is still not available.

An additional assumption to further reduce the problem, is a restriction on the motion of the two massive particles, P_1 and P_2. The two primary bodies are assumed to move on perfectly circular paths relative to the barycenter of the system and to each other. Another common formulation of the three-body problem, one not considered here, allows

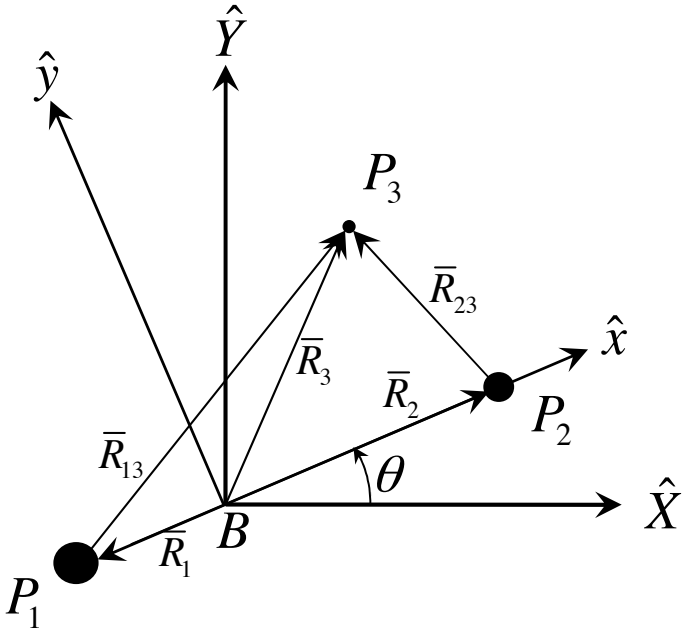

Figure 2.2 Formulation of the Circular Restricted Three-Body Problem (CR3BP) relative to a rotating coordinate system.

for elliptical motion of the primaries relative to their common barycenter. However, this elliptic formulation is more complex and unnecessary when applied to the Saturnian system, where many of the moons lie on nearly circular orbits around Saturn, with typical eccentricities on the order of $e = 0.001$ [6]. The formulation of the CR3BP appears graphically in Figure 2.2. In Figure 2.2, a standard cartesian inertial vector basis, I, centered at the system barycenter, B, is defined, denoted with directions along $\hat{X}$ and $\hat{Y}$ (where $\hat{Z}$ is normal to the page). Note that a carat indicates a unit vector. Introduce an additional rotating reference frame, R, centered at the system barycenter, B, such that the x-axis of the rotating frame, $\hat{x}$, is always parallel to the line connecting the larger primary, P_1, to the smaller primary, P_2. The z-axis of the rotating reference frame, $\hat{z}$, is directed parallel to the orbital angular momentum vector associated with the motion of the system primaries, and $\hat{y}$ completes the right-hand vector basis. The rotating reference frame is related to the inertial reference frame through the angle, θ. The rotation rate of this reference frame, is equal to the mean motion of the system primaries, N. The introduction of this rotating reference frame is key to the formulation of the CR3BP because it facilitates the identification of fixed equilibrium points that correspond to solutions to the nonlinear system of equations. The equilibrium points serve as a starting point for the determination of periodic orbits in the CR3BP.

2.1.2 Derivation of the Non-Dimensional Equations of Motion

In addition to the simplifying assumptions, the equations of motion (EOM) in the restricted three-body problem are typically manipulated to further simplify their form and appearance. First, the EOM in the three-body problem (i.e., Equation 2.1) are non-dimensionalized by multiplication and division with appropriate characteristic quantities. The characteristic quantities are defined to reduce the parametric quantities in the EOM to unity. The characterisitic length, l^*, is equal to the distance between the primaries,

$$l^* = \left\|\overline{R}_1\right\| + \left\|\overline{R}_2\right\|, \tag{2.2}$$

and the characteristic mass, m^*, is equal to the sum of the masses of the two primaries,

$$m^* = m_1 + m_2. \tag{2.3}$$

The characteristic time, t^*, is defined as the rotation period of the system primaries,

$$t^* = \left[\frac{l^*}{\widetilde{G}m^*}\right]^{\frac{1}{2}}, \tag{2.4}$$

where the definition of t^* depends also on the non-dimensional gravitational constant,

$$\widetilde{G} = \frac{G(l^*)^3}{m^*(t^*)^2} = 1. \tag{2.5}$$

The independent variable in the CR3BP is time, specifically τ, the non-dimensional time,

$$\tau = \frac{t}{t^*}. \tag{2.6}$$

Finally, the mean motion of the primary bodies is also non-dimensionalized to the value n, such that,

$$n = N \cdot t^* = \frac{d\theta}{d\tau} = 1. \tag{2.7}$$

In addition to the definition of the characteristic quantities, the EOM in the CR3BP are typically expressed in terms of the mass fraction associated with the two system primaries, P_1 and P_2. This mass fraction, μ, is defined as follows,

$$\mu = \frac{m_2}{m_1 + m_2} = \frac{m_2}{m^*}. \tag{2.8}$$

With the characteristic quantities as defined in Equations 2.2-2.8, it is possible to simplify the original EOM, Equation 2.1, to the following vector form,

$$\bar{r}_3'' = \frac{-(1-\mu)\bar{r}_{13}}{r_{13}^{\ 3}} - \frac{-\mu\ \bar{r}_{23}}{r_{23}^{\ 3}}, \tag{2.9}$$

where the superscript primes denote derivatives with respect to non-dimensional time, τ, as measured in terms of the inertial reference frame centered on the CR3BP system barycenter. The relative position vectors that appear in Equation 2.9 result from the non-dimensionalization of the corresponding position vectors in the general three-body problem, that is,

$$\bar{r}_3 = \frac{\bar{R}_3}{l^*} = x\hat{x} + y\hat{y} + z\hat{z}, \tag{2.10}$$

$$\bar{r}_{13} = \frac{\bar{R}_{13}}{l^*} = (x+\mu)\hat{x} + y\hat{y} + z\hat{z}, \tag{2.11}$$

$$r_{13} = \frac{\left\|\bar{R}_{13}\right\|}{l^*} = \sqrt{(x+\mu)^2 + y^2 + z^2}, \tag{2.12}$$

$$\bar{r}_{23} = \frac{\bar{R}_{23}}{l^*} = \left[x-(1-\mu)\right]\hat{x} + y\hat{y} + z\hat{z}, \tag{2.13}$$

$$r_{23} = \frac{\left\|\bar{R}_{23}\right\|}{l^*} = \sqrt{\left[x-(1-\mu)\right]^2 + y^2 + z^2}. \tag{2.14}$$

Note that these vectors are written in terms of components in the rotating frame.

The vector EOM in Equation 2.9, while complete, is far more useful when written in terms of the cartesian coordinates of the rotating reference frame. To this end, kinematic expressions for $\bar{r}_3'$ and $\bar{r}_3''$ can be derived by application of the well-known kinematic expansion, that is,

$$\bar{r}_3' = \frac{{}^I d\bar{r}_3}{d\tau} = \frac{{}^R d\bar{r}_3}{d\tau} + {}^I\bar{\omega}^R \times \bar{r}_3 , \tag{2.15}$$

$$\bar{r}_3'' = \frac{{}^I d^2\bar{r}_3}{d\tau^2} = \frac{{}^R d^2\bar{r}_3}{d\tau^2} + 2{}^I\bar{\omega}^R \times \bar{r}_3 + {}^I\bar{\omega}^R \times \left({}^I\bar{\omega}^R \times \bar{r}_3 \right). \tag{2.16}$$

In Equation 2.16, $\bar{r}_3''$ is the inertial second derivative with respect to non-dimensional time, in terms of derivatives as observed in the rotating reference frame and the angular rotation rate of the rotating reference frame, that is, ${}^I\bar{\omega}^R = \frac{d\theta}{d\tau}\hat{z} = n\hat{z} = \hat{z}$. The kinematic expressions for the velocity and acceleration with respect to non-dimensional time, $\frac{{}^R d^2\bar{r}_3}{d\tau^2}$, are written as follows,

$$\dot{\bar{r}}_3 = \frac{{}^R d\bar{r}_3}{d\tau} = \dot{x}\hat{x} + \dot{y}\hat{y} + \dot{z}\hat{z} , \tag{2.17}$$

$$\ddot{\bar{r}}_3 = \frac{{}^R d^2\bar{r}_3}{d\tau^2} = \ddot{x}\hat{x} + \ddot{y}\hat{y} + \ddot{z}\hat{z} , \tag{2.18}$$

where the dots denote derivatives relative to an observer in the rotating reference frame, *R*, and with respect to non-dimensional time. After substituting the result of Equation 2.18 into Equation 2.16, it is apparent that the kinematic expansion for the inertial velocity and acceleration are expressed as,

$$\bar{r}_3' = (\dot{x} - ny)\hat{x} + (\dot{y} + nx)\hat{y} + \dot{z}\hat{z} , \tag{2.19}$$

$$\bar{r}_3'' = \frac{{}^I d^2\bar{r}_3}{d\tau^2} = (\ddot{x} - 2n\dot{y} - n^2 x)\hat{x} + (\ddot{y} + 2n\dot{x} - n^2 y)\hat{y} + \ddot{z}\hat{z} . \tag{2.20}$$

The result of Equation 2.20 can finally be substituted on the left side in Equation 2.9 and further decomposed into scalar form to deliver the final CR3BP equations of motion:

$$\ddot{x} - 2n\dot{y} - n^2 x = \frac{-(1-\mu)(x+\mu)}{r_{13}^{\ 3}} - \frac{\mu \cdot [x-(1-\mu)]}{r_{23}^{\ 3}}, \tag{2.21}$$

$$\ddot{y} + 2n\dot{x} - n^2 y = \frac{-(1-\mu)y}{r_{13}^{\ 3}} - \frac{\mu \cdot y}{r_{23}^{\ 3}}, \tag{2.22}$$

$$\ddot{z} = \frac{-(1-\mu)z}{r_{13}^{\ 3}} - \frac{\mu \cdot z}{r_{23}^{\ 3}}. \tag{2.23}$$

These differential equations govern the motion of P_3 under the gravitational influence of the two primaries, and all simulations in the CR3BP will result from the numerical integration of Equations 2.21-2.23.

2.1.3 The Jacobian Integral

As a means of simplifying the expression of the EOM in the CR3BP, define a pseudo-potential function,

$$U^* = \frac{(1-\mu)}{r_{13}} + \frac{\mu}{r_{23}} + \frac{(x^2+y^2)}{2}. \tag{2.24}$$

The pseudo-potential function is similar to the gravitational potential function in that it depends only on position within the three-body system, but U^* also includes the centrifugal acceleration of the CR3BP. Note that the equations of motion of the CR3BP can be rewritten in terms of the pseudo-potential function as:

$$\ddot{x} - 2\dot{y} = \frac{\partial U^*}{\partial x}, \tag{2.25}$$

$$\ddot{y} + 2\dot{x} = \frac{\partial U^*}{\partial y}, \tag{2.26}$$

$$\ddot{z} = \frac{\partial U^*}{\partial z}. \tag{2.27}$$

It is possible to operate on Equations 2.25-2.27 and produce a single integral of the motion in the CR3BP. One method to determine this integral involves the dot product of the rotating velocity vector, $\dot{\bar{r}} = \dot{x}\hat{x} + \dot{y}\hat{y} + \dot{z}\hat{z}$, and the vector expression of the EOM in Equations 2.25-2.27. The expression that results is,

$$\dot{x}\ddot{x} + \dot{y}\ddot{y} + \dot{z}\ddot{z} = \frac{dU^*}{d\tau}, \tag{2.28}$$

and this expression can be directly integrated over non-dimensional time, τ, and further reduced to the form,

$$\frac{1}{2}\left(\dot{x}^2 + \dot{y}^2 + \dot{z}^2\right) = 2U^* - \frac{c}{2}. \tag{2.29}$$

The constant of integration in Equation 2.29 is arbitrarily defined as $\frac{c}{2}$ so that the constant can be more easily expressed as,

$$c = 2U^* - v^2. \tag{2.30}$$

The constant of integration, c, is an integral of the motion and is referred to variously as the Jacobian Integral and Jacobi Constant. The Jacobi Constant possesses particular value for astrodynamics problems since it is an energy-like quantity that remains constant regardless of the motion of a particle in the CR3BP. Knowledge of the Jacobi Constant associated with a path in the CR3BP is used to determine forbidden regions that are inaccessible to the particle throughout the evolution of its path.

2.1.4 Transformations between the Inertial and Rotating Reference Frames

As is frequently true for many astrodynamics problems, data may be best visualized in the rotating reference frame, the inertial reference frame, or both. As such, a transformation between these two frames is desirable. In general, the transformation of a vector from rotating coordinates to inertial coordinates is accomplished via a direction cosine matrix, ${}^{I}C^{R}(\tau)$, that is,

$$\begin{bmatrix} \hat{X} \\ \hat{Y} \\ \hat{Z} \end{bmatrix} = {}^{I}C^{R}(\tau) \begin{bmatrix} \hat{x} \\ \hat{y} \\ \hat{z} \end{bmatrix}. \tag{2.31}$$

In the CR3BP, the angle between the rotating reference frame and the inertial reference frame increases at a constant rate (Equation 2.7). Therefore, the transformation matrix depends only on the non-dimensional time, τ. The transformation matrix in the CR3BP describes a simple rotation about the common z-axis of the rotating and inertial reference frames,

$${}^{I}C^{R}(\tau) = \begin{bmatrix} \cos(\tau - \tau_0) & -\sin(\tau - \tau_0) & 0 \\ \sin(\tau - \tau_0) & \cos(\tau - \tau_0) & 0 \\ 0 & 0 & 1 \end{bmatrix}, \tag{2.32}$$

where τ_0 is the initial integration time, and is generally assumed to be zero.

Of additional utility is a matrix transformation that simultaneously transforms both position and velocity states between the rotating and inertial reference frames. However, transformation of the velocity state involves the use of the basic kinematic equation from Equation 2.15. To derive the transformation matrix, first define the position and velocity vectors in terms of inertial coordinates,

$$\bar{r}_3 = X\hat{X} + Y\hat{Y} + Z\hat{Z}, \tag{2.33}$$

$$\bar{r}_3' = X'\hat{X} + Y'\hat{Y} + Z'\hat{Z}\,. \tag{2.34}$$

The kinematic description of an inertial position and velocity state in terms of rotating coordinates appears in Equations 2.10 and 2.20. The complete transformation from rotating to inertial coordinates results in the following block matrix for the position and velocity transformation:

$$\begin{bmatrix} X \\ Y \\ Z \\ X' \\ Y' \\ Z' \end{bmatrix} = \begin{bmatrix} {}^{I}C^{R}(\tau) & 0_{3\times3} \\ \dot{C}(\tau) & {}^{I}C^{R}(\tau) \end{bmatrix} \begin{bmatrix} x \\ y \\ z \\ \dot{x} \\ \dot{y} \\ \dot{z} \end{bmatrix}. \tag{2.35}$$

Of course, the inverse transformation between position and velocity components is then,

$$\begin{bmatrix} x \\ y \\ z \\ \dot{x} \\ \dot{y} \\ \dot{z} \end{bmatrix} = \begin{bmatrix} {}^{I}C^{R}(\tau) & 0_{3\times3} \\ \dot{C}(\tau) & {}^{I}C^{R}(\tau) \end{bmatrix}^{-1} \begin{bmatrix} X \\ Y \\ Z \\ X' \\ Y' \\ Z' \end{bmatrix}. \tag{2.36}$$

The lower-left sub-matrix in Equation 2.35 and 2.36, $\dot{C}(\tau)$, is defined,

$$\dot{C}(\tau) = \begin{bmatrix} -\sin(\tau-\tau_0) & -\cos(\tau-\tau_0) & 0 \\ \cos(\tau-\tau_0) & -\sin(\tau-\tau_0) & 0 \\ 0 & 0 & 0 \end{bmatrix}. \tag{2.37}$$

Note the close relationship between the matrix in Equation 2.37 and the transformation matrix in Equation 2.32.

2.1.5 The Lagrange Points

It is noteworthy that the equations of motion for the CR3BP, Equations 2.21-2.23, are autonomous. As a result, time-independent stationary solutions and/or periodic orbits may exist. In fact, five equilibrium point solutions to Equations 2.21-2.23 are known. Stationary solutions are determined by solving for the x, y, and z position coordinates that result in the rotating velocity and acceleration components equaling zero,

$$x_L = \frac{-(1-\mu)(x_L+\mu)}{r_{13_L}^{\ 3}} - \frac{\mu\cdot\left[x_L-(1-\mu)\right]}{r_{23_L}^{\ 3}}, \tag{2.38}$$

$$y_L = \frac{-(1-\mu)y_L}{r_{13_L}^{\ 3}} - \frac{\mu\cdot y}{r_{23_L}^{\ 3}}, \tag{2.39}$$

$$0 = \frac{-(1-\mu)z_L}{r_{13_L}^{\ 3}} - \frac{\mu\cdot z_L}{r_{23_L}^{\ 3}}. \tag{2.40}$$

The position coordinates of the stationary solutions to these CR3BP equations of motion are denoted with a subscript "L" in acknowledgment of Joseph-Louis Lagrange, in whose honor the equilibrium points are named.

While all three of Equations 2.38-2.40 are coupled non-linear differential equations, Equation 2.40, can be examined independently. Note that by reducing the z acceleration to zero in Equation 2.40, the value of z_L can be solved trivially to determine, $z_L = 0$. This result immediately indicates that all equilibrium solutions to Equations 2.21-2.23 lie in the plane of motion of the two primary bodies, P_1 and P_2. The location of two of the equilibrium point solutions, those known as the equilateral points, were first identified by Lagrange [8]. Lagrange observed that by assuming $r_{13_L} = r_{23_L} = 1$, Equations 2.38 and 2.39 reduce to an identity. Given that $r_{13_L} = r_{23_L} = 1$, the equilibrium point is exactly the same distance from both the first and second primaries; this distance is also equal to the separation distance between the two primaries. There are two points in the xy-plane that

satisfy these conditions. These two equilibrium points, commonly labeled L_4 and L_5, are located at the third vertices of two equilateral triangles, symmetric across the *x*-axis, that include the two system primaries, P_1 and P_2, at the remaining triangle vertices, as seen in Figure 2.3. The location of L_4 and L_5, at the vertices of these equilateral triangles leads to a common name for these points, "the equilateral points."

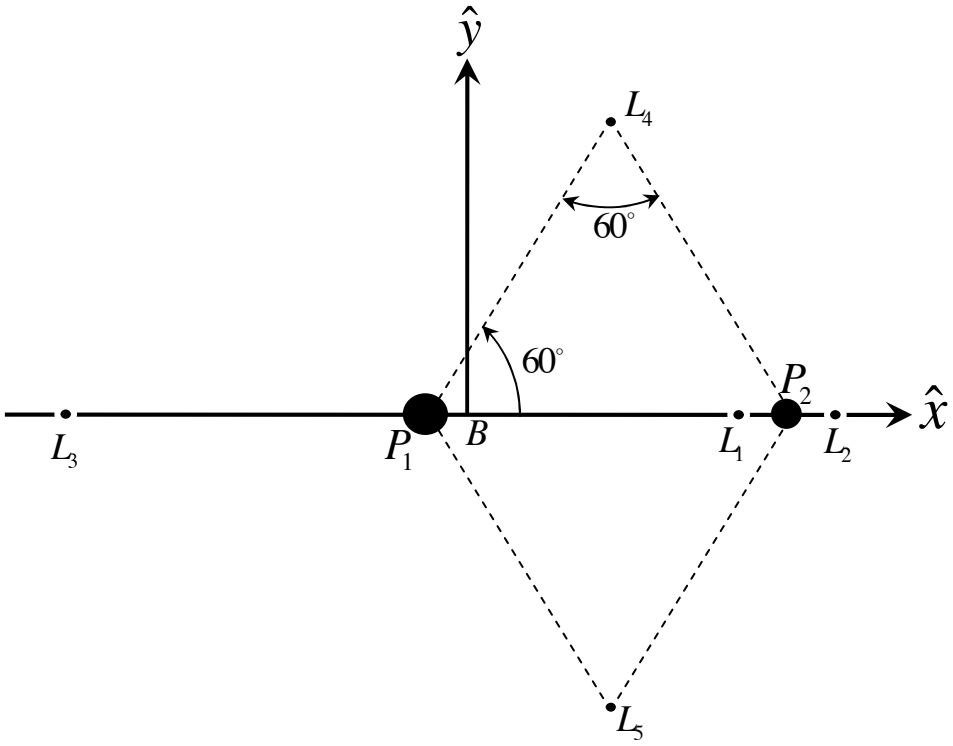

Figure 2.3 Relative locations of the five Lagrange points in the CR3BP.

Knowledge of the locations of L_4 and L_5, at the vertices of equilateral triangles, immediately yields the coordinates of these equilibrium Lagrange points, that is, $x_L = \left(\frac{1}{2} - \mu\right)$ and $y_L = \pm\frac{\sqrt{3}}{2}$. By convention L_4 corresponds to the positive y_L value and leads the second primary, P_2, in its orbit around the barycenter; L_5 is located at $y_L = -\frac{\sqrt{3}}{2}$ and trails the motion of the second primary.

Although not as geometrically intuitive, three additional equilibrium points exist in the CR3BP. These remaining Lagrange points, L_1, L_2, and L_3, are isolated by assuming $y_L = z_L = 0$ in Equations 2.38-2.40. Equations 2.38 then reduces to a fifth-order polynomial equation in x_L. By nulling the *y* and *z* coordinates of the remaining Lagrange points, the physical location of the final equilibrium points is constrained to lie along the line connecting the two system primaries, P_1 and P_2; thus, these points along the *x*-axis are labeled the "collinear points". The solution for x_L using a numerical root solving technique returns five roots, although two include imaginary components that lack physical significance. The three remaining real-valued roots for x_L supply the *x*-coordinates for the remaining Lagrange points. The values of x_L corresponding to the collinear points vary depending on the system mass ratio, μ. As in Figure 2.3, regardless of the μ value of the system, the Lagrange points are labeled according to a common convention, where L_1 is the collinear equilibrium point that lies between P_1 and P_2, L_2 lies along the *x*-axis beyond the P_2 mass in the $+\hat{x}$ direction, and L_3 is also on the *x*-axis, but beyond the P_1 mass in the $-\hat{x}$ direction.

2.1.6 The State Transition Matrix

In addition to the Lagrange equilibrium point solutions, it is also often desirable to search for periodic orbits near the Lagrange points that are solutions to the non-linear differential equations of the CR3BP. The CR3BP is non-integrable, so computing periodic solutions requires a numerical differential corrections process. At the heart of the numerical corrections scheme used in this analysis is a State Transition Matrix (STM) associated with the variational equations relative to a reference solution to the non-linear differential equations in the CR3BP.

Many of the elements of the STM depend on derivatives of the energy-like scalar pseudo-potential function from Equation 2.24. Given a reference solution, variations

with respect to the reference are predicted using the STM. The development of the variational equations begins with the state space representation of the non-linear CR3BP in terms of the state, $\bar{X}(\tau) = \begin{bmatrix} x & y & z & \dot{x} & \dot{y} & \dot{z} \end{bmatrix}^T$,

$$\dot{\bar{X}} = \bar{f}(\bar{X}). \tag{2.41}$$

However, the three-body problem is non-integrable, so a closed form solution for $\bar{X}(\tau)$ is unattainable. Instead, define a reference path in the CR3BP, $\bar{X}_n(\tau)$, that is both time-varying and satisfies the differential equations of motion. In this case, a desired solution nearby the reference, $\bar{X}(\tau) = \bar{X}_n(\tau) + \delta\bar{X}_n(\tau)$, can be represented by a Taylor's series expansion about $\bar{X}_n(\tau)$ neglecting all terms of order higher than the first-order linear approximation. The Taylor series expansion results in the linear system equation expressed in terms of the variations in the state $\delta\bar{X}(\tau) = \begin{bmatrix} \delta x & \delta y & \delta z & \delta\dot{x} & \delta\dot{y} & \delta\dot{z} \end{bmatrix}^T$,

$$\delta\dot{\bar{X}}(\tau) = A(\tau)\delta\bar{X}(\tau) \longrightarrow \begin{bmatrix} \delta\dot{x} \\ \delta\dot{y} \\ \delta\dot{z} \\ \delta\ddot{x} \\ \delta\ddot{y} \\ \delta\ddot{z} \end{bmatrix} = \begin{bmatrix} 0 & 0 & 0 & 1 & 0 & 0 \\ 0 & 0 & 0 & 0 & 1 & 0 \\ 0 & 0 & 0 & 0 & 0 & 1 \\ U^*_{xx} & U^*_{xy} & U^*_{xz} & 0 & 2 & 0 \\ U^*_{yx} & U^*_{yy} & U^*_{yz} & -2 & 0 & 0 \\ U^*_{zx} & U^*_{zy} & U^*_{zz} & 0 & 0 & 0 \end{bmatrix} \begin{bmatrix} \delta x \\ \delta y \\ \delta z \\ \delta\dot{x} \\ \delta\dot{y} \\ \delta\dot{z} \end{bmatrix}. \tag{2.42}$$

In Equation 2.42, $A(\tau)$ is the Jacobian matrix defined as $A(\tau) = \left.\dfrac{\partial\bar{f}}{\partial\bar{X}}\right|_{\bar{X}_n}$, and is evaluated along the reference solution, $\bar{X}_n(\tau)$. The lower-right 3×3 sub-matrix of $A(\tau)$ in Equation 2.42 involves the second partial derivatives of the pseudo-potential function from Equation 2.24,

$$U^*_{xx} = \frac{\partial^2 U^*}{\partial x^2} = 1 - \frac{(1-\mu)}{r_{13}^{\ 3}} - \frac{\mu}{r_{23}^{\ 3}} + \frac{3(1-\mu)(x+\mu)^2}{r_{13}^{\ 5}} + \frac{3\mu(x-1+\mu)^2}{r_{23}^{\ 5}}, \tag{2.43}$$

$$U_{yy}^{*} = \frac{\partial^2 U^{*}}{\partial y^2} = 1 - \frac{(1-\mu)}{r_{13}^{\ 3}} - \frac{\mu}{r_{23}^{\ 3}} + \frac{3(1-\mu)y^2}{r_{13}^{\ 5}} + \frac{3\mu \cdot y^2}{r_{23}^{\ 5}}, \tag{2.44}$$

$$U_{zz}^{*} = \frac{\partial^2 U^{*}}{\partial z^2} = -\frac{(1-\mu)}{r_{13}^{\ 3}} - \frac{\mu}{r_{23}^{\ 3}} + \frac{3(1-\mu)z^2}{r_{13}^{\ 5}} + \frac{3\mu \cdot z^2}{r_{23}^{\ 5}}, \tag{2.45}$$

$$U_{xy}^{*} = \frac{\partial^2 U^{*}}{\partial x \partial y} = U_{yx}^{*} = \frac{3(1-\mu)(x+\mu)y}{r_{13}^{\ 5}} + \frac{3\mu(x-1+\mu)y}{r_{23}^{\ 5}}, \tag{2.46}$$

$$U_{xz}^{*} = \frac{\partial^2 U^{*}}{\partial x \partial z} = U_{zx}^{*} = \frac{3(1-\mu)(x+\mu)z}{r_{13}^{\ 5}} + \frac{3\mu(x-1+\mu)z}{r_{23}^{\ 5}}, \tag{2.47}$$

$$U_{yz}^{*} = \frac{\partial^2 U^{*}}{\partial y \partial z} = U_{zy}^{*} = \frac{3(1-\mu)y \cdot z}{r_{13}^{\ 5}} + \frac{3\mu \cdot y \cdot z}{r_{23}^{\ 5}}. \tag{2.48}$$

The general solution [23] to the differential equations in Equation 2.42 will be of the following form,

$$\delta\overline{X}(\tau) = \Phi(\tau, \tau_0)\delta\overline{X}(\tau_0). \tag{2.49}$$

In general, the matrix, $\Phi(\tau, \tau_0)$, as in Equation 2.49, is the State Transition Matrix (STM) that relates the variation in the system state at integration time, τ_0, to the variation at time τ. The STM reflects the sensitivities via the following partial derivatives,

$$\Phi(\tau_2,\tau_1)=\begin{bmatrix} \frac{\partial x}{\partial x_0} & \frac{\partial x}{\partial y_0} & \frac{\partial x}{\partial z_0} & \frac{\partial x}{\partial \dot{x}_0} & \frac{\partial x}{\partial \dot{y}_0} & \frac{\partial x}{\partial \dot{z}_0} \\ \frac{\partial y}{\partial x_0} & \frac{\partial y}{\partial y_0} & \frac{\partial y}{\partial z_0} & \frac{\partial y}{\partial \dot{x}_0} & \frac{\partial y}{\partial \dot{y}_0} & \frac{\partial y}{\partial \dot{z}_0} \\ \frac{\partial z}{\partial x_0} & \frac{\partial z}{\partial y_0} & \frac{\partial z}{\partial z_0} & \frac{\partial z}{\partial \dot{x}_0} & \frac{\partial z}{\partial \dot{y}_0} & \frac{\partial z}{\partial \dot{z}_0} \\ \frac{\partial \dot{x}}{\partial x_0} & \frac{\partial \dot{x}}{\partial y_0} & \frac{\partial \dot{x}}{\partial z_0} & \frac{\partial \dot{x}}{\partial \dot{x}_0} & \frac{\partial \dot{x}}{\partial \dot{y}_0} & \frac{\partial \dot{x}}{\partial \dot{z}_0} \\ \frac{\partial \dot{y}}{\partial x_0} & \frac{\partial \dot{y}}{\partial y_0} & \frac{\partial \dot{y}}{\partial z_0} & \frac{\partial \dot{y}}{\partial \dot{x}_0} & \frac{\partial \dot{y}}{\partial \dot{y}_0} & \frac{\partial \dot{y}}{\partial \dot{z}_0} \\ \frac{\partial \dot{z}}{\partial x_0} & \frac{\partial \dot{z}}{\partial y_0} & \frac{\partial \dot{z}}{\partial z_0} & \frac{\partial \dot{z}}{\partial \dot{x}_0} & \frac{\partial \dot{z}}{\partial \dot{y}_0} & \frac{\partial \dot{z}}{\partial \dot{z}_0} \end{bmatrix}. \tag{2.50}$$

Thus, the STM effectively serves as a linear predication of the sensitivity of the final state of a solution to variations in the state at an earlier time.

Differentiating Equation 2.49 and substituting the resulting expression into Equation 2.42 results in the differential equation that governs the evolution of the STM,

$$\dot{\Phi}(\tau,\tau_0)=A(\tau)\Phi(\tau,\tau_0)\,. \tag{2.51}$$

Since $A(\tau)$ is evaluated along a time-varying reference solution, in general, $A(\tau)$ is time-varying (although $A(\tau)$ is constant for variations relative to the Lagrange points, of course). The state transition matrix, $\Phi(\tau,\tau_0)$, is generally determined through numerical integration of Equation 2.51 along with the EOM in Equations 2.21-2.23. At the initial time, $\Phi(\tau_0,\tau_0)$, is equal to the 6×6 identity matrix.

2.1.7 Differential Corrections Scheme to Determine Periodic Orbits in the CR3BP

To determine periodic orbits in the restricted three-body problem, a differential corrections algorithm is employed and various formulations are available. One type of corrections algorithm is a targeter in which small adjustments are made to the initial state, to achieve some desired final state. In an extension of a targeter, a periodic orbit is

determined by solving a two-point boundary value problem such that the initial and final states are identical.

The differential corrector in the current investigation incorporates a gradient-based multi-dimensional Newton process, schematically represented in Figure 2.4. In this approach, a reference trajectory is integrated forward in time from some known six-dimensional initial state, $\overline{X}(\tau_0)$, comprised of the spacecraft cartesian position and velocity components. The resulting final state along the reference path is denoted as $\overline{X}(\tau_f)$. The objective of the differential corrections process is the determination of the initial variation, $\delta\overline{X}(\tau_0)$, relative to the initial state, $\overline{X}(\tau_0)$, that results in the delivery of P_3 to a desired final target state, that is, $\overline{X}^*$. Thus, the target state can be expressed in terms of the variation relative to the reference trajectory, that is, $\overline{X} = \overline{X}(\tau_f) + \delta\overline{X}(\tau_f + \delta\tau)$. Note that the representation of the final variation incorporates $\delta\tau$ since the corrector also allows an adjustment in the time relative to the reference path. The derivation of the differential corrections algorithm is applicable to any reference trajectory. For the determination of a general periodic orbit, the initial and final state

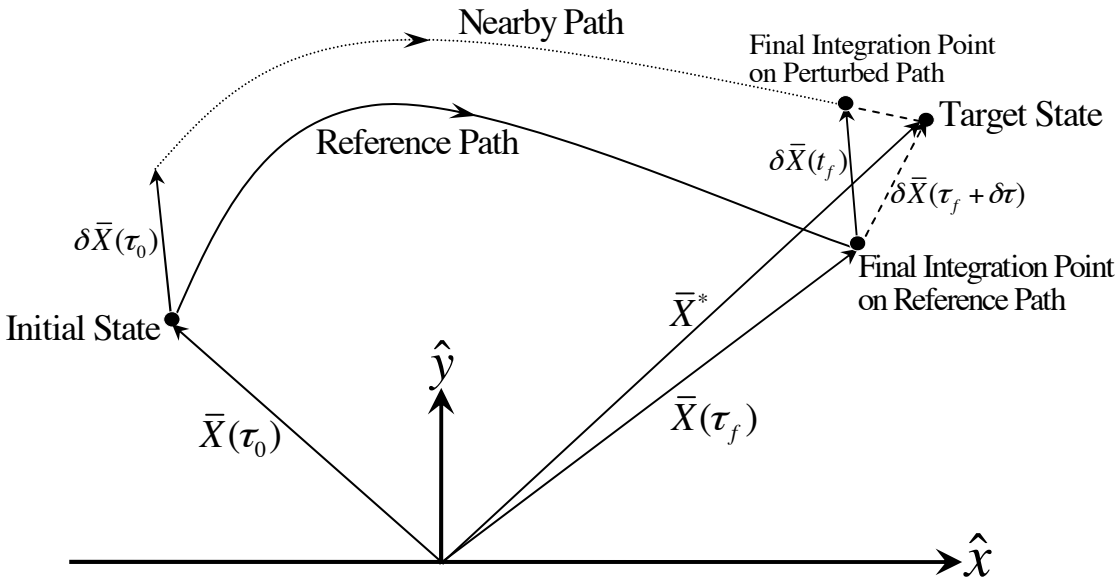

Figure 2.4 Basic schematic of a time-varying targeting method.

along the corrected trajectory arc are identical: $\overline{X}(\tau_0)+\delta\overline{X}(\tau_0)=\overline{X}(\tau_f)+\delta\overline{X}(\tau_f+\delta\tau)$. The CR3BP is a time-invariant system, thus, matching the conditions of the initial state at some later integration time ensures periodic motion. An infinite number of periodic orbits exist in the CR3BP, and many of the orbits lack any intuitive symmetry. However, besides time-invariance, the differential equations possess symmetry across the *xz*-plane. Thus, families of periodic orbits with notable symmetry are also available, including families symmetric across the *xz*-plane when three-dimensional motion is considered, and families symmetric across just the *x*-axis when motion is constrained to lie in the orbital plane of the primaries. Although an individual three-dimensional trajectory in the CR3BP will not generally be symmetric across the *xy*-plane, any arc in the CR3BP will mirror a separate arc across the *xy*-plane

In families of periodic orbits that are simply symmetric across the *x*-axis or *xz*-plane, the symmetry can be exploited for the computation of the orbits. For symmetry across the *xz*-plane, the orbit must satisfy the mirror theorem [24]. The mirror theorem requires two conditions for periodicity: (i) the orbit must be continuous, and (ii) the orbit must cross the *xz*-plane perpendicularly twice. In terms of the state vectors, the *y*-component of position equals zero at the crossing of the *xz*-plane; the $\dot{x}$ and $\dot{z}$ components of velocity are also zero. In a planar, two-dimensional orbit, the *xz*-plane crossing is perpendicular to the *x*-axis. Given the requirements on the state vector at the perpendicular crossings, it is possible to select initial conditions for a targeting scheme to exploit this information. Consider the following initial state: $\overline{X}(\tau_0)=\begin{bmatrix}x_0 & 0 & z_0 & 0 & \dot{y}_0 & 0\end{bmatrix}^T$, one that crosses the *xz*-plane perpendicularly at the initial time. Integrating forward in time generally fails to produce a second perpendicular crossing of the *xz*-plane. The goal, then, of the differential corrections process is the determination of small variations in the initial *y*-velocity, $\delta\dot{y}_0$, integration time, $\delta\tau$, and initial position on the *xz*-plane, $\left(x_0+\delta x, z_0+\delta z\right)$, such that a second perpendicular crossing of the *xz*-plane occurs. Of course, in the planar case, variations in *z* are not considered. The differential corrections process yields the desired update of the initial state based on the fundamental targeting relationship in Equation 2.49. When time is variable, the relationship is expanded as,

$$\delta\overline{X}(\tau_f) = \Phi(\tau_f, \tau_0)\delta\overline{X}(\tau_0) + \begin{bmatrix} \frac{\partial x}{\partial \tau} & \frac{\partial y}{\partial \tau} & \frac{\partial z}{\partial \tau} & \frac{\partial \dot{x}}{\partial \tau} & \frac{\partial \dot{y}}{\partial \tau} & \frac{\partial \dot{z}}{\partial \tau} \end{bmatrix}^T \delta\tau \,. \qquad (2.52)$$

The computation of periodic orbits in the CR3BP that possess symmetry across the *xz*-plane is further simplified by assuming that only δx or δz is varied, while the remaining state is fixed at the initial value. If z_0 is assumed to be fixed, then Equation 2.52 can be further compacted and subsequently inverted to solve for the updates to the control parameters at the initial time, $\begin{bmatrix} \delta x_0 & \delta \dot{y}_0 & \delta\tau_0 \end{bmatrix}^T$, in terms of variations in the constraint variables, that is, the *x* and *z* components of velocity at the subsequent perpendicular crossing:

$$\begin{bmatrix} \delta x_0 \\ \delta \dot{y}_0 \\ \delta\tau_0 \end{bmatrix} = \begin{bmatrix} \phi_{21} & \phi_{25} & \dot{y}_f \\ \phi_{41} & \phi_{45} & \ddot{x}_f \\ \phi_{61} & \phi_{65} & \ddot{z}_f \end{bmatrix}^{-1} \begin{bmatrix} 0 \\ \delta \dot{x} \\ \delta \dot{z} \end{bmatrix}. \qquad (2.53)$$

A similar expression can be derived when the *x*-position coordinate is fixed. When the periodic orbit is assumed to lie in the *xy*-plane, the expression in Equation 2.53 reduces to the following form,

$$\begin{bmatrix} \delta \dot{y}_0 \\ \delta\tau_0 \end{bmatrix} = \begin{bmatrix} \phi_{25} & \dot{y}_f \\ \phi_{45} & \ddot{x}_f \end{bmatrix}^{-1} \begin{bmatrix} 0 \\ \delta \dot{x} \end{bmatrix}. \qquad (2.54)$$

Consideration of non-dimensional time, τ, as a variable, can be neglected if the numerical integration is terminated at the crossing of the *xz*-plane. This capability is common in many commercial numerical integration routines, which may further use a root solving method to determine the time as well as position and velocity states very accurately at the crossing of the *xz*-plane.

As an example of periodic orbits in the CR3BP that are symmetric across the *xz*-plane, consider the trajectory in Figures 2.5. In Figure 2.5, a three-dimensional periodic orbit, labeled as an L_2 halo orbit, is plotted in the Saturn-Enceladus system. This single

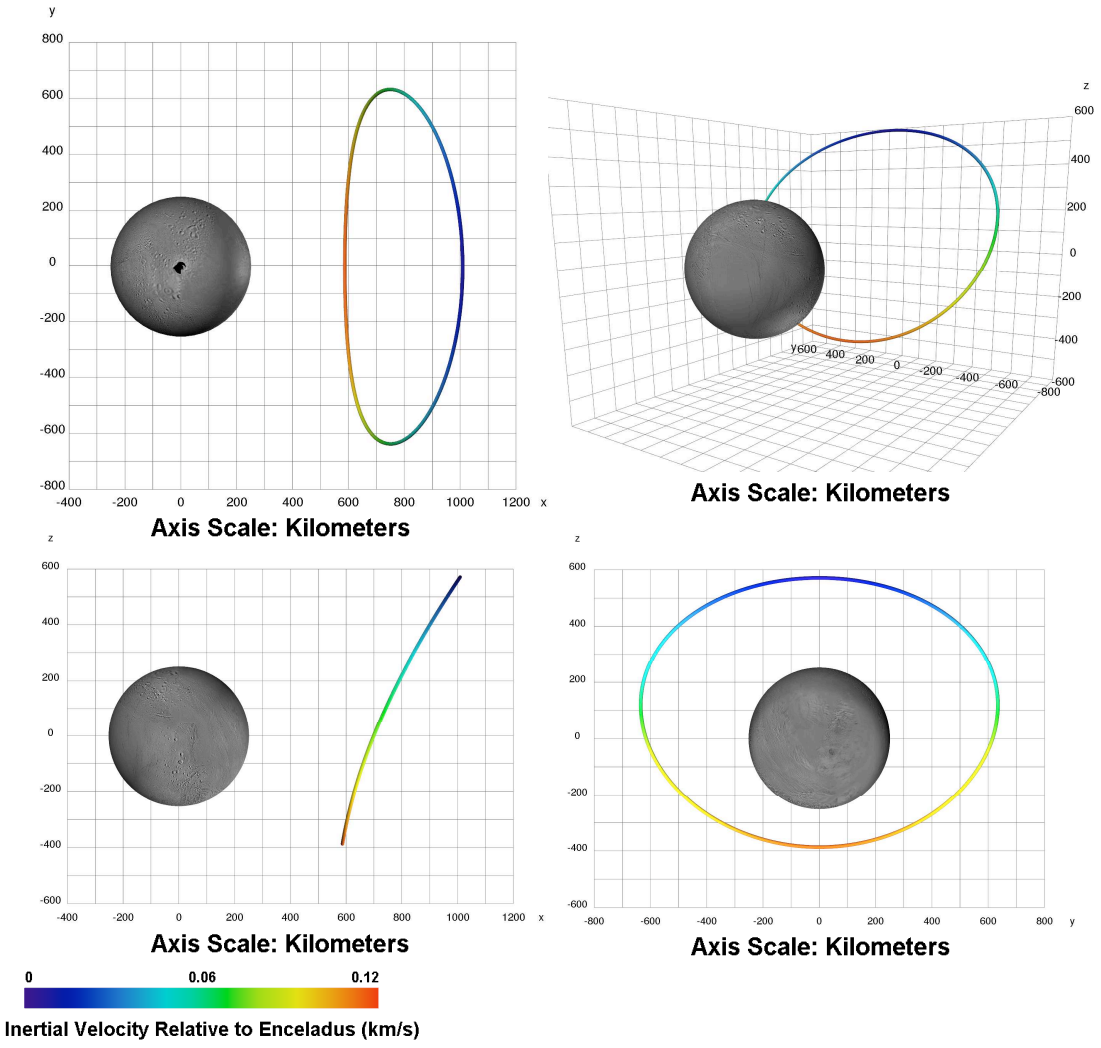

Figure 2.5 A periodic L_2 halo orbit in the Saturn-Enceladus CR3BP; plotted in the Enceladus-centered rotating reference frame.

orbit results from the previously described differential corrections process, where the initial approximation for the perpendicular velocity at the crossing of the *xz*-plane is obtained via a shooting method. Another example of a periodic orbit in the Saturn-Enceladus system is the planar trajectory in Figure 2.6. Unlike the previous example, this particular orbit has no direct association with the Lagrange equilibrium points. The orbit in Figure 2.6 is a 4:5 resonant orbit in the Saturn-Enceladus system. Along this

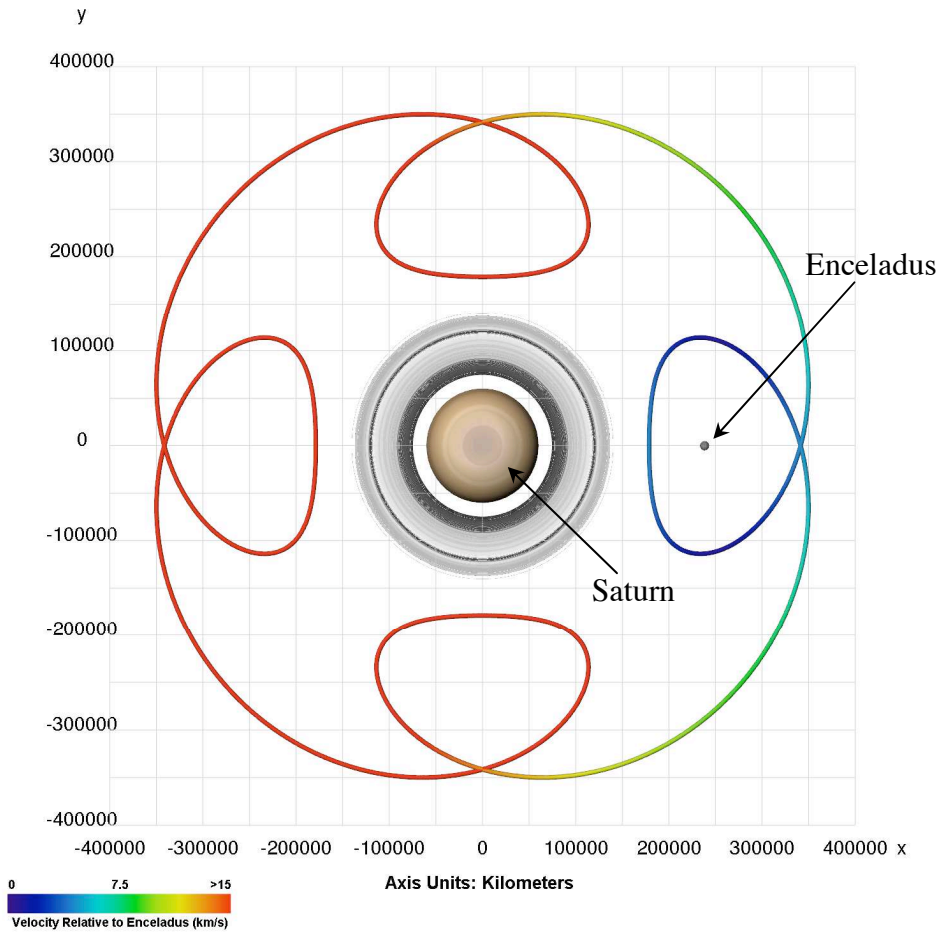

Figure 2.6 A periodic resonant orbit in the Saturn-Enceladus CR3BP; plotted in the rotating reference frame, with Enceladus enlarged 25× .

trajectory, the spacecraft completes four orbits of Saturn in the time required for Enceladus to complete five revolutions. Note also that the initial guess for the targeting routine originated with the x-axis crossing between Saturn and Enceladus. Then, the final targeted state lies at the x-axis crossing near $x \approx -180{,}000$ km. For this orbit, two additional non-perpendicular crossings of the x-axis occur, though integration is terminated at the third x-axis crossing (at the half-period of the orbit) to target a desired perpendicular crossing of the final periodic orbit.

Once a single symmetric periodic orbit is available in the CR3BP, it is often possible to easily compute an infinite number of nearby orbits that are in the same *family* of orbits. Using the same differential corrections process, the user can simply supply an initial

integration state that is very near in position to the perpendicular crossing of the known orbit, with the same velocity state perpendicular to the *xz*-plane at the new perturbed position coordinates. Assuming the states at the perpendicular crossing of the known periodic orbit and the targeted nearby orbit are sufficiently close, the velocity from the known orbit will generally be a good initial guess for the actual velocity on the new nearby orbit, though a differential corrector is still required to determine the exact velocity state for a later perpendicular crossing. This method of constructing a family of orbits is labeled a continuation process or continuation method.

2.2 Resonant Orbits in Mission Design

Though there are actually many types of orbital resonance, the focus in the current investigation is mean motion orbital resonance. Emphasis on multi-body mission design is a priority in this investigation, but orbital resonance is much more clearly defined in the two-body conic model. Thus, the definition of mean motion resonance is introduced within the context of the two-body model. Orbital resonance in the three-body problem logically follows.

In the two-body problem, there are three possible parameterizations of conic trajectories in the inertial frame that are grouped according to their energy level: elliptical orbits (of which circles are a special case), parabolic trajectories, and hyperbolic trajectories. Within the Saturn-centered two-body problem, parabolic and hyperbolic trajectories escape the vicinity of the attractive center and, thus, are not of interest in a discussion of orbital resonance. Circular and elliptical orbits are both closed and periodic trajectories relative to the inertial reference frame in the two-body problem. Circular orbits also remain closed and periodic in a rotating reference frame within the context of the two-body problem, regardless of the particular synodic rate. Elliptical orbits, however, generally fail to form a closed trajectory relative to a rotating reference frame, *unless* the rotating frame is either specifically selected or happens to possess a resonant orbital period.

To investigate two-body resonance, consider the introduction of a massless second primary, P_2 (either a planet or moon), in a circular orbit relative to P_1. A spacecraft is defined to be in orbital resonance with the massless second primary, P_2, when the spacecraft completes precisely p orbits around the first primary, P_1, in the same length of time that is required for P_2 to complete q orbits. In this definition, p and q are positive integers ($p,q \in \mathbb{N}$) and there is no restriction on which of the integers is larger. The particular resonance is often denoted as a $p:q$ resonance; by convention, the spacecraft is typically associated with the first integer, p, and the motion of the moon of interest (i.e., Enceladus, or some other Saturnian moon) is associated with the second integer, q. This type of orbital resonance is termed mean motion resonance because the ratio $p:q$ is equal to the ratio of the mean motion of each body, that is,

$$\frac{p}{q} = \frac{n_p}{n_q} = \frac{T_q}{T_p} = \frac{\left(\frac{1}{T_p}\right)}{\left(\frac{1}{T_q}\right)}, \tag{2.55}$$

where T_j and n_j are the minimal orbital period and mean motion of body *j*, respectively. The mean motion, n_j, depends only on the mass of the first primary and the semi-major axis of the orbit,

$$n_j = \sqrt{\frac{Gm_1}{a_j^{\,3}}}, \tag{2.56}$$

and the orbital period, T_j, is equal to the inverse of n_j. As P_2 is in circular motion relative to P_1, a rotating reference frame is defined similar to the frame definition in the CR3BP. The two primaries remain stationary along the *x*-axis of the rotating frame; the *z*-axis is parallel to the orbital angular momentum vector, and the *y*-axis completes the right handed triad. In this two-body rotating reference frame, a spacecraft in orbital

resonance with P_2 is also in a closed orbit relative to the rotating reference frame as well as the inertial frame. Physically, periodicity relative to the rotating frame demonstrates that the precise configuration of the spacecraft and the moon repeats once per resonant period. To clarify, the resonant period is simply the total time during which the spacecraft completes p orbits, or identically, the time required for P_2 to complete q orbits. As an example of resonance in the conic model, consider the 3:4 resonant orbit depicted in Figure 2.7. This resonant orbit is computed in the two-body Saturnian system, where Enceladus is temporarily assumed to be the massless particle, P_2, orbiting Saturn in a circular orbit at a distance equal to the moon's accepted value of semi-major axis. The red elliptical orbit of the spacecraft, plotted relative to the inertial reference frame on the left in Figure 2.7, approaches and intersects the circular blue orbit of

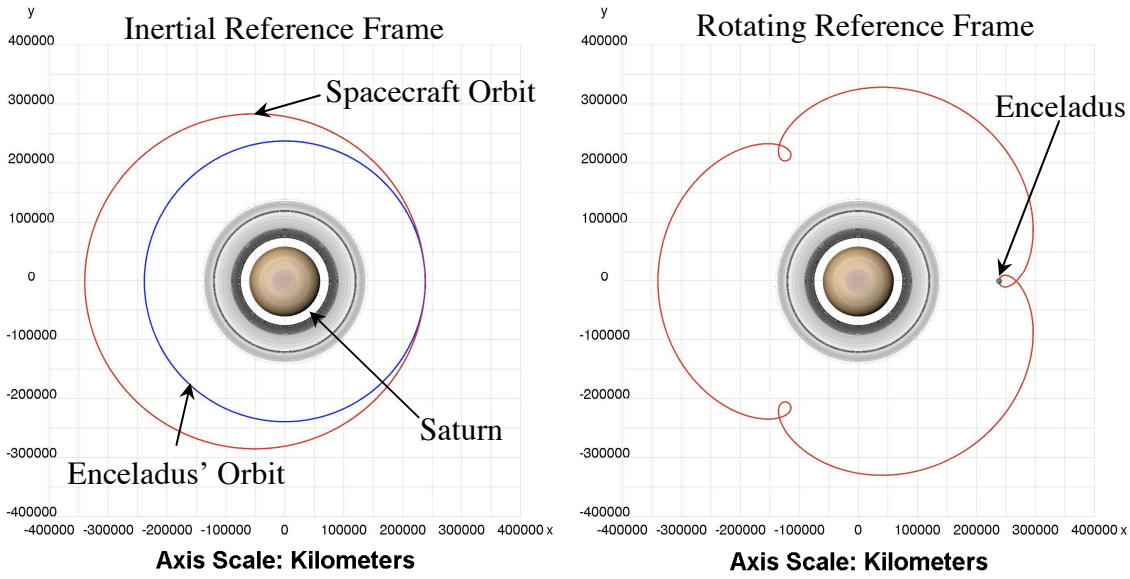

Figure 2.7 Inertial and rotating views – 3:4 (S/C: Enceladus) resonant orbit around Saturn, as calculated in the two-body model.

Enceladus. In the Saturn-Enceladus rotating reference frame, on the right in Figure 2.7, the same trajectory forms a three-leafed clover shape with the three inner loops corresponding to each of the three periapse passages of the spacecraft during a single resonant period. The flyby altitude associated with one of the periapse loops is just a matter of kilometers from the position of massless Enceladus, enlarged by a factor of

$25\times$ in Figure 2.7. Periapsis is, of course, the point along an elliptical orbit that is closest to the single gravitational source in the two-body model, just as apoapsis is the point of greatest separation. In the Saturnian system, periapsis and apoapsis along an orbit about Saturn are known as perikrone and apokrone. While orbits around Saturn in the CR3BP are generally not closed, the terms "perikrone" and "apokrone" still identify the points of closest approach and maximum separation between the spacecraft and the planet.

Though mean motion resonance is well defined and conceptually understood within the context of the conic model, orbital resonance is more complex when transitioned to the CR3BP. In the conic model, orbital resonance is exactly defined analytically in terms of the orbital periods of the two resonant bodies, consistent with Equation 2.55. However, in the restricted three-body problem, a $p:q$ resonant ratio is defined as,

$$\frac{p}{q} \approx \frac{T_q}{T_p} = \frac{n_p}{n_q}, \tag{2.57}$$

where the first body completes p orbits in *approximately* the same time interval that is required by the second body to complete q orbits relative to the three-body problem barycenter [25-27]. The approximate nature of the definition of orbital resonance in the CR3BP should not be mistaken to mean that precise orbital resonance does not exist in the restricted three-body problem. Rather, while closed and periodic resonant orbits *do* exist in the CR3BP, the ratio of the orbital periods will generally fail to form a rational fraction.

To clarify the physical meaning, orbital resonance in the three-body problem is characterized by configurations of the three bodies (the two primaries and the spacecraft) that repeat periodically. Thus, resonant orbits in the CR3BP produce closed trajectories as observed in the rotating reference frame. In light of this definition, some examples of resonant spacecraft trajectories are immediately evident. In particular, the Lagrange equilibrium points, by their very definition, complete precisely one revolution around the barycenter in the CR3BP during the synodic period of the rotating reference frame. Therefore, the Lagrange equilibrium points are in precisely 1:1 orbital resonance with

both primaries, P_1 and P_2, in the three-body system. In general, any closed trajectory relative to the rotating reference frame in the restricted three-body problem can potentially be understood to be in resonance with the system primaries, as the relative configuration of the bodies repeats periodically. However, not every orbit that is periodic relative to the rotating reference frame possesses an orbital period that is related through some rational fraction to the rotational period of the three-body problem primaries. For that reason, a trajectory in the CR3BP will be termed "resonant" only if the orbit satisfies one of two conditions: either the three-body orbit possesses a period that satisfies Equation 2.57 to some arbitrarily chosen level of accuracy, or the orbit is a member of a continuous family of orbits that includes many additional orbits with periods that satisfy Equation 2.57.

As an illustration of the differences between orbital resonance in the two-body and three-body models, the initial state corresponding to the resonant orbit from Figure 2.7 is transformed into rotating components, as in Equation 2.35, and then propagated forward

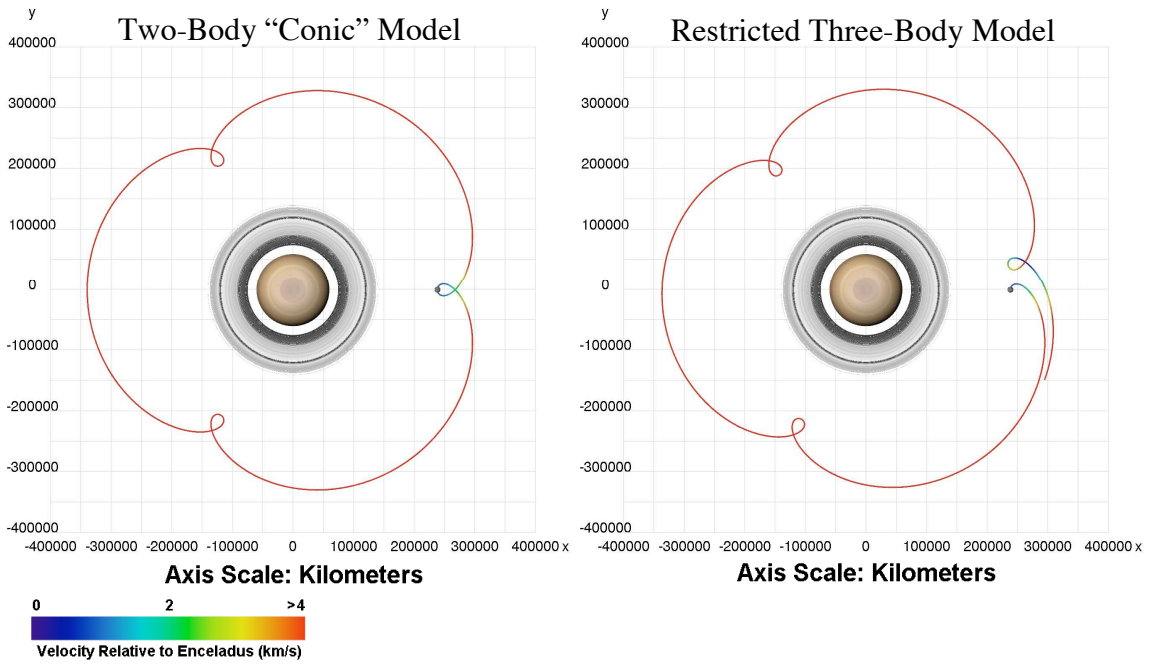

Figure 2.8 The initial state corresponding to a 3:4 (S/C: Enceladus) resonant orbit propagated in the conic model (left) and the restricted three-body problem (right).

in the CR3BP. Both the original periodic conic resonant orbit and the non-periodic trajectory resulting from integration in the CR3BP appear in Figure 2.8. Although the time-history of the spacecraft position can be determined analytically in the two-body model, both the conic and CR3BP trajectories in Figure 2.8 result from the numerical integration of the same initial spacecraft state. This plot demonstrates that any discrepancies between the trajectory result from the influence of an additional gravity field. Although Enceladus' gravity field is minute, the moon's perturbing influence on the trajectory in Figure 2.8 is clear. While the conic resonant orbit in Figure 2.8 remains closed to within some numerical tolerance, forward propagation of the same initial state in the CR3BP results in a trajectory that fails to precisely return to the same position relative to Enceladus after even a single resonant period.

The computation of resonant orbits in the restricted three-body problem is complicated by two important differences, when compared to the determination of their two-body counterparts. First, as a result of the perturbations due to P_2, the orbital period of a spacecraft in the CR3BP is not constant and the resonance ratio is not rational. As such, the initial conditions corresponding to these orbits are not available analytically. Secondly, the addition of the gravity field of the second primary results in perturbations that tend to shift a trajectory away from perfect resonance in the three-body problem, unless the resonant orbit is symmetric across the rotating *x*-axis. While resonant orbits that are not symmetric across the *x*-axis do exist, all resonant orbits in this investigation are computed by exploiting symmetry.

Resonant orbits in the restricted three-body problem are identified using the previously detailed differential corrections algorithm to target perpendicular crossings along a resonant trajectory. For several families of orbital resonance, multiple crossings of the *x*-axis occur prior to the targeted perpendicular crossing of the *x*-axis. Typically, geometric insight, along with user intuition, quickly yield the number of *x*-axis crossings that occur during a resonant period. The location and timing of the perpendicular crossings of the *x*-axis are also easily approximated. Due to the favorable symmetric structure of several families of resonant orbits, all resonant orbits in this analysis have

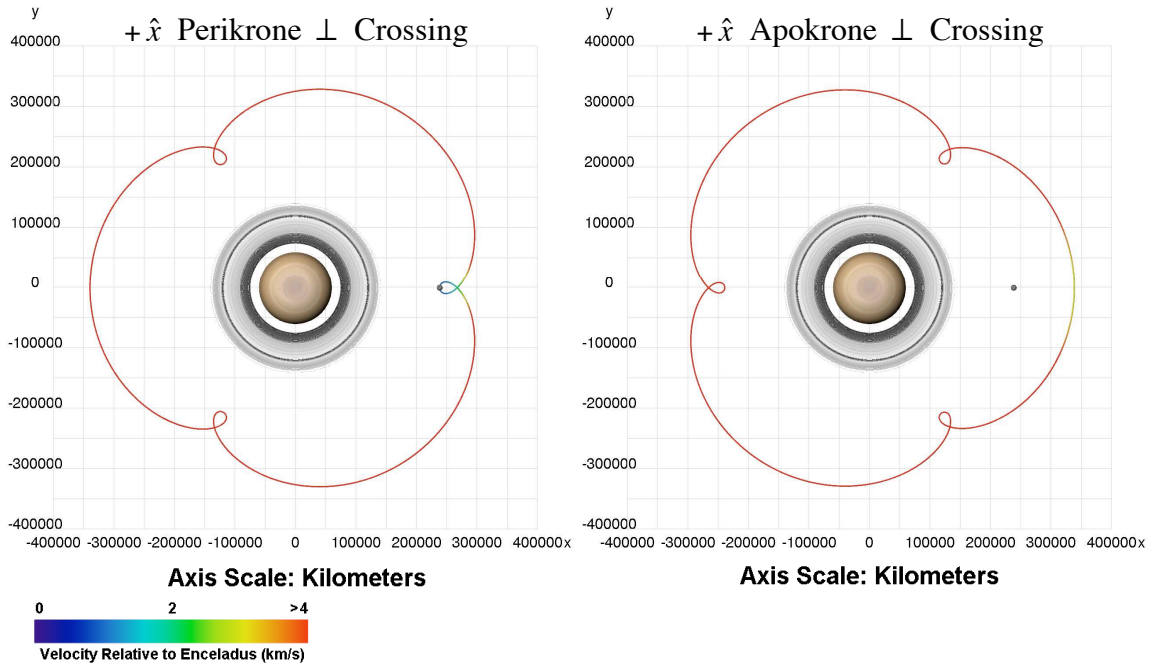

Figure 2.9 Resonant orbits from two distinct families characterized by varying perpendicular *x*-axis crossing locations.

perpendicular crossings of the rotating *x*-axis that occur during the perikrone or apokrone passage of the spacecraft.

In this investigation, there are two distinct families of resonant orbits that are possible for any given $p:q$ resonance. As is apparent in Figure 2.9, one of these families includes orbits with a perpendicular crossing of the *x*-axis at perikrone, notably on the positive side (the same side as P_2); the other family is characterized by orbits exhibiting a similar apokrone crossing. Generally, the family of resonant orbits that allows for frequent periodic flybys of P_2, specifically, the families of resonant orbits with a perikrone passage near P_2, offer geometries of particular interest in this investigation.

In identifying resonant orbits using a numerical differential corrections process, the user must supply an initial estimate, that represents an approximation to the resonant orbit, for the numerical integrator. The accuracy of this initial estimate typically affects the speed of convergence to the targeted resonant orbit. For restricted three-body systems where $m_2 << m_1$, as is true in the Saturn-Enceladus system, a spacecraft state generated

from the two-body conic resonant orbit is often a very accurate initial estimate. Using the conic model as an initial guess is particularly effective if the targeted resonant orbit does not pass close to P_2. Once a single resonant orbit is identified, it is possible to construct an entire family of resonant orbits via continuation. Two continuation options are possible: to initiate the targeter using the initial conditions from (i) the conic resonant orbits, or (ii) previously determined three-body resonant orbits.

2.3 Gravity-Assist Flyby Trajectories

The use of gravity-assist flyby trajectories has been integral to the successful design of many robotic missions to the outer solar system. Launching a spacecraft that inserts into a trajectory to the outer solar system tends to be expensive both energetically and in terms of the time-of-flight (TOF) required to reach distant planetary destinations. Incorporating a gravity-assist flyby into the design of an interplanetary trajectory is one common and highly successful way of reducing both the Earth departure energy and time-of-flight associated with such a trajectory. Gravity-assist trajectories have been used to intentionally alter the orbital path of several spacecraft launched during the last four decades, but the mechanics of a gravity-assist flyby have been understood by astronomers for over 150 years. Although no formal credit is generally given to a single astronomer for the discovery of the slingshot effect associated with a flyby trajectory, Leverrier (1847) was among the first to describe the gravity-assist mechanism [28, 29]. By 1889, Tisserand derived the commonly known *Tisserand relation,* that is,

$$\frac{1}{2a_1} + \sqrt{a_1(1-e_1^{\,2})}\cos(i_1) = \frac{1}{2a_2} + \sqrt{a_2(1-e_2^{\,2})}\cos(i_2)\,, \tag{2.58}$$

to calculate how the Keplarian elements associated with the orbit of a comet change as the result of a close encounter with a gravitational source [30]. In Equation 2.58, the subscripts on the Keplarian elements denote that the elements are associated with the orbit of a comet or spacecraft at a time prior to the flyby (i.e., a_1) and following the flyby

(i.e., a_2). The Tisserand criteria can be calculated from either side of the equality in Equation 2.58 as,

$$T \approx \frac{1}{2a} + \sqrt{a(1-e^2)}\cos(i). \tag{2.59}$$

The Tisserand criteria is, in fact, an analytical approximation of the more precise Jacobi Constant from Equation 2.30, and is commonly used in patched conic mission design. Both the Tisserand criteria and the Jacobi Constant are expressions of an energy-like quantity associated with a particular trajectory; a quantity that remains unchanged as a result of a gravity-assist flyby.

In the intervening years, between the work of Leverrier and Tisserand in the late 19th century and the advent of rocket propulsion in the mid-20th century, a number of additional astronomers independently repeated the derivation of many of the formulas associated with gravity-assist trajectories [28]. In the 1950's, Battin studied the application of gravity-assist flybys to provide free-return trajectories [29] and additional researchers in the 1960's, including Sedov (1960), Deerwester (1966), Niehoff (1966), and Sohn (1966), extended the application of gravit-assist flybys to the problem of interplanetary exploration [29, 31].

Several spacecraft in the 1960's travelled beyond the bounds of the Earth's gravity field on orbital paths that were subsequently altered by close flybys with Mars and Venus, including Mariner 2 (1962) and Mariner 4 (1964) as well as a number of the Soviet Venera, Zond, and Mars spacecraft. However, the first spacecraft to receive a more substantive boost in orbital energy as a result of gravity-assist flybys were Pioneer 10 (1972) and Pioneer 11 (1973) and later Voyager 1 and Voyager 2 (1977) [28, 29]. The close flybys of Jupiter, as well as the other gas giants, placed each of these four spacecraft on hyperbolic escape trajectories departing the solar system, though they were originally launched from Earth on less energetic elliptical orbits relative to the Sun [28].

Virtually every spacecraft sent beyond the orbit of Mars in the last half-century has flown on a trajectory that incorporated at least a close flyby of Jupiter, and some also included flybys of other planets including Mercury, Venus, Earth, and Mars. More recent

examples of interplanetary spacecraft to utilize gravity-assist flybys include Galileo (1989) [32], Ulysses (1990) [33], Cassini (1997) [34, 35], MESSENGER (2004) [36], and New Horizons (2006) [37]. In addition to interplanetary trajectories, patched conic techniques were also used to design the orbital *tours* of both the Jovian and Saturnian systems exploited by the Galileo and Cassini spacecraft, respectively [32, 35].

This investigation ultimately examines flybys in multi-body dynamical models, however, the dynamics of a gravity-assist flyby are most easily understood when formulated within the patched conic model. To this end, a brief introduction to gravity-assist flybys in the two-body model follows.

2.3.1 Gravity-Assist Flybys in a Patched Conic Dynamical Model

During a gravity-assist flyby in the patched conic model, orbital energy is transferred from a flyby body to a spacecraft, though the total energy of the planet-spacecraft system is conserved. To understand the dynamics of a gravity-assist flyby, consider a smaller gravitational source, P_2 of mass m_2, in orbit around a larger body, P_1 of mass m_1. This scenario is equally valid for either a planet orbiting the sun or a moon orbiting some planet. Suppose, now, that a spacecraft moving on an elliptical orbit around P_1 passes very near the smaller body, P_2. At the point of closest approach, the spacecraft is defined to be a distance r_c from the center of P_2. During the flyby, the spacecraft possesses a velocity of $\overline{V}_{S/C_{in}}$ relative to P_1. Similarly, the second primary, P_2, is in orbit with a velocity of $\overline{V}_2$ relative to P_1, as in Figure 2.10. Although both P_2 and the spacecraft are in circular or elliptical orbits relative to P_1, the close flyby of P_2 is represented in the two-body model as a hyperbolic flyby of P_2, where the asymptotic velocity of the spacecraft relative to P_2, at infinite distance, $\overline{V}_{\infty_{in}}$, is assumed to be the vector difference between $\overline{V}_{S/C_{in}}$ and $\overline{V}_2$,

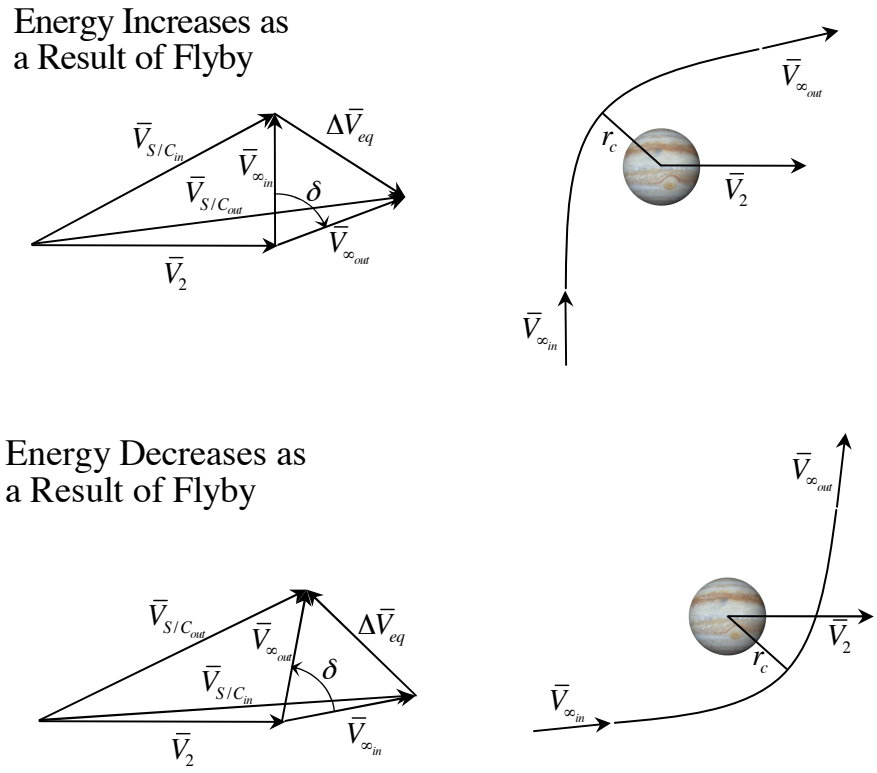

Figure 2.10 Vector diagrams associated with a gravity-assist flyby.

$$\bar{V}_{\infty_{in}} = \bar{V}_{S/C_{in}} - \bar{V}_2 . \tag{2.60}$$

During the hyperbolic flyby of P_2, the trajectory of the spacecraft will be rotated through a total bending angle of δ, though the magnitude of the velocity along the departure asymptote, $\bar{V}_{\infty_{out}}$, is equal to the magnitude of the velocity along the incoming asymptote, $\bar{V}_{\infty_{in}}$. The velocity of the spacecraft relative to P_1 following the flyby, $\bar{V}_{S/C_{out}}$, is calculated through the vector addition of the asymptotic departure velocity relative to P_2, $\bar{V}_{\infty_{out}}$, and the velocity of P_2 relative to P_1, that is,

$$\bar{V}_{S/C_{out}} = \bar{V}_{\infty_{out}} + \bar{V}_2 . \tag{2.61}$$

Using common relationships from the two-body model, it is possible to derive a relationship between the magnitude of the hyperbolic excess velocity, V_∞, the flyby distance, r_c, and the bending angle of the flyby hyperbolic trajectory, δ. This relationship,

$$\sin\frac{\delta}{2} = \frac{1}{\left(1+\frac{r_c V_\infty{}^2}{Gm_2}\right)}, \tag{2.62}$$

is known as the flyby equation.

The most useful way to measure the effect of a gravity-assist flyby is to quantify ΔV_{eq}, the equivalent change in the spacecraft velocity relative to P_1 as a result of the flyby. An examination of Figure 2.10 demonstrates that a larger bending angle, δ, is associated with larger values of $\Delta\bar{V}_{eq}$. As such, the equivalent change in velocity resulting from a flyby, $\Delta\bar{V}_{eq}$, can be increased by either decreasing the velocity of the spacecraft during the flyby or by decreasing the altitude of the flyby. This change in velocity can be directly calculated from V_∞ and r_c as,

$$\Delta V_{eq} = \frac{2V_\infty}{\left(1+\frac{r_c V_\infty{}^2}{Gm_2}\right)}. \tag{2.63}$$

Note that in Equation 2.63, ΔV_{eq} is not dependent on the bending angle, δ. Therefore, as long as the flyby distance, r_c, is known, calculation of the Keplarian elements associated with the hyperbolic orbit in the vicinity of P_2 is not necessary to determine ΔV_{eq}.

2.3.2 Definition of a Gravity-Assist Flyby in the Restricted Three-Body Problem

The patched conic formulation of gravity-assist trajectories is essentially an approximation of multi-body dynamical interactions. As such, it is reasonable to compare a gravity-assist trajectory represented in terms of a patched conic approximation to the results of a numerically simulated gravity-assist trajectory in a multi-body dynamical model. In this instance, gravity-assist trajectories in the CR3BP are examined. The most straightforward approach to quantify the effects of a gravity-assist flyby simulated in both the patched conic and three-body models, is through an examination of ΔV_{eq}. Of course, ΔV_{eq} varies depending on the geometry of the flyby and the characteristics of the spacecraft's approach trajectory, so several simulations are required in the CR3BP.

Unfortunately, the comparison of gravity-assist trajectories in the two-body and three-body models is hampered by the fact that ΔV_{eq}, V_∞, $\overline{V}_{S/C_{in}}$, $\overline{V}_{S/C_{out}}$ and δ are all quantities that are defined within the patched conic model, but are undefined in the CR3BP. Since it is possible to analyze flybys without computing δ, this parameter is ignored. However, both ΔV_{eq} and V_∞ must be defined relative to the CR3BP.

It is often desirable in mission design to quantify how close a spacecraft must pass to some gravitational body before the perturbations of that body become significant. One common approach for estimating the effective range of the gravitational influence due to a Saturnian moon is through the calculation of the Hill's sphere radius [30] associated with the moon, that is,

$$r_{Hills} = l^* \left(\frac{\mu}{3} \right)^{\frac{1}{3}}. \tag{2.64}$$

The Hill's sphere is an approximation of the range of the gravitational influence of the second primary in a restricted three-body system, for the case when the second primary is much less massive than the first primary; a distinctly accurate assumption when applied to Saturn and its moons. In Equation 2.64, μ is defined consistent with Equation 2.8.

Multiplication by l^*, the semi-major axis associated with the moon's orbit around Saturn, returns the non-dimensional Hill's sphere radius measured in terms of more meaningful physical units. The Hill's sphere is a good approximation of the closest possible distance that a spacecraft can approach relative to the flyby body, such that the gravitational influence of the flyby body is less significant than the influence of the first primary. Thus, the state of the spacecraft at the moments that it crosses into and out from the boundary of the Hill's sphere corresponding to P_2 are used in the calculation of ΔV_{eq}.

Note that the numerical integration of the flyby trajectory in the CR3BP is *not* terminated as the spacecraft crosses the Hill's sphere associated with the flyby body. Instead, the boundary of the Hill's sphere is used as a weigh-point in the integration, where the particular position and velocity state of both the spacecraft and the flyby body are noted and used to calculate the instantaneous orbital characteristics. In fact, three particular spacecraft states are isolated from the flyby simulation in the CR3BP. First, the state of the spacecraft is recorded as the spacecraft crosses into the Hill's sphere of the flyby body. Next, the particular spacecraft state and integration time associated with the closest approach of the spacecraft relative to the flyby body is noted, and finally, the spacecraft state as it exits the Hill's sphere of the flyby body is also noted.

Due to the gravitational influence of the larger primary, it is not sufficient to compare the velocity of the spacecraft as it enters the flyby body's Hill's sphere to the velocity as it exits the Hill's sphere, and use the difference between these two values as a simple means to calculate the ΔV_{eq} resulting from the flyby. In the CR3BP, the velocity of the spacecraft changes as it passes through the Hill's sphere of a moon both because of the gravitational influence of the second primary *and* because of the motion of the spacecraft along its orbit relative to the first primary. For a trajectory around Saturn that encounters a moon while the spacecraft is passing toward apokrone (i.e., the true anomaly of the spacecraft is between 0 and 180 degrees), the velocity of the spacecraft naturally decreases continuously through the transit of the Hill's sphere of the flyby body, regardless of the influence of the second primary. The spacecraft similarly exhibits a continuous increase in velocity as it approaches a flyby body during an inbound flyby. It

is for this reason that the particular integration time associated with the closest approach of the spacecraft to the flyby body is of such importance.

The computation of the ΔV_{eq} that results from a flyby during a simulation in the CR3BP occurs after the propagation of the gravity-assist flyby is completed. In essence, the ΔV_{eq} resulting from the flyby is determined by using the state of the spacecraft as it enters the Hill's sphere associated with P_2 to calculate the instantaneous Keplarian elements associated with the spacecraft orbit relative to the moon. This instantaneous measurement of the orbital characteristics is then used to predict the future velocity of the spacecraft at the moment of the spacecraft's closest approach to P_2. Similarly, the instantaneous Keplarian elements are calculated as the spacecraft exits the Hill's sphere, and the characteristics of the orbit at that moment are used for a prediction backwards in time of the velocity of the spacecraft along the two-body hyperbolic path at the time of closest approach to P_2. In general, the velocity at closest approach to P_2 predicted at the entrance to the flyby body's Hill's sphere is not equal to the predicted value at the spacecraft's exit from the Hill's sphere. It is the difference between these two predicted velocities at the closest approach point that define ΔV_{eq} as,

$$\Delta V_{eq} = \left| \overline{V}_{r_c\_in} - \overline{V}_{r_c\_out} \right|, \tag{2.65}$$

where $\overline{V}_{r_c\_in}$ is the velocity of the spacecraft at closest approach to P_2, as predicted from the spacecraft state upon entry to the Hill's sphere, and $\overline{V}_{r_c\_out}$ is the velocity at r_c as predicted at the exit from the Hill's sphere.

The two predicted velocity vectors in Equation 2.65, $\overline{V}_{r_c\_in}$ and $\overline{V}_{r_c\_out}$, are calculated from the position and velocity states of the spacecraft as well as some geometric intuition. First, the position and velocity of the spacecraft as it enters the Hill's sphere of P_2 are used to determine the instantaneous value of semi-latus rectum corresponding to the spacecraft orbit around Saturn,

$$p_{in} = \frac{\left(\left|\bar{r}_{in} \times \bar{v}_{in}\right|\right)^2}{Gm_1}, \tag{2.66}$$

where $\bar{r}_{in}$ is the inertial cartesian position vector of the spacecraft relative to Saturn and $\bar{v}_{in}$ is the corresponding orbital velocity. The magnitudes, r_{in}, v_{in}, and p_{in}, yield the semi-major axis and eccentricity of the instantaneous two-body orbit, that is,

$$a_{in} = -\frac{Gm_1}{v_{in}^{\ 2} - \frac{2Gm_1}{r_{in}}}, \tag{2.67}$$

$$e_{in} = \sqrt{1 - \frac{p_{in}}{a_{in}}}. \tag{2.68}$$

With the shape of the two-body orbit thus determined, the true anomaly of the spacecraft at the instant that it enters the P_2 Hill's sphere is calculated as,

$$\theta^*_{in} = \cos^{-1}\left(\frac{p_{in} - r_{in}}{r_{in} e_{in}}\right), \tag{2.69}$$

where the quadrant ambiguity associated with the inverse cosine in Equation 2.69 is resolved with user knowledge of the direction of spacecraft motion relative to Saturn. Next, using the instantaneous two-body orbit calculated at the entrance to the Hill's sphere, the true anomaly of the spacecraft at the moment of closest approach to the flyby body, $\theta^*_{r_c\_in}$, is determined as,

$$\theta^*_{r_c\_in} = \cos^{-1}\left(\frac{p_{in} - r_{cSat}}{r_{cSat} e_{in}}\right), \tag{2.70}$$

where r_{cSat} is the magnitude of the cartesian position vector of the spacecraft, relative to *Saturn*, at the moment of closest approach to the flyby body, the moment the spacecraft is a distance r_c from the flyby body in Figure 2.10. With the calculation of these quantities,

the predicted velocity of the spacecraft at the moment of closest approach to P_2 , that is $\overline{V}_{r_c\_in}$, is computed using the $\dot{f}$ and $\dot{g}$ relationships [30], as,

$$\overline{V}_{r_c\_in} = \dot{f} \cdot \overline{r}_{in} + \dot{g} \cdot \overline{v}_{in} , \tag{2.71}$$

where

$$\dot{f} = \left\{ \frac{\overline{r}_{in} \cdot \overline{v}_{in}}{p_{in} r_{in}} \left[1 - \cos\left(\theta^*_{r_c\_in} - \theta^*_{in} \right) \right] - \frac{1}{r_{in}} \sqrt{\frac{Gm_1}{p_{in}}} \sin\left(\theta^*_{r_c\_in} - \theta^*_{in} \right) \right\} , \tag{2.72}$$

$$\dot{g} = \left\{ 1 - \frac{r_{in}}{p_{in}} \left[1 - \cos\left(\theta^*_{r_c\_in} - \theta^*_{in} \right) \right] \right\} . \tag{2.73}$$

Note that the process used to determine $\overline{V}_{r_c\_in}$, which is based on the state of the spacecraft at the moment it enters the P_2 Hill's sphere, can be repeated at the point that the spacecraft exits the Hill's sphere to obtain $\overline{V}_{r_c\_out}$. With the definition of $\overline{V}_{r_c\_in}$ and $\overline{V}_{r_c\_out}$ thus complete, it is finally possible to determine ΔV_{eq} , the equivalent change in velocity imparted by the gravity-assist flyby within the context of a three-body model, using Equation 2.65. The results of the comparison between the two-body and three-body modeling of gravity-assist flyby trajectories in the Saturnian system are presented via specific examples in Chapter 5.

3. ORBITS IN THE VICINITY OF ENCELADUS

A flagship class mission to Enceladus will almost certainly require a long tour of the Saturnian system. It is likely that many gravity-assist flybys of the Saturnian moons will be incorporated to modify the orbital energy of the spacecraft relative to Saturn, such that the arrival at Enceladus allows a reasonable orbit insertion maneuver or, at the very least, a low velocity flyby. However, before designing a tour of the Saturnian system and subsequent transfer 'down' to Enceladus, some basic understanding of the possible motion in the vicinity of the small moon is desirable.

There are many mission specific considerations involved in designing a science orbit near Enceladus. The ideal science orbit of Enceladus must be feasible and must also balance the science possibilities with the engineering realities. Examining a small subset of possible Enceladus orbits is useful to quantify the orbital energy and the velocity relative to Enceladus that support an Enceladus orbiter.

As detailed in the Enceladus Flagship Mission Concept Study [4], the science objectives for an Enceladus orbiter include global mapping (morphological, compositional, and thermal mapping), as well as laser altimetry measurements, magnetic sounding, precise gravity field measurements, and low velocity sampling of the ice plumes at Enceladus' south-pole. These science objectives are best accomplished from an Enceladus orbit that provides both low velocity, relative to Enceladus' surface, and low altitude. Given these goals, a number of different Enceladus orbit scenarios are investigated.

3.1 Selection of Dynamical Model

The use of a full ephemeris model to represent the Saturnian system, one incorporating every conceivable perturbation – from general relativistic acceleration to the slight gravitational influence of distant Pluto – certainly yields the most accurate description of the expected behavior of a spacecraft in this system. However, it is also true that an investigation using only the full ephemeris model is unlikely to expand the general understanding or yield insight into the dynamical structure of the Saturnian system. A simpler dynamical model offers a broader qualitative understanding of the spacecraft dynamics in the Saturnian system. The challenge then, in modeling the Saturnian system, lies in determining the appropriate balance between simplifications and assumptions that still allow sufficient dynamical insight, and the inclusion of significant perturbing influences to provide physical relevance for design in the actual Saturnian system. In response to these conflicting goals, this analysis employs models of the Saturnian system that incorporate several key simplifying assumptions. However, the most useful assumptions depend upon the dynamical regime within the Saturnian system to which the model is applied. For example, the CR3BP is used to model the motion of a spacecraft in orbit around Enceladus. An alternate model, incorporating the gravitational influence of not only Saturn and Enceladus, but four additional larger moons, is more appropriate to initiate the analysis of a transfer to Enceladus by means of multiple gravity-assist flybys.

3.2 The Restricted Three-Body Problem and the Saturn-Enceladus System

At first glance, the application of the CR3BP to the Saturn-Enceladus system may appear to be an inadequate model for the Saturnian system. Including the gravity of tiny Enceladus, while neglecting the gravitational influence of mighty Titan, a moon some three orders of magnitude more massive than Enceladus, may quickly lead an external observer to object that this model bears no resemblance to the actual Saturnian system. However, observational information reflecting the dynamics of Saturn and its moons,

provided by both Earth-based astronomers and NASA robotic spacecraft, demonstrate several instances of dynamical behavior that is predicted by the CR3BP. For example, Dione, a Saturnian moon that is just ten times the mass of Enceladus and lies just ~1.5 times further from Saturn, possesses two of its own Trojan moons [38]. These two moons, Helene and Polydeuces, revolve around Saturn along orbital paths that keep them both locked in the vicinity of the Saturn-Dione L_4 and L_5 Lagrange points, respectively [38, 39]. In addition, the Saturnian moon, Tethys, only five times the mass of Enceladus, is also associated with two of its own Trojan moons, Telesto and Calypso, located near the Saturn-Tethys L_4 and L_5 points, respectively [39]. The motion of these four small Trojan bodies in the vicinity of the equilateral Lagrange points is predicted by the CR3BP. While the three-body effects alone are insufficient to completely explain the orbital motion of any of these four Trojan moons, the fact that these Lagrange point orbiting satellites, predicted in the Saturn-Dione and Saturn-Tethys three-body systems, can exist side-by-side in a single planetary system is a very cogent demonstration that the model in the CR3BP can be successfully applied to particular regions within the Saturnian system. While neither Cassini nor either of the Voyager spacecraft have identified any Trojan "moons" at the Saturn-Enceladus equilateral libration points, there is direct physical evidence supporting the validity of using the CR3BP to model the Saturn-Enceladus system. High angular resolution observations by one ground-based astronomer [40] identified a faint transient arc in the vicinity of Saturn's E-Ring; the arc is interpreted to have resulted from the collision of a large ice block with smaller ice fragments trapped near the Saturn-Enceladus L_4 Lagrange point. If this hypothesis is verified, it provides further justification of the valid application of the CR3BP to the Saturn-Enceladus system. The main focus of this investigation is gaining access to the vicinity of Enceladus, but reaching that goal includes the application of the CR3BP to systems involving Saturn and one additional moon consisting of either Tethys, Dione, Rhea, or Titan.

3.2.1 Planar Orbits in the Saturn-Enceladus Restricted Three-Body Problem

Modeling the Saturn-Enceladus system in terms of the CR3BP possesses several advantages over other models. Unlike some higher fidelity models, it is possible to identify *periodic* solutions in the CR3BP, and these solutions may become quasi-periodic trajectories in the full ephemeris system. An infinite number of periodic orbits exist in the CR3BP, and a suitable differential corrections scheme yields orbital periodicity for a wide variety of initial conditions.

In the Saturn-Enceladus restricted three-body system, the requisite families of Lagrange points orbits are generated as an illustration of the types of periodic orbits that are available for use in observing the surface of Enceladus. Orbits from the L_1 and L_2 Lyapunov families in the Saturn-Enceladus CR3BP are plotted in Figure 3.1. The orbits in Figure 3.1 are coplanar with Enceladus' equatorial plane; this plane is assumed to coincide with the plane of Enceladus' orbital motion around Saturn. The color along each orbit represents the magnitude of the inertial velocity of the spacecraft relative to Enceladus. The Lyapunov orbits revolve around the L_1 and L_2 Lagrange points in a clockwise ($-z$-axis rotation) direction as viewed from above the orbital plane in the Saturn-Enceladus rotating frame. Approximate initial conditions for an arbitrarily-sized Lyapunov orbit from each family are determined using a shooting method; a targeting scheme then yields a periodic orbit. Given a single orbit, additional orbits in a Lyapunov family are constructed using a continuation process. To maintain feasibility, each Lyapunov orbit family is terminated when the orbital path passes Enceladus at an altitude below the mean radius of the moon. While fewer than 20 members of each Lyapunov family appear in Figure 3.1, there are actually an infinite number of periodic orbits in each family.

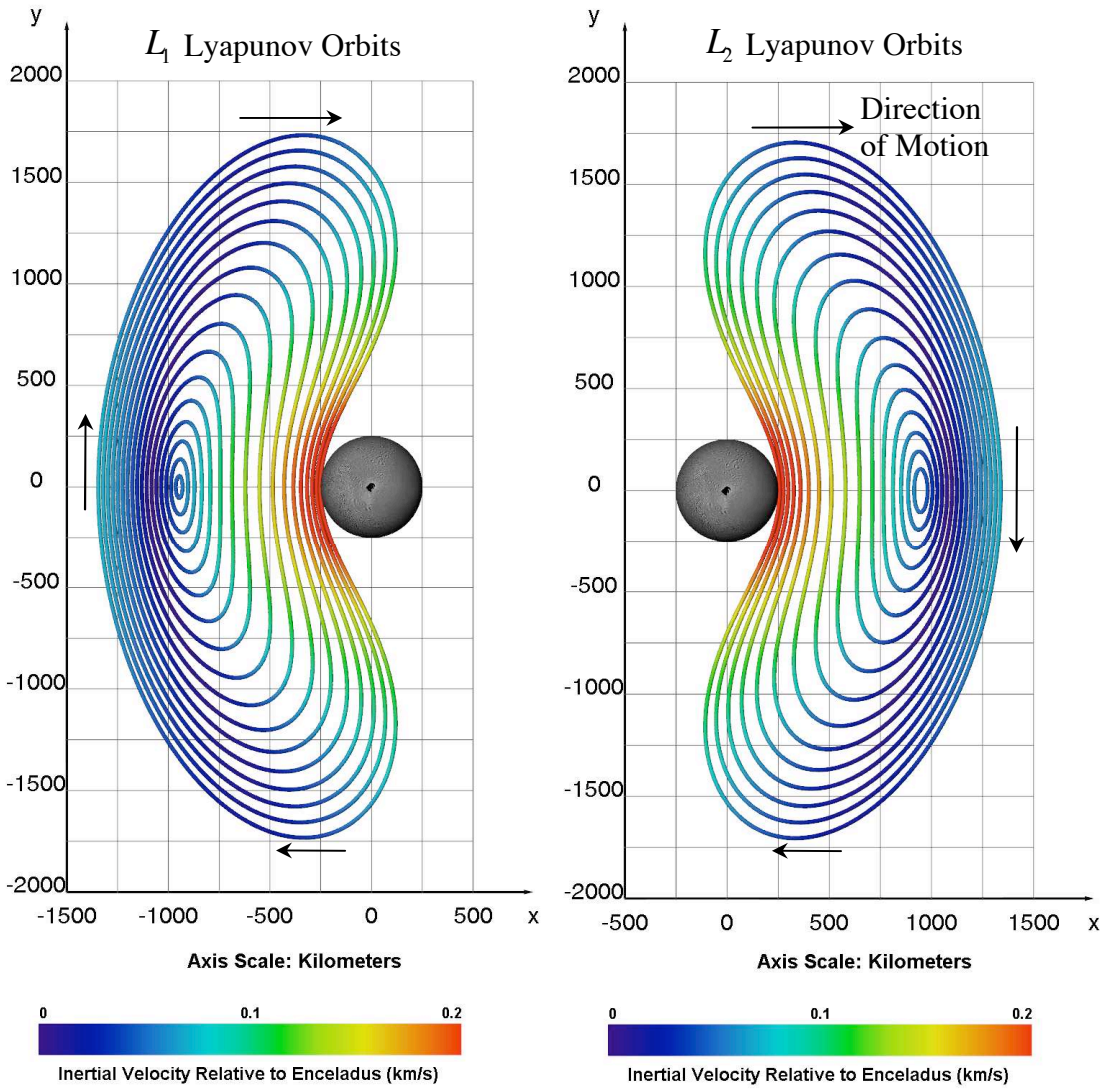

Figure 3.1 Rotating reference frame view of the Saturn-Enceladus L_1 and L_2 Lyapunov orbit families.

Libration point orbits are not the only closed and periodic orbits in the CR3BP. As an example of closed orbits in the Saturn-Enceladus rotating frame that do not revolve around any of the Lagrange points, consider the family of planar orbits in Figure 3.2. The nearly elliptical orbits from Figure 3.2 are centered on Enceladus and are, in fact, in orbital resonance with Enceladus. As such, the trajectories in Figure 3.2 are mildly eccentric orbits relative to Saturn, with perikrone only marginally closer to Saturn

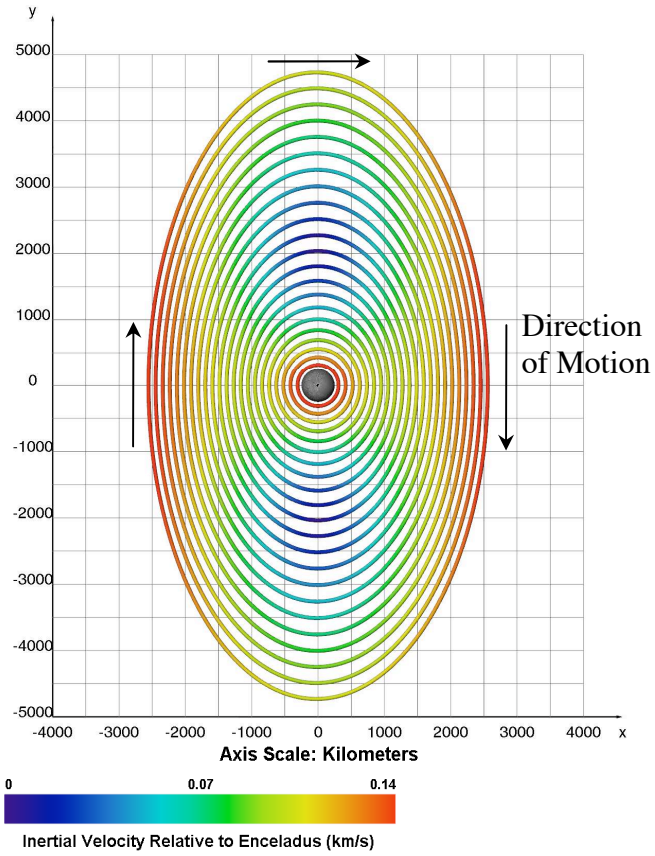

Figure 3.2 Enceladus-centered, rotating reference frame view of a planar 1:1 (Spacecraft: Enceladus) mean motion resonant orbit family.

than Enceladus and apokrone similarly more distant from Saturn than the moon. As a result of this orbital resonance, a spacecraft moving along one of the orbits from Figure 3.2 displays prograde motion around Saturn, but in a retrograde orbit with respect to Enceladus, as viewed in the Enceladus-centered rotating reference frame. In Figure 3.2, line color once again supplies a measure of the inertial velocity of the spacecraft relative to Enceladus, and Saturn would be located at $x \approx -280{,}000$ km.

3.2.2 Three-Dimensional Periodic Orbits in the Saturn-Enceladus Circular Restricted Three-Body Problem

Most of the scientific interest in Enceladus relates to the geologic activity at the moon's south-pole. Thus, the Lyapunov orbits and the resonant orbits in Figure 3.2, located in the Enceladus equatorial plane, are not ideal for scientific purposes, though both options do still provide excellent visibility of Enceladus' equatorial regions. The Lyapunov orbits are also valuable in the generation of additional families of periodic orbits that prove more favorable for mission science. Both the L_1 and L_2 Lyapunov families include orbits that intersect additional families of three-dimensional periodic orbits. The two families of orbits intersect in a single bifurcating orbit that is a common member of both families. A bifurcating orbit can be detected through an examination of the eigenvalues of the monodromy matrix (i.e., the state transition matrix evaluated at the end of one complete orbital period). A bifurcation of the orbits is visible in the monodromy matrix as a sudden change in the character of the eigenvalues. Stability characteristics change as eigenvalues depart from or arrive at the unit circle in the complex plane.

Table 3.1 Initial conditions corresponding to the halo family-Lyapunov family bifurcating orbits in the Saturn-Enceladus system.

	x (km)	$\dot{y}$ (km/s)	Period (days)
L_1 Halo/Lyapunov	236890.32827	0.04444	0.670308
L_2 Halo/Lyapunov	239012.77208	-0.04603	0.674707

Two well known families of orbits in the CR3BP with an out-of-plane component are the L_1 and L_2 halo orbit families. These halo families bifurcate from the L_1 and L_2 Lyapunov families at the orbits recorded in Table 3.1. Example members from these halo orbit families for the Saturn-Enceladus system are plotted in Figures 3.3 and 3.4. The halo orbits are actually mirror families. For each three-dimensional periodic orbit with an out-of-plane component, a mirror image exists across the *xy*-plane. The halo orbit families in Figure 3.3 and 3.4 are both labeled "southern" halo families since the orbits

extend further in the $-z$ direction than the $+z$ direction. "Northern" families of halo orbits are symmetric across the xy-plane with the "southern" halo orbits. Some of the halo orbits that most closely approach Enceladus could be potentially useful for achieving the science goals involving Enceladus south-pole visibility.

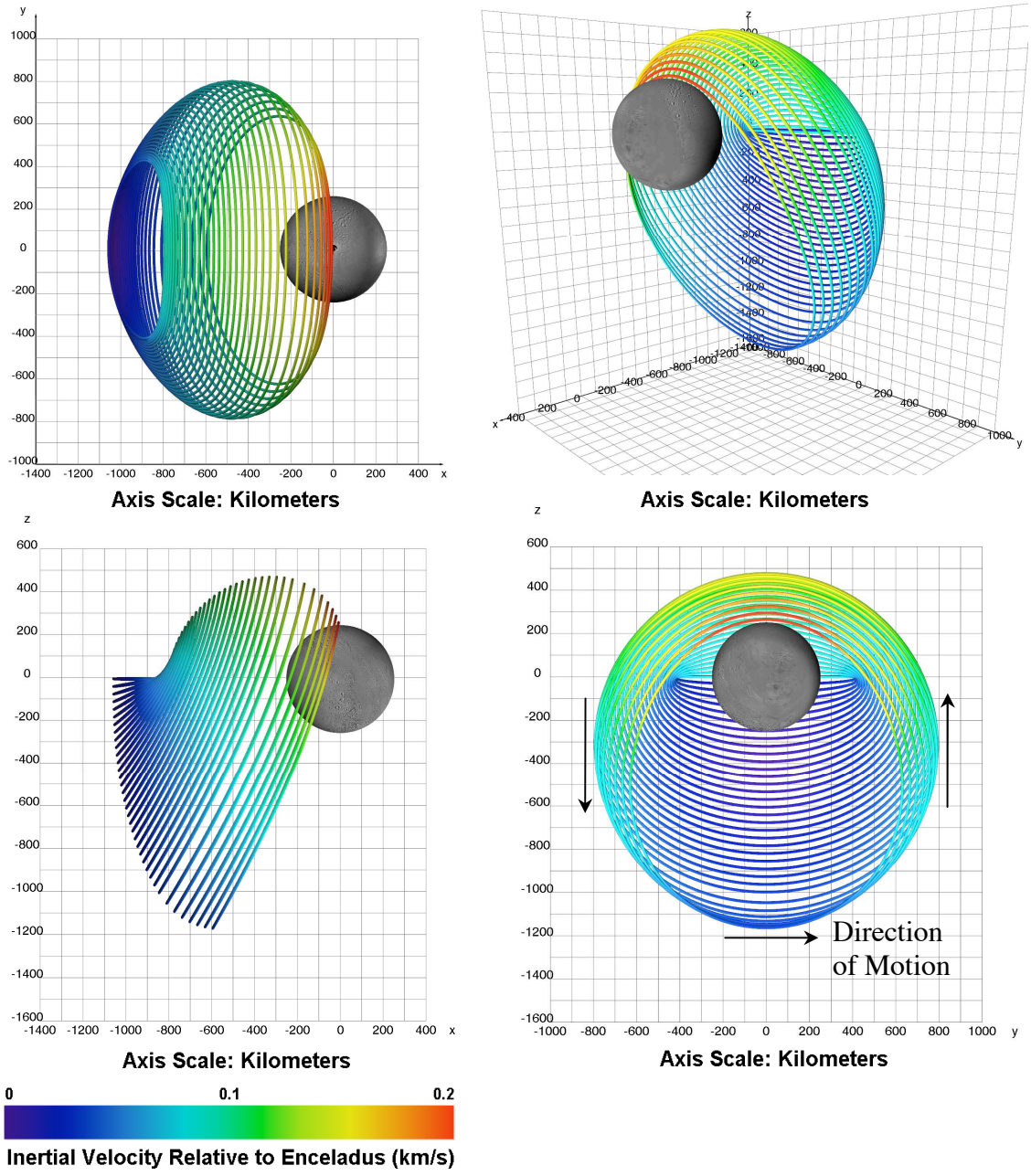

Figure 3.3 Several L_1 halo orbits in the Enceladus-centered rotating reference frame of the Saturn-Enceladus CR3BP.

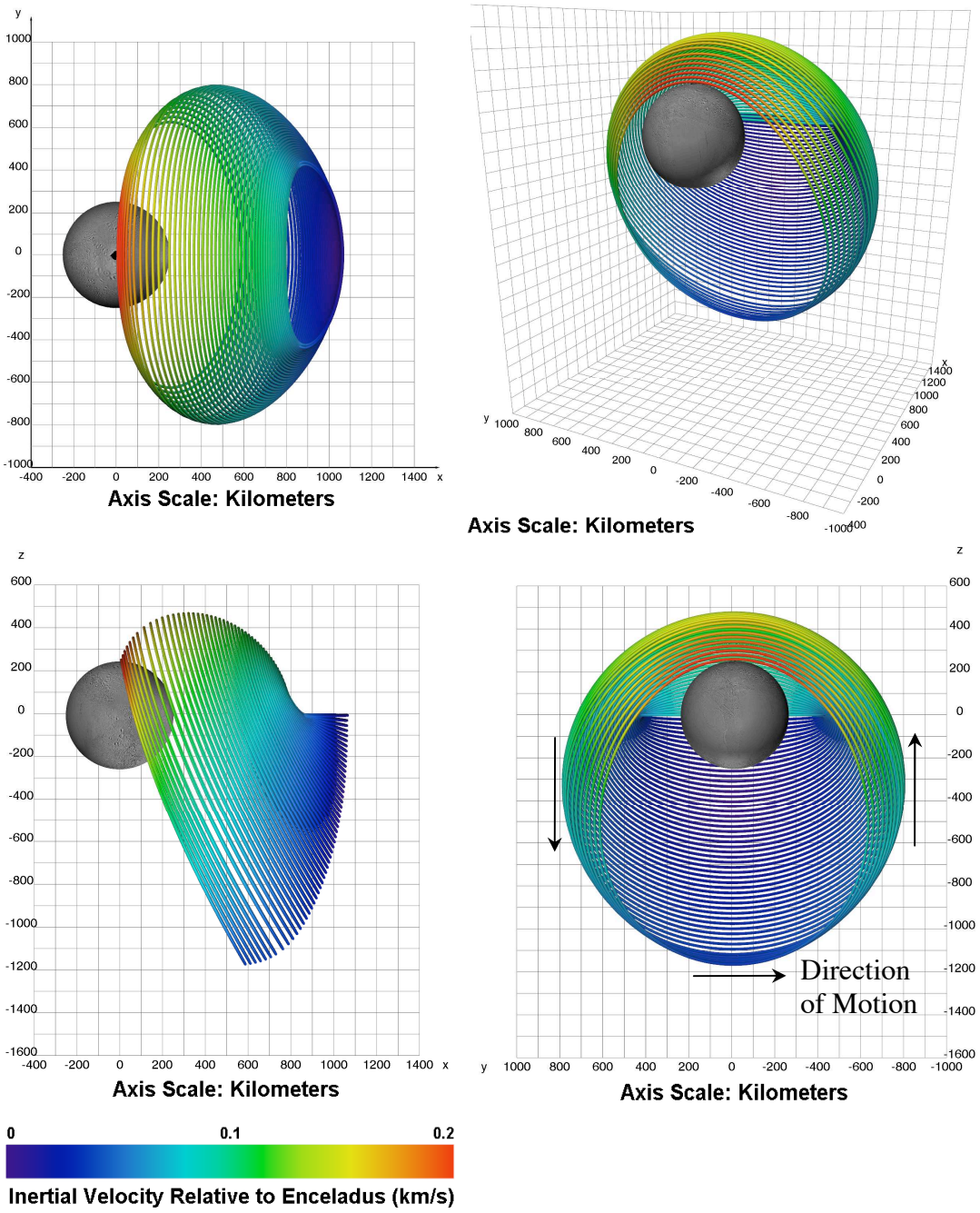

Figure 3.4 Several L_2 halo orbits in the Enceladus-centered rotating reference frame of the Saturn-Enceladus CR3BP.

It is clear in Figures 3.3 and 3.4 that orbits with the largest out-of-plane excursions also pass just tens of kilometers above Enceladus' north-pole. The corresponding orbits in the northern families of halo orbits pass similarly close to Enceladus' south-pole.

However, while Enceladus' south-pole is the primary science target, minimizing the flyby distance relative to the pole may not be the most practical or desirable condition for an Enceladus orbit. A flyby distance just tens of kilometers below the Enceladus south-pole improves image resolution of the moon, but it also minimizes the length of time available to collect science data and potentially increases the risk for any spacecraft passing directly through the icy plumes emanating from Enceladus south-pole. As such, orbits from the southern halo families plotted in Figures 3.3 and 3.4 offer a time and distance trade-off over their northern counterparts; spacecraft on the southern halo orbits spend significantly more time above the horizon, as viewed from Enceladus' south-pole, and the spacecraft remains relatively far from the icy particulate from Enceladus geysers. The halo orbits plotted in Figures 3.3 and 3.4 are periodic orbits in the vicinity of Enceladus and many of the science objectives identified in the Enceladus Flagship Mission Study [4] can be accomplished from a baseline trajectory incorporating halo orbits. However, there are other orbital options as well.

3.2.3 Evolution of Nearly Circular Orbits around Enceladus

Global mapping of an arbitrary solar system body can be efficiently accomplished using a polar-orbiting spacecraft. A circular polar orbit benefits from the natural rotation of the central body to allow for low altitude flyovers of the entire surface. Polar orbits are simulated in the Saturn-Enceladus restricted three-body model to investigate the feasibility of using these orbits for Enceladus science observations. Initial spacecraft states are selected within the Enceladus conic model to insert the spacecraft into an approximately polar circular orbit relative to Enceladus. The initial conditions to deliver a spacecraft into the nearly-circular polar orbits, recorded in Table 3.2, are defined with Enceladus altitudes of ~150 km (r = 406 km); this altitude value is arbitrarily selected to be within the 100-200 km range identified as acceptable in the Enceladus Flagship Mission Concept Study [4].

Table 3.2 Enceladus polar orbit characteristics for various initial values of Right Ascension of the Ascending Node (RAAN).

RAAN (deg)	Mean Relative Velocity Prior to Impact (m/s)	Time to Collision (days)	Simulation Time (days)
0	153.49	1.32	2
15	152.97	1.32	2
30	153.43	1.54	2
45	138.75	1.75	2
60	147.68	3.25	4
75	145.68	2.45	3
90	163.00	2.02	3

A selection of the resulting orbital trajectories propagated from the initial conditions in Table 3.2 appear in Figure 3.5. The difference between the sets of initial conditions corresponding to the four simulations in Figure 3.5 is the value of the Right Ascension of the Ascending Node (RAAN). The RAAN is measured from the $+x$-axis. In this model, the $+x$-axis possesses neither physical nor astronomical significance, so the RAAN is not measured relative to a specific astronomical epoch. The plots in Figure 3.5 result from varying the value of RAAN in 30^o increments (0^o, 30^o, 60^o, and 90^o from top-left to bottom-right) measured around the $+z$-axis from the $+x$-axis. Colors along the trajectories provide a measure of the inertial velocity of the spacecraft relative to the center of Enceladus. Note that while the plots of the Lyapunov and halo orbits in Figure 3.1-3.4 depict orbits relative to the Saturn-Enceladus rotating frame, the orbits in Figure 3.5 are plotted in the Enceladus-centered *inertial* frame. It is apparent, from a cursory examination of Figure 3.5, that the nearly "circular" polar orbits around Enceladus actually impact the surface of the moon within a few days (see Table 3.2). Each of the simulations listed in Table 3.2 results in an Enceladus collision in less than four days.

The four trajectories in Figure 3.5 demonstrate that varying the value of the RAAN angle, for orbits that are inclined 90 degrees relative to the Enceladus equatorial plane, does very little to prevent the spacecraft from quickly colliding with Enceladus. These results are not unexpected since the perturbing influence of nearby Saturn has a very

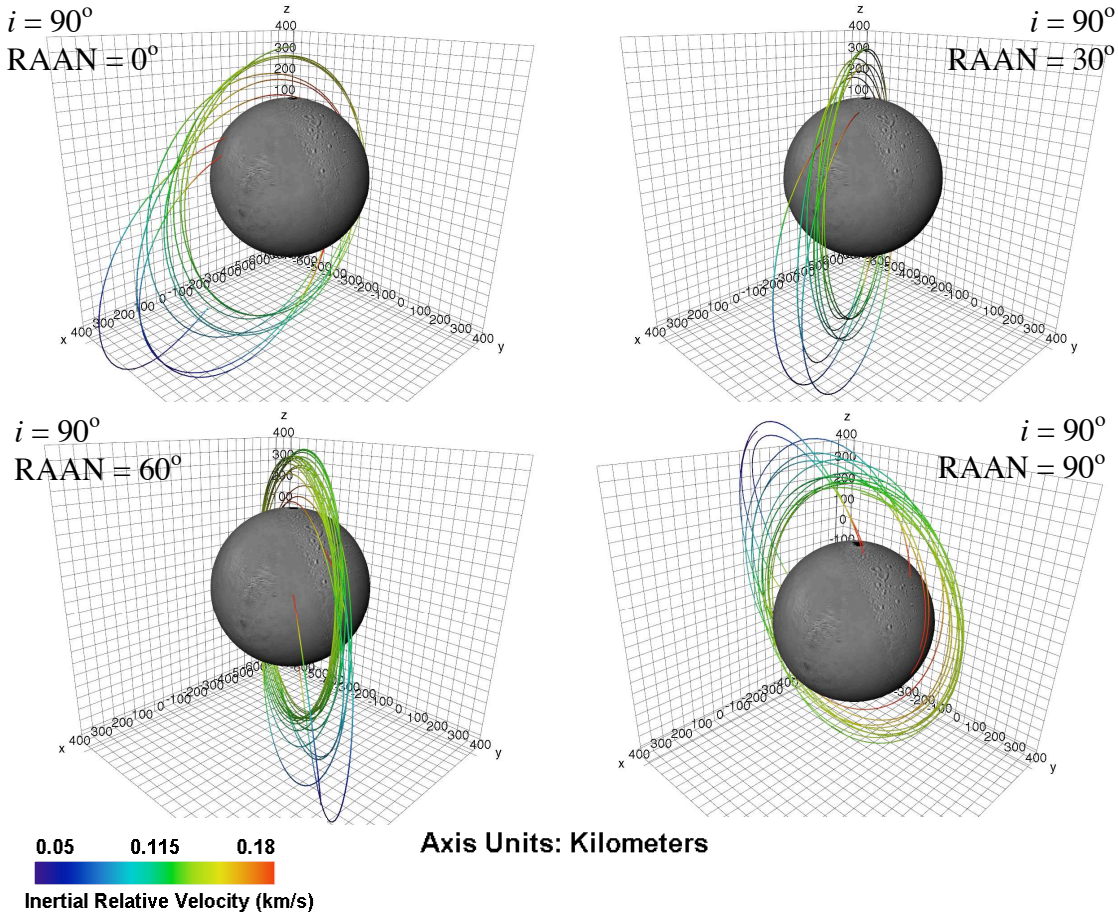

Figure 3.5 Enceladus polar orbits plotted in the Enceladus-centered inertial reference frame.

significant influence on the trajectory of the spacecraft. The restricted three-body model of the Saturnian system neglects the influence of both the Enceladus gravity harmonics and the J2 perturbation resulting from Saturn's oblateness, but the simplified model is sufficient to conclude that any circular-polar Enceladus orbit requires station keeping maneuvers, perhaps multiple times daily [4].

A circular polar orbit around Enceladus creates some challenges for implementation, yet, lower orbital inclinations may yield a circular Enceladus orbit that does not impact Enceladus within a relatively short period of time. Thus, several additional orientations of a circular orbit around Enceladus are examined for feasibility. Various combinations of orbital inclinations and RAAN are used as initial states in simulations that are summarized in Table 3.3 and propagated in Figure 3.6.

Table 3.3 Enceladus orbit propagations for varying inclinations and values of RAAN.

Inclination (deg)	RAAN (deg)	Mean Relative Velocity Prior to Impact (m/s)	Time to Collision (days)	Simulation Time (days)
0	90	139.43	N/A	100
15	90	138.98	N/A	100
30	90	138.28	N/A	100
45	90	146.03	5.03	7
60	90	172.60	2.81	5
75	90	287.74	1.33	5
90	90	164.98	0.65	1
0	0	134.90	N/A	100
15	0	134.22	N/A	100
30	0	134.50	N/A	100
45	0	143.99	2.31	3
60	0	141.57	5.18	6
75	0	145.89	1.53	2
90	0	141.56	0.95	1

In the CR3BP, any initial orbit that lies precisely in the *xy*-plane, the plane defined by both Enceladus' equator and its orbit around Saturn, remains permanently in the same plane, since the dynamical model cannot introduce perturbations or numerical errors in the $\pm z$ direction. Two examples from Figure 3.6 reflect this fact, i.e., the simulations with an initial value of inclination equal to zero remain precisely planar throughout the 100-day numerical propagation. A similar orbit in the actual Saturnian system will vary from this plane by some small amount. Several simulations are propagated for 100 days to explore the trade-offs between combinations of inclination and RAAN, and the resulting dynamical behavior of the spacecraft. These simulations demonstrate that a roughly circular orbit, at an altitude 150 km, does not impact the moon or depart the vicinity of Enceladus within 100 days, regardless of the RAAN value, as long as the initial orbital inclination is less than 45 degrees.

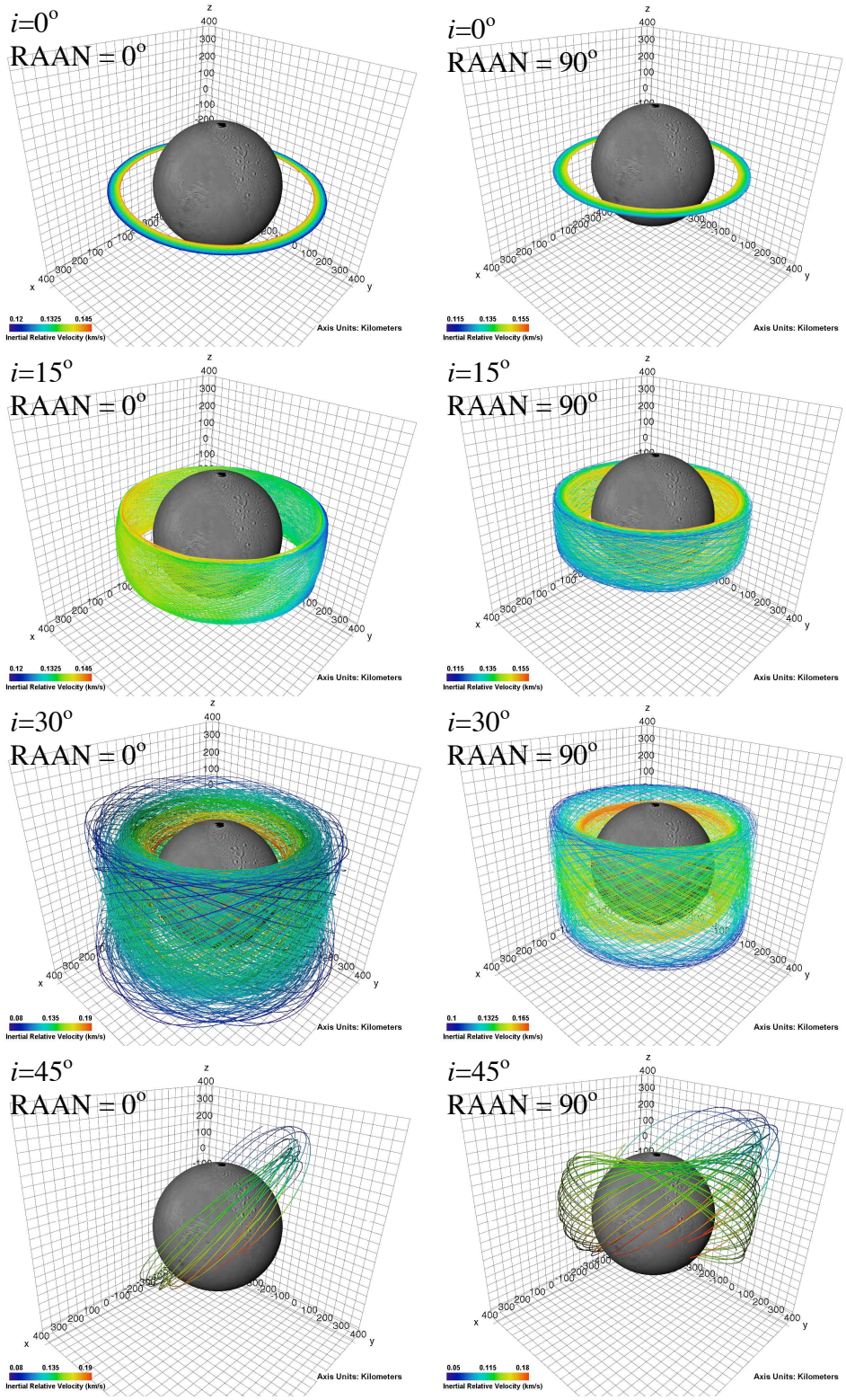

Figure 3.6 Circular Enceladus orbits of varying inclination, plotted in the Enceladus-centered non-rotating reference frame.

The maximum permissible orbital inclination observed in the Saturn-Enceladus CR3BP is not probed in great detail because solutions on the very border of transitions in dynamical behavior observed in the CR3BP are those solutions that are least likely to carryover to higher fidelity models with any predictive accuracy. Although significantly more conservative than other studies that attempt to truly maximize orbital inclination, the inclination limit of 30^{o} – the maximum value in this analysis that did not result in an Enceladus impact in less than six days – remains in agreement with other published results [4, 41]. The Enceladus Flagship Mission Concept Study [4] concluded that nearly-circular 200 km altitude orbits with inclinations above 45 degrees, but otherwise randomly selected initial conditions, generally result in an Enceladus collision when propagated in a full ephemeris system. Russell et al. [41] conclude, from a different and slightly more complex variation on the circular restricted three-body model, that 100 km altitude orbits with inclinations below 42 degrees avoid an Enceladus impact because the eccentricity oscillations resulting from perturbing influences remain sufficiently small. A thorough examination the Saturn-Enceladus system has only recently been undertaken by the scientific community due to the recent nature of the discoveries of the Cassini spacecraft at Saturn [3]. However, there has been a great deal of research focused on sending a spacecraft to Jupiter's moon Europa [42-46]. Dynamically, the Europa-Jupiter system has many similarities to the Saturn-Enceladus system. Thus, results from analysis in the Jovian system is relevant to the Enceladus mission design problem as well. Again, the conclusions from this investigation regarding permissible ranges of orbit inclinations around Enceladus are in general agreement with previously published results for the Jupiter-Europa system[42].

One of the primary purposes of undertaking simulations involving these Enceladus orbits is the determination of orbit types and orbital velocities, relative to Enceladus. These Enceladus orbiting states are the final target condition in a Saturn spacecraft tour that culminates in an Enceladus orbit insertion maneuver. From the previously generated circular orbits, it is demonstrated that for the types of orbits that succeed in avoiding an Enceladus collision for 100 days, the mean velocity of the spacecraft relative to

Enceladus is 136.72 m/s. This result is compared to the velocity corresponding to a circular orbit around Enceladus, that is,

$$v_c = \sqrt{\frac{Gm_E}{r}}, \tag{3.1}$$

where v_c is the velocity of a circular orbit of radius, r, the gravitational constant is expressed as G, and m_E is the mass of Enceladus. For the previously simulated circular orbits, the conic value of the circular velocity at a distance 406 km from Enceladus center (150 km altitude) is equal to $v_c = 133.26\,\text{m/s}$. The conic value and the value from the CR3BP simulations differ by only ~3 m/s. Define the baseline Enceladus orbital velocity as 136.72 m/s. For comparison, the Enceladus escape velocity is defined as the instantaneous tangential velocity required to depart on a parabolic trajectory from some fixed distance relative to the center of Enceladus. For bodies without significant atmospheres, like Enceladus, the escape velocity, v_{Esc}, is typically calculated as,

$$v_{Esc} = \sqrt{\frac{2Gm_E}{r_{mean}}}, \tag{3.2}$$

where r_{mean} corresponds to the mean radius of the body in question. Given the most recent available measurement of Enceladus' mean radius, i.e., $r_{mean} = 256.3\,\text{km}$, the Enceladus escape velocity is calculated as $v_{Esc} = 237.19\,\text{m/s}$. A spacecraft located 406 km from Enceladus' center, like the orbits from Figure 3.6, requires a speed equal to 188.38 m/s to escape Enceladus orbit. As such, it is possible to insert into an Enceladus orbit for as little as 52.65 m/s, and an Enceladus lander could theoretically arrive from outside the Enceladus system and reduce its velocity relative to the center of Enceladus to zero at the surface of the moon for as little as 237.17 m/s. Of course, both of these values rely on conic approximations. As such, these values for an Enceladus orbit insertion maneuver and landing are regarded as extreme lower bounds for the trajectory design of a spacecraft.

A more significant result from the examination of orbits around Enceladus and its Lagrange points is related to the orbit sensitivity. From an initial orbit with some visibility of Enceladus' poles, a spacecraft, under the influence of only the natural dynamics of the Saturn-Enceladus system, tends to either depart the vicinity of Enceladus or impact the moon following some brief period of time. The simulations of nearly-circular Encaladus orbits demonstrate that orbiting Enceladus is a challenging prospect. However, as an alternative to entering orbit relative to Enceladus, orbits exist around Saturn that, if properly selected, allow for frequent periodic flybys of Enceladus. Thus, it is possible to accomplish many of the science objectives of an Enceladus mission while avoiding the risk associated with the sensitivity of Enceladus orbits.

3.2.4 Orbital vs. Non-Orbital Enceladus Mission Design

As the previous results demonstrate, it is not trivial to determine an orbit around Enceladus that, while uncontrolled, accomplishes boththe science objectives of an Enceladus orbiter, and still avoid straying substantially from the desired orbit during an arbitrarily selected duration of time. However, some other orbit around Saturn might exist that still allows a spacecraft to accomplish many of the science objectives laid out for an Enceladus mission, while avoiding the problems associated with actually entering Enceladus orbit.

The most straightforward way of accomplishing many of the science objectives described in the Enceladus Mission Concept Study [4] is through a low-altitude orbit of Enceladus. An Enceladus orbit offers two advantages over possible trajectories of a spacecraft that is not in orbit around the moon: first, an orbiter will maintain close proximity to the moon for a long duration of time, and second, a spacecraft in orbit around Enceladus tends to move more slowly relative to the moon than a spacecraft approaching from beyond the Enceladus sphere of influence. Therefore, the goal in designing an orbit around Saturn, that periodically flies by Enceladus, is to incorporate the advantageous qualities of an Enceladus orbit to the maximum extent possible without entering orbit around Enceladus. Thus, to accomplish science objectives, the most

desirable flyby trajectory near Enceladus is a trajectory that minimizes the distance to the moon at closest approach while simultaneously minimizing the velocity of the spacecraft relative to the moon. Other than orbits around Enceladus, orbits around Saturn that frequently encounter Enceladus might also offer additional options and flexibility. To this end, one specific dynamical phenomenon with potential relevance is orbital resonance.

4. MEAN MOTION ORBITAL RESONANCE WITH ENCELADUS

4.1 Orbital Resonance in the Saturnian System

Orbital resonance is not merely a mission design tool, but rather it is a naturally occurring dynamical process throughout the solar system, and there are actually many examples of resonance just within the Saturnian system. Outside the environs of Saturn and its moons, well known examples of orbital resonance include the 2:3 resonance between Pluto and Neptune as well as the 1:2:4 Laplace resonance between three of Jupiter's moons: Ganymede, Europa, and Io [30]. However, the Saturnian system is perhaps an even more impressive natural laboratory of orbital resonance. Many of Saturn's larger inner moons exist in some naturally-occurring mean motion orbital resonance. For example, Hyperion moves in a 3:4 orbital resonance with Saturn's most massive moon, Titan, and there is a natural 2:1 resonance between two pairs of moons; Mimas and Tethys, as well as Enceladus and Dione [6]. Some of the ring gaps and other structures within the main rings of Saturn also result from resonant orbital interactions with various Saturnian ring moons, including Pan, Prometheus, and Pandora. The relationship between the Lagrange points of the restricted three-body problem and orbital resonance is also notable. The Lagrange equilibrium points are stationary relative to the rotating reference frame in the CR3BP and, thus, these points complete one orbit around the three-body problem barycenter in exactly the same amount of time as the two primaries. As such, the Lagrange points display a 1:1 orbital resonance with the primaries of the restricted three-body problem. Thus, the Trojan moons – Helene and

Polydeuces at the Saturn-Dione L_4 and L_5 points as well as Telesto and Calypso at the Saturn-Tethys L_4 and L_5 points – are additional examples of moons displaying a naturally occurring variety of orbital resonance with Saturn's larger satellites [39].

In interplanetary mission design, the value of orbital resonance is also widely recognized. For example, in designing orbital science tours (e.g., in the Jovian or Saturnian system), it is desirable to fly past several moons, and a particular flyby of a single moon is often designed specifically such that the spacecraft orbit following the flyby is in some orbital resonance with the flyby moon. Entering orbital resonance is one method of ensuring that the spacecraft will encounter the same moon again after both have completed some integer number of orbits about the large primary. This use of orbital resonance was exploited in the design of the trajectories for both the Galileo and Cassini spacecraft to Jupiter and Saturn, respectively [32, 47]. Orbital resonance is also an important component for many proposed orbital tours and cycler trajectories [43, 46-50].

4.2 Use of Resonant Orbits for Periodic Enceladus Encounters

A strategy to target resonant orbits in the CR3BP was introduced in Chapter 2. The direct application of the technique to the Saturn-Enceladus CR3BP produces orbits around Saturn that periodically fly close to Enceladus. The Saturn-Enceladus restricted three-body problem is a particularly interesting system since the diminutive size of Enceladus is insufficient to be practically used to intentionally reshape the orbit of a hypothetical spacecraft. However, the gravity field of the tiny moon still interferes with the direct use of trajectories designed in the conic model when those trajectories pass close to the moon.

Consider the 3:4 resonant orbit from the conic model in the Saturn-Enceladus system that appears in Figure 2.7. The perikrone passage in the immediate vicinity of Enceladus is used as a starting point for the targeting algorithm with the goal to deliver a closed resonant orbit in the restricted three-body problem. The result of the differential

corrections process appears in Figure 4.1, where the green trajectory corresponds to the uncorrected initial condition supplied to the targeter and derived from the corresponding two-body resonant orbit; the red trajectory is the final corrected resonant orbit in the three-body problem. The differential corrections process for this resonant orbit required

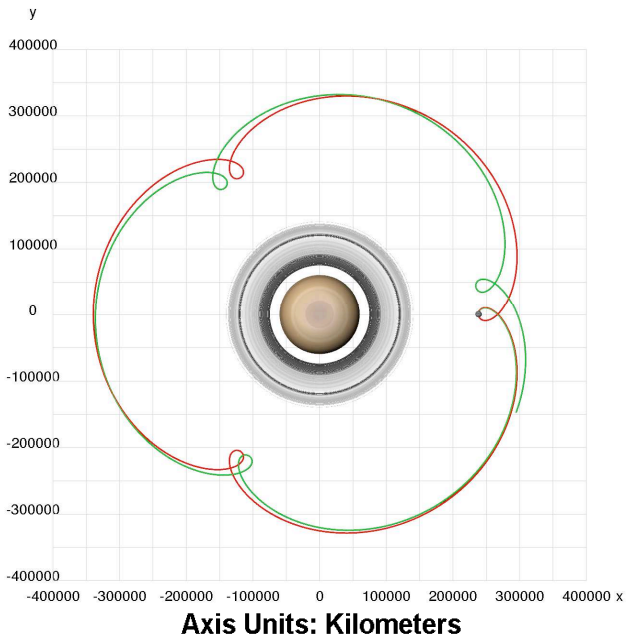

Figure 4.1 Comparison of an uncorrected (green) and corrected (red) 3:4 resonant orbit in the Saturn-Enceladus CR3BP.

five iterations of the algorithm to converge on an orbit that is periodic within a tolerance of 10^{-12}. The initial conditions of both the two-body resonant orbit and the corrected orbit in the restricted three-body problem are shown in Table 4.1. A spacecraft in a 3:4 resonance with Enceladus in the two-body model returns to precisely the same position relative to Enceladus after the moon has completed four orbits around Saturn; in the restricted three-body problem, Enceladus does not complete an exact integer number of orbits when the realignment of the bodies occurs. For the resonant orbit from Figure 4.1, it is clear from Table 4.1 that Enceladus is 0.4% of one orbital period shy of completing its fourth circular orbit around Saturn. The net effect of Enceladus' gravity on the resonant orbit, is a velocity discrepancy in the initial spacecraft state of just 22.2 m/s.

Table 4.1 Non-zero initial condition elements of a two-body and corrected three-body 3:4 resonant orbit.

	x (km)	$\dot{y}$ (km/s)	Period (days)	# of Complete Enceladus Orbits
2-Body Resonant Orbit	238115.483125	13.684378	5.498244	4.000000
3-Body Resonant Orbit	238115.483125	13.706601	5.493279	3.996388

In fact, the influence of Enceladus is so small that when the two-body resonant orbit and corrected three-body orbit are plotted together (Figure 4.2), the two curves are nearly indistinguishable to the naked-eye without refocusing the plot on the loop corresponding to the perikrone passage of the 3:4 resonant orbit in the immediate vicinity of Enceladus. For the resonant orbit in Figure 4.2, the perikrone passage occurs at the same moment as

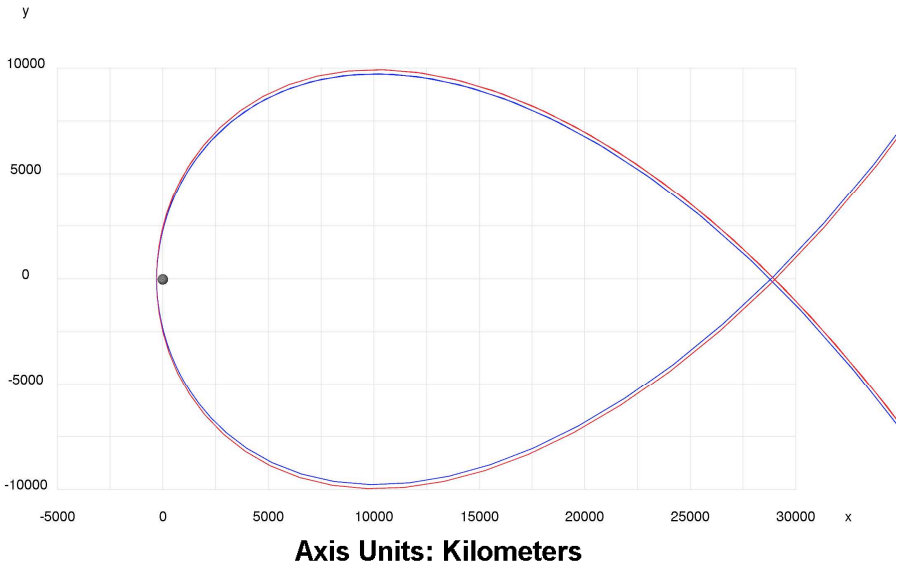

Figure 4.2 Comparison of the same 3:4 resonant orbit calculated in the two-body (red) and three-body (blue) models in the vicinity of Enceladus.

the closest approach to Enceladus. In Figure 4.2, the red trajectory is a periodic 3:4 resonant orbit in the two-body model, where Enceladus gravity is neglected; the blue path in Figure 4.2 is the corresponding periodic orbit in the CR3BP, where Enceladus influence is incorporated. The 22.2 m/s velocity discrepancy between the two-body and three-body resonant orbits is remarkably small, yet considering that the trajectories pass just 40 km above the surface of Enceladus at closest approach, very little additional

reshaping of the orbit is expected to result from Enceladus flybys, without the spacecraft colliding with the moon. However, while drastic reshaping of an orbit through the use of Enceladus flybys seems unlikely, the small perturbing influence of the moon continues to affect all corrected periodic orbits in the CR3BP, though that effect will admittedly diminish as the distance of closest approach of a spacecraft relative to Enceladus continues to grow. Using initial conditions from a two-body resonant orbit becomes an increasingly accurate approximation, as the minimum distance to Enceladus increases. However, a differential corrections scheme to refine the orbit is always required to converge to periodicity in the CR3BP to within some reasonable tolerance.

To demonstrate the point that Enceladus does reshape orbits that pass just above the moon's surface, several additional members of the family of planar 3:4 resonant orbits appear in Figure 4.3 and all are periodic in the Saturn-Enceladus three-body problem.

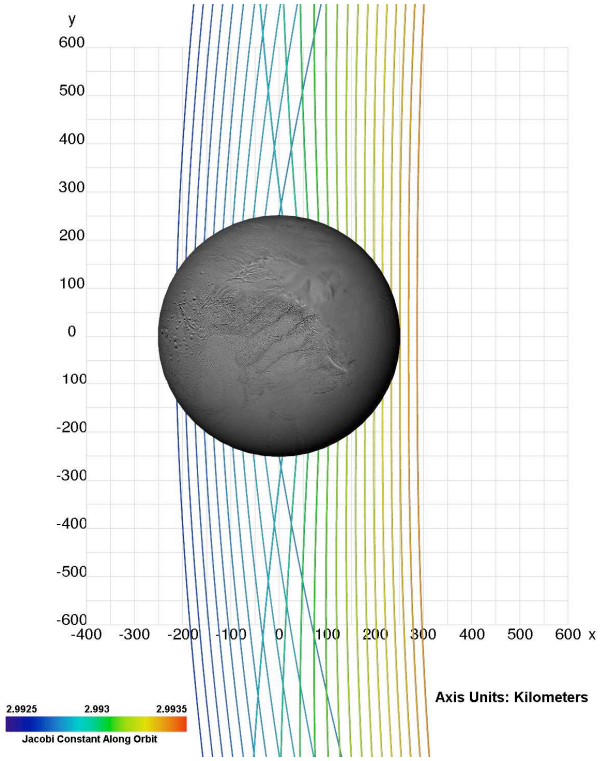

Figure 4.3 A demonstration of the gravitational perturbation of several planar 3:4 resonant orbits that pass near the Enceladus point-mass in the CR3BP.

The trajectories visible in Figure 4.3 are all examples of 3:4 resonant orbits that appear structurally similar to the periodic orbit in Figures 4.1 and 4.2. However, in Figure 4.3 only the portion of each 3:4 resonant orbit that passes near the immediate vicinity of Enceladus is plotted. To magnify the perturbing influence that Enceladus exerts on trajectories that pass near the gravitational singularity at the moon's center in the CR3BP, the trajectories in Figure 4.3 are allowed to pass below the surface of the moon. These trajectories demonstrate that only subtle perturbations of the resonant orbits are anticipated as the distance of the closest approach to the moon grows beyond even the moon's own radius.

4.3 Families of Resonant Orbits in the Saturn-Enceladus CR3BP

To determine the types of resonant orbits around Saturn that are most applicable to the problem of designing periodic Enceladus flyby trajectories, it is first necessary to examine the size and structure of many different families of resonant orbits. There are an infinite number of resonant orbits in the CR3BP, and, as such, the families in this investigation do not necessarily constitute a global search of the design space. Instead, many of the lower-numbered resonances (i.e., 1:2, 2:3, 1:3, 3:4, etc.) are examined as a starting point to gain a qualitative understanding of resonant orbits in the vicinity of Enceladus. Resonances involving small integer ratios are preferred over higher-numbered resonances (e.g., a 57:59 resonance) because the frequency of Enceladus encounters is higher for lower-numbered resonances. For example, a spacecraft in a 2:3 resonance with Enceladus encounters the moon twice in less than five days, while a spacecraft in a 57:59 resonance with Enceladus only completes its full resonant period after several months have passed.

Even among the small integer resonance ratios, several resonances are not considered for practical reasons. Resonances that form un-reduced rational fractions are ignored in favor of the reduced fraction representation of the same resonance. For example, the family of 1:2 resonant orbits are considered, while the 2:4 and 4:8 families are ignored. However, it is possible that there are families of 4:8 resonant orbits that are not identical

to the family of 1:2 resonant orbits, but there are no examples of orbits of this type included in this analysis.

4.3.1 Families of 1:1 Resonant Orbits in the Saturn-Enceladus System

Perhaps the simplest orbital resonance between a spacecraft and Enceladus is demonstrated by the families of 1:1 resonant orbits. Several orbits from this resonance appear in Figure 3.2. However, while this resonant ratio may be the simplest to understand intuitively in the CR3BP – a spacecraft completes approximately one orbit around Saturn in the time it takes Enceladus to do the same – the families of possible orbits that share this resonance with Enceladus are actually quite varied. In fact, there are several families of 1:1 resonant orbits in the CR3BP. Multiple members of four families of 1:1 resonant orbits are plotted in Figure 4.4.

Recall the previous discussion of planar periodic Lagrange point orbits in the CR3BP; specifically, the L_1 and L_2 families of Lyapunov orbits in the Saturn-Enceladus system that appear in Figure 3.1. In addition to the L_1 and L_2 Lyapunov orbits, there are also planar periodic orbits around the L_3, L_4, and L_5 Lagrange points, though the name "Lyapunov" is reserved for orbits around the three collinear Lagrange points. A subset of the L_3 Lyapunov orbit family is plotted in Figure 4.4; planar members of families in the vicinity of the equilateral points also appear in the figure. There are actually an infinite number of orbits in each of the four families plotted in Figure 4.4. The orbits in this figure are constructed numerically through a continuation process from small orbits in the immediate vicinity of the Lagrange points, in the case of the L_3, L_4, and L_5 planar orbits, and small orbits in the vicinity of Enceladus in the case of the orbits that encircle that moon. Mathematically, all of the families extend far beyond the range of orbital sizes in Figure 4.4. However, it is generally desirable to remain outside of Saturn's rings, so only orbits with perikrone above Saturn's main rings are plotted. Traditionally, the L_3, L_4,

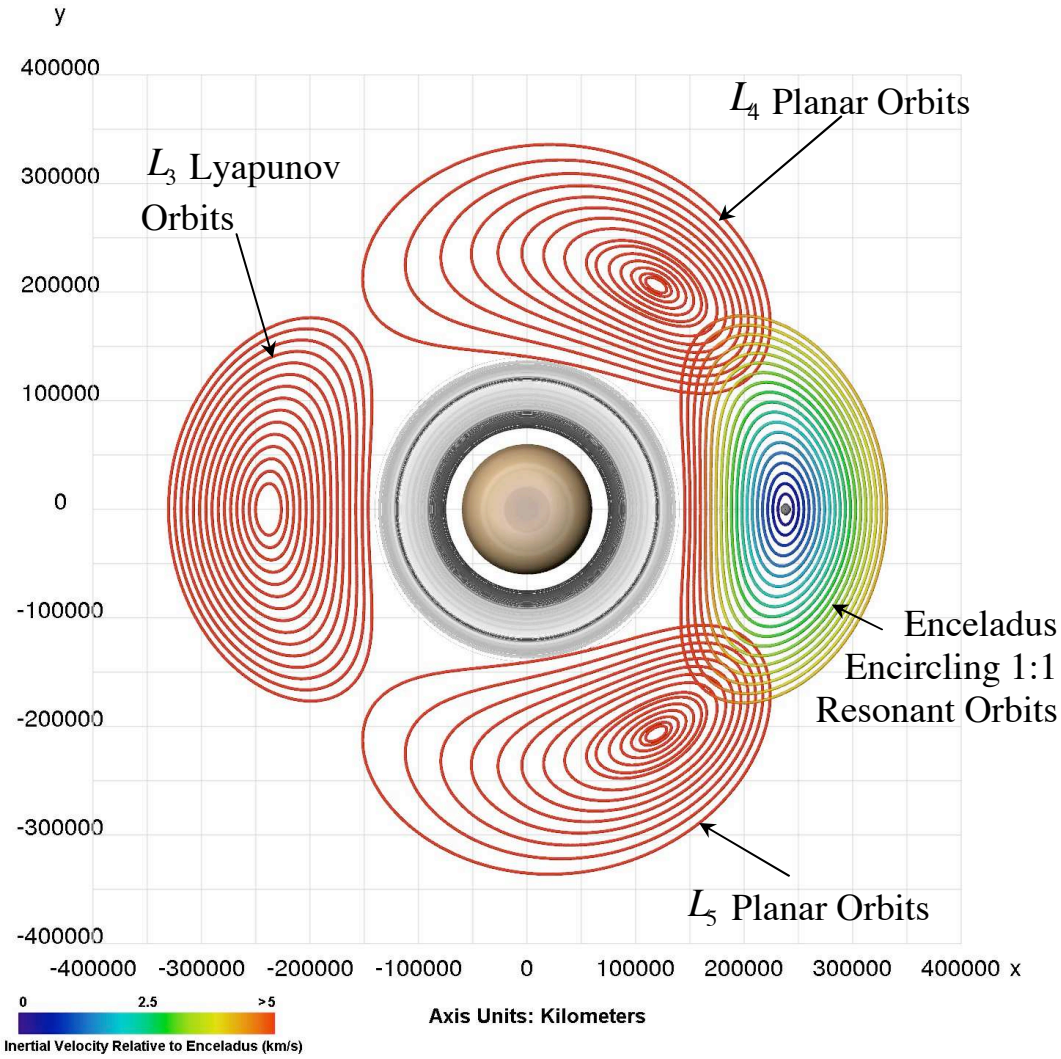

Figure 4.4 Four families of 1:1 (spacecraft: Enceladus) resonant orbits in the Saturn-Enceladus CR3BP rotating frame.

and L_5 planar orbits are not labeled 1:1 resonant orbits but, in fact, these orbits are members of orbit families that satisfy the definition of orbital resonance in the CR3BP. This definition requires that a spacecraft in a $p:q$ resonant orbit completes p revolutions around the CR3BP barycenter in *approximately* the time that the second primary, Enceladus, completes q orbits. In addition to the near rational ratio of the orbital periods of a spacecraft and Enceladus, the definition of resonance requires that

resonant orbits are closed and periodic in the rotating reference frame. As noted in Chapter 2, all five of the Lagrange points associated with any restricted three-body system are in a precise 1:1 resonance with the system primaries. In addition to the resonance of the Lagrange points, the planar libration point orbits in the vicinity of L_3, L_4, and L_5 also form closed orbits in the CR3BP with orbital periods approximately equal to the period of the primaries in the three-body problem. Table 4.2 includes the initial conditions for the smallest and largest members of each family of 1:1 resonant orbits plotted in Figure 4.4. The data in Table 4.2 indicates that the resonance ratio between the orbital period of the L_3, L_4, and L_5 planar orbits and the orbit of Enceladus is preserved to the sixth decimal place, despite the perturbing influence of Enceladus. However, while the three families of planar Lagrange point orbits maintain the close 1:1 resonant ratio with Enceladus across the entire range of orbits calculated for this investigation, the same cannot be said for the family of orbits that encircle the moon.

Table 4.2 Initial conditions of the largest and smallest orbits in four families of 1:1 resonant orbits.

Orbit Type	$\dot{x}$ (km/s)	y (km)	$\dot{x}$ (km/s)	$\dot{y}$ (km/s)	Period (days)	# of Complete Enceladus Orbits
Small L_3 Lyapunov	-250334.175	0	0	1.246333	1.374560894	0.999999929
Large L_3 Lyapunov	-349514.191	0	0	10.878614	1.374560924	0.999999951
Small L_4 Planar	165477.1362	187914.4841	0.070612	-1.939917	1.374561980	1.000000719
Large L_4 Planar	237001.1862	188567.9638	0.894063	-9.555970	1.374561524	1.000000387
Small L_5 Planar	165477.1362	-187914.484	-0.070612	-1.939917	1.374561980	1.000000719
Large L_5 Planar	237001.1862	-188567.963	-0.894063	-9.555970	1.374561524	1.000000387
Small Planar Enceladus Orbit	236029.365	0	0	0.264624	1.218597735	0.88653595
Large Planar Enceladus Orbit	145432.235	0	0	11.346182	1.374558572	0.999998239

In Table 4.2, temporarily focus on the planar Enceladus orbits. The results demonstrate that for the family of 1:1 resonant orbits that revolve around Enceladus in Figure 4.4, the larger orbits possess a period that matches Enceladus orbital period to the fifth significant

digit, but the precision of the resonance is degraded as the orbits decrease in size and more closely approach Enceladus.

The families of resonant orbits around the L_3, L_4, and L_5 Lagrange points in Figure 4.4 demonstrate that for any $p:q$ resonance, there are generally multiple families of periodic orbits that exist. However, since orbits that closely approach Enceladus are desired, the focus of this analysis is on resonant families with characteristics similar to the Enceladus-centered orbits in Figure 4.4, that is, families of orbits that possess symmetry across the *x*-axis and closely approach the moon.

4.3.2 Families of Exterior Resonant Orbits in the Saturn-Enceladus CR3BP

To expand the understanding of the structure of resonant orbits in the Saturn-Enceladus system, several additional families are computed. Multiple families of resonant orbits in the Saturn-Enceladus rotating reference frame appear in Figures 4.5 and 4.6. The families of orbits in both figures are examples of exterior resonant orbits; the resonant ratio of these orbits is $p:q$, such that $p < q$. These orbits are termed "exterior" resonant orbits because each orbit is defined in terms of an instantaneous semi-major axis that is greater than the semi-major axis of Enceladus' orbit around Saturn. Thus, more than 50% of the time the spacecraft moves along its orbital path around Saturn at a distance that is beyond the orbit of Enceladus. The size of Enceladus has been exaggerated by a factor of 20 in Figures 4.5 and 4.6 to aid in visibility, and the moon appears as a stationary sphere at a coordinate of $x \approx 238{,}000$ km.

Velocity information along the trajectories in Figures 4.5 and 4.6 is indicated by the color gradient; colors on the red end of the spectrum correspond to higher velocities relative to Enceladus and the blue end of the spectrum represents lower velocities relative to the moon. Again, lower velocities relative to Enceladus are preferred for accomplishing science objectives during the closest approach of the spacecraft to the moon. To compute the orbits in the families plotted in Figures 4.5 and 4.6, a differential

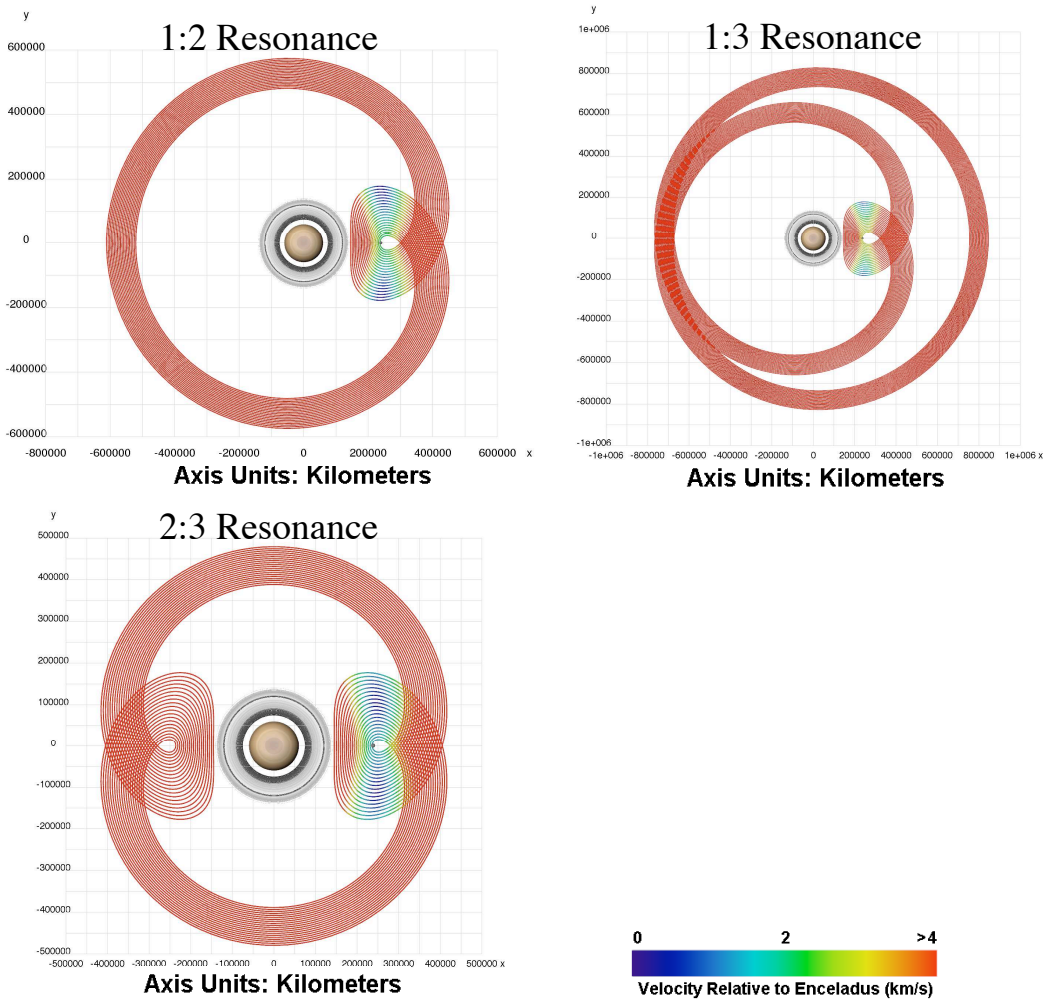

Figure 4.5 Exterior resonant orbit families plotted in the rotating frame of the Saturn-Enceladus CR3BP.

corrections algorithm is employed. Perpendicular crossings of the rotating *x*-axis between Saturn and Enceladus are targeted to achieve orbital periodicity. The initial conditions to generate the orbits in each family of orbits span a range along the *x*-axis from ~140,000 km relative to Saturn's center, to a distance equal to ~240,000 km. Saturn's main rings extend to a distance of ~175,000 km relative to the center of the planet. Therefore, the orbits in Figures 4.5 and 4.6 that intersect the rings are not generally practical. The outer edge of the F-ring terminates at a distance of approximately 140,000 km from Saturn, so this distance is used as a lower bound on the minimum allowable perikrone distance allowable for each resonant orbit.

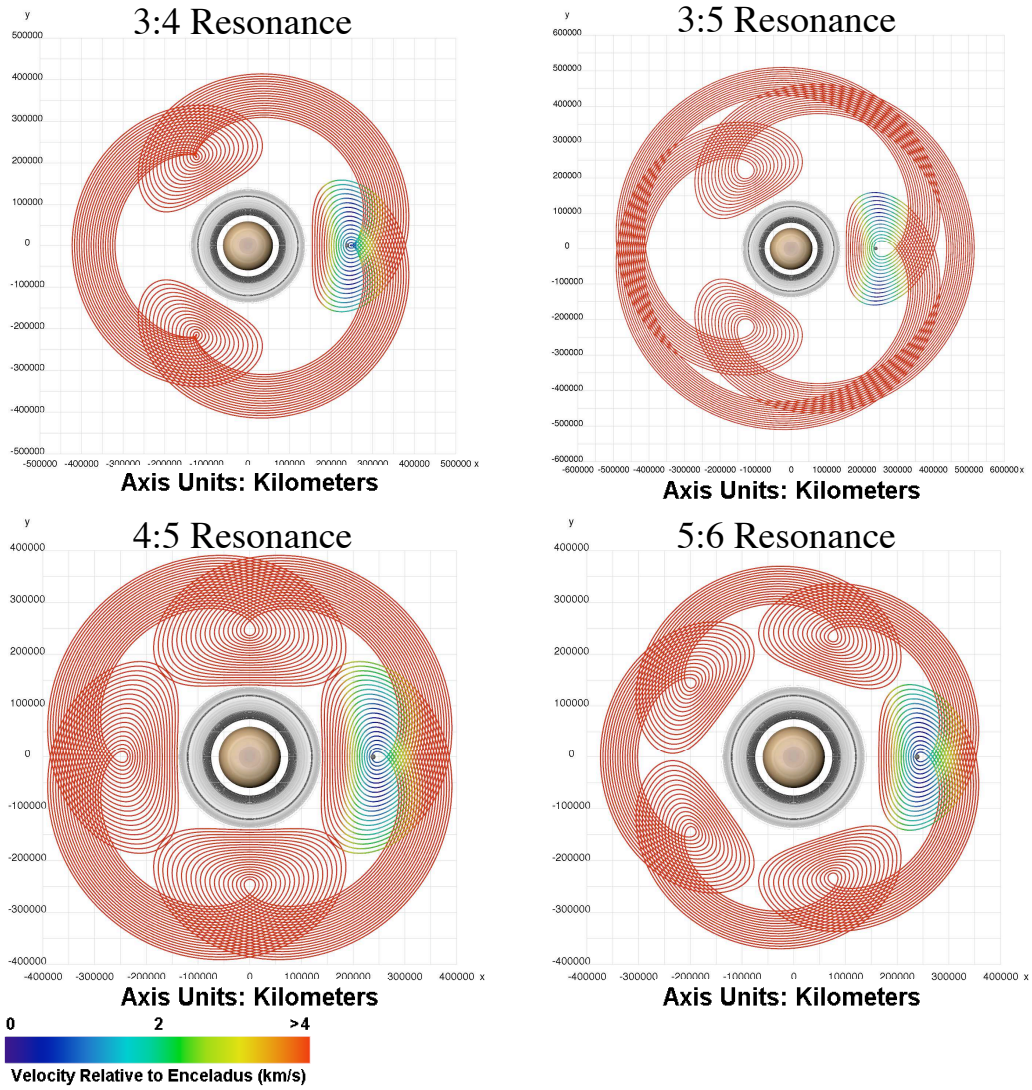

Figure 4.6 Additional exterior resonant orbit families plotted in the rotating frame of the Saturn-Enceladus CR3BP.

Since Enceladus observability is the primary motivation in generating these orbits, only those orbits with perikrone closer to Saturn than Enceladus' orbit are examined in detail, that is, orbits that pass between Saturn and Enceladus during their closest approach to the planet. In general, exterior resonant orbits with periapsis above the orbit of Enceladus do exist in each one of the exterior resonant families in Figures 4.5 and 4.6, but these orbits are of little utility here. Note that each of the exterior resonant orbits in the figures includes a perpendicular x-axis crossing between Enceladus and Saturn. However, recall that there are complementary families for each resonance that cross the

positive x-axis perpendicularly beyond the distance of Enceladus. An example of each of these two types of families of resonant orbits is included in Figure 4.7. The left plot in Figure 4.7, represents the family of 3:4 resonant orbits from Figure 4.6; it includes a perikrone passage loop that encircles Enceladus. A complementary family of 3:4 resonant orbits appears in the right plot of Figure 4.7; this family is less useful for Enceladus science since the path never approaches the moon.

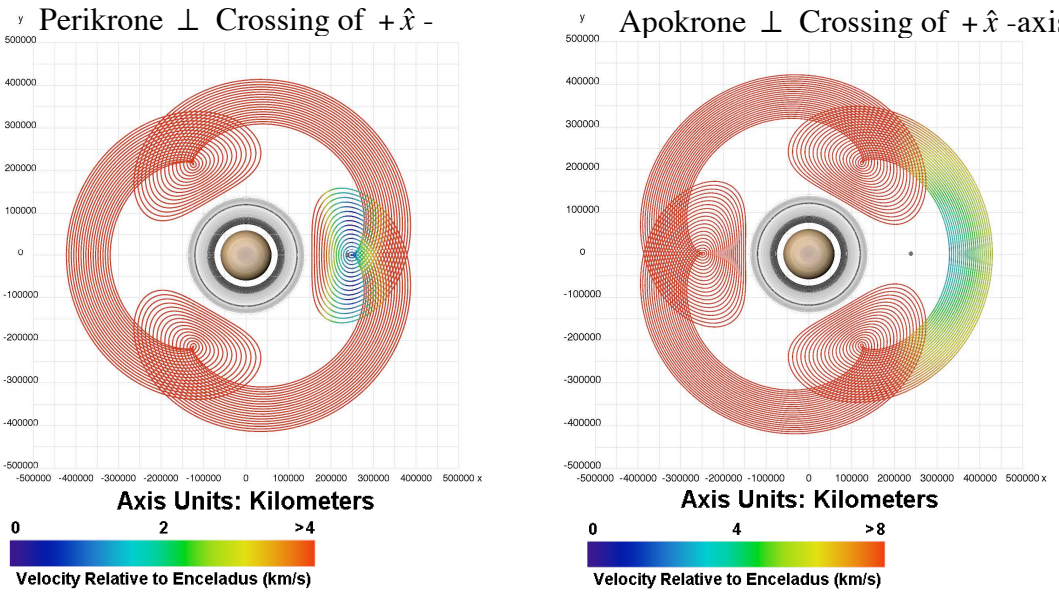

Figure 4.7 Comparison of two distinct families of 3:4 resonant orbits in the Saturn-Enceladus rotating frame.

Further consideration of resonant orbits with higher $p:q$ ratios introduces closed and periodic resonant orbits in the CR3BP that accomplish multiple close flybys of Enceladus during one resonant period. One example that achieves two close Enceladus flybys during a single resonant period is accomplished via a 9:10 resonant orbit. In Figure 4.8, there are two views of several members from a 9:10 resonant family with a perikrone distance of approximately 152,000 km. However, unlike the resonant orbits from the previous figures, two close Enceladus encounters occur along the trajectories in Figure 4.8. These close encounters are approximately mid-way between the perikrone and apokrone distances of the orbit. In Figure 4.8, the orbits are plotted in the Saturn-Enceladus rotating frame.

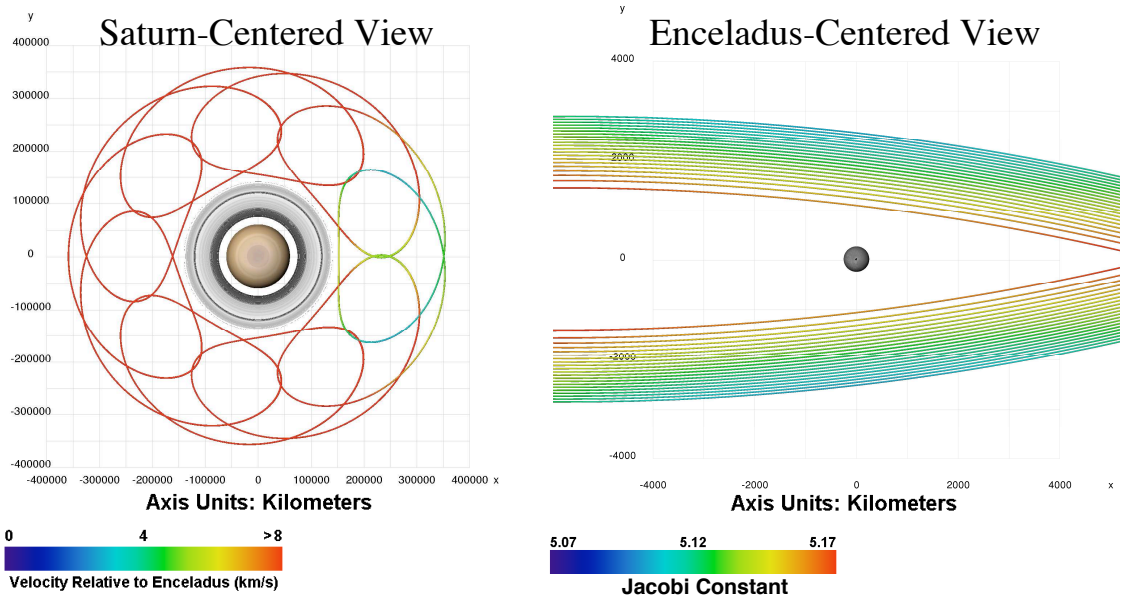

Figure 4.8 A family of 9:10 resonant orbits that allow for two Enceladus flybys during a single resonant period.

Clearly, one advantage of a resonant orbit similar to the 9:10 resonant orbits in Figure 4.8 is two close Enceladus encounters that are spaced relatively close in time, followed by a longer period of time devoid of any close flybys. A potentially significant drawback associated with such Enceladus flybys is a high velocity relative to Enceladus during each flyby: velocities on the order of 5 km/s. Velocities of this magnitude greatly exceed the relative velocities along one of the resonant orbit families that appear in Figures 4.5 and 4.6.

4.3.3 Families of Interior Resonant Orbits in the Saturn-Enceladus CR3BP

All previous families of resonant orbits are comprised of orbits that are examples of exterior resonance. In exterior resonance, the spacecraft moves on an orbit around Saturn with a longer orbital period than Enceladus' orbit; the spacecraft therefore completes fewer orbits around Saturn than the moon during each resonant cycle. For exterior resonant orbits, the resonance will be of the form $p:q$, such that $p < q$. However, there are also families of *interior* resonant orbits, those with a resonance of the form $p:q$,

such that $p > q$. An interior resonant orbit around Saturn possesses a semi-major axis that is smaller than the orbit of Enceladus. As such, the orbital period of an interior resonant orbit is also smaller than the orbital period of Enceladus, and a spacecraft on an interior resonant orbit completes more orbits around Saturn than the moon during each resonant period.

Several examples of interior resonant orbits in the Saturn-Enceladus CR3BP appear in Figure 4.9. Unlike the exterior resonant orbit families, a spacecraft on an interior resonant orbit from one of the families in Figure 4.9 spends the majority of its orbital period inside of the orbit of Enceladus. While the loops in the exterior resonant orbit families in Figure 4.5 and 4.6 correspond to times when the spacecraft passes *perikrone* in its orbit around Saturn, the loops visible in the interior resonant orbit families in Figure 4.9 correspond to *apokrone* passages.

Enceladus' orbit around Saturn is relatively close to Saturn's rings; it is just 1.7 times further from Saturn than the outer edge of Saturn's F-ring. Unfortunately, the proximity of Enceladus' orbit to Saturn's rings implies that there is only a narrow range available for interior resonant orbits to closely encounter the moon, while still maintaining a sufficiently large perikrone distance to avoid collision with Saturn's rings. Note that in the 3:2 family of resonant orbits from Figure 4.9, even the orbit with the apokrone loop nearest Enceladus fails to actually reach the of the orbit of Enceladus. The apokrone distance associated with the 3:2 resonant orbits in Figure 4.9 cannot be raised to more closely approach Enceladus without the trajectory passing through Saturn's rings during perikrone. Since interior resonant orbits are within the orbit of Enceladus, the velocities along these orbits are higher, relative to Saturn, that the velocity of Enceladus. Consequently, to exploit an interior resonant orbit, the spacecraft's orbital energy must be reduced to a level below that of Enceladus' orbit. If a spacecraft transfers down from an original orbit with apokrone near Titan, the required energy reduction to achieve interior resonance with Enceladus is greater than the reduction required to reach an exterior resonant orbit.

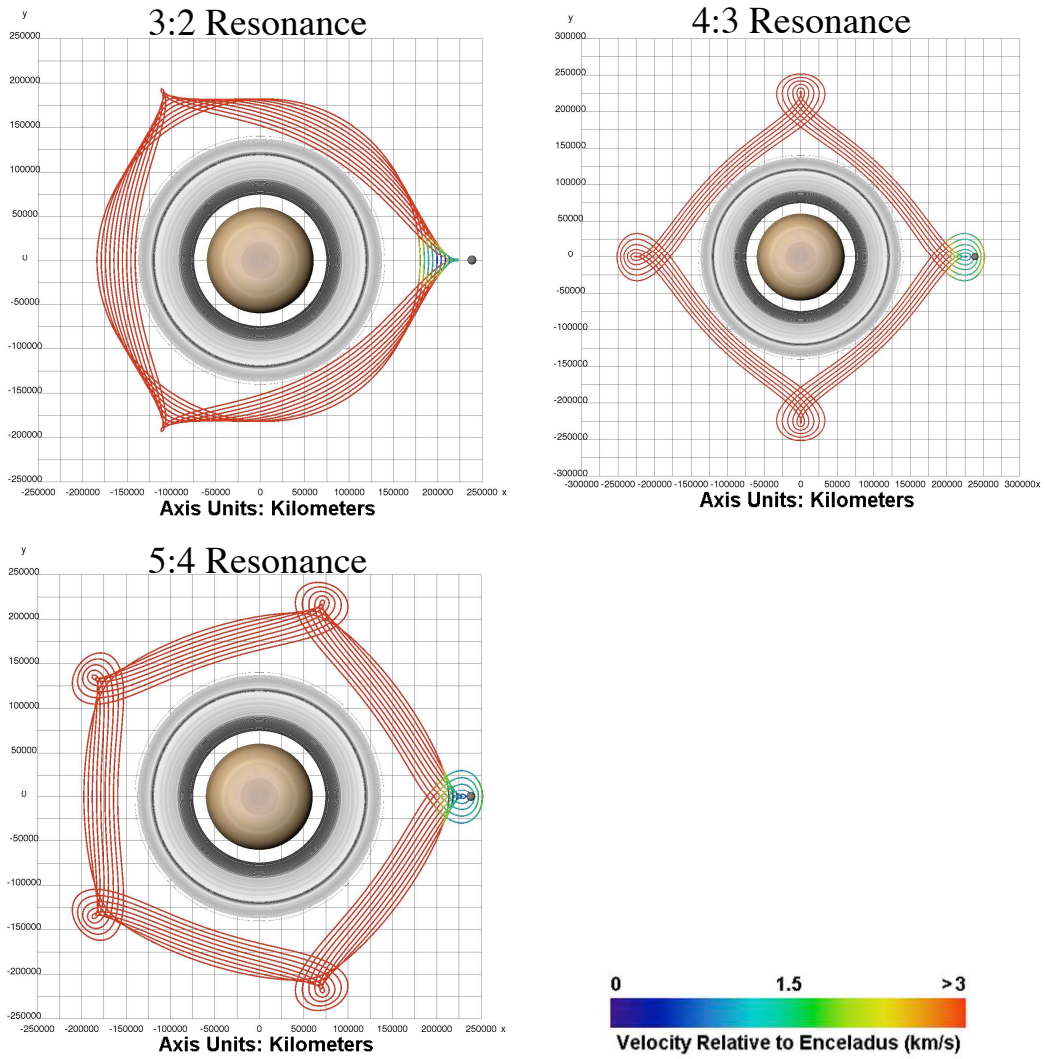

Figure 4.9 Interior resonant orbit families plotted in the rotating frame of the Saturn-Enceladus CR3BP.

In summary, the previous families of resonant orbits can be constructed using differential corrections and a continuation process. Ultimately, only a handful of orbits from any resonant family would support an Enceladus mission. Those resonant orbits with qualities that are desirable for mission design purposes can be isolated by examining each family of resonant orbits and identifying the orbits which have characteristics that meet the design criteria.

4.4 Trajectories in Resonance with Both Dione and Enceladus

In the previous analysis, families of resonant orbits are constructed in the Saturn-Enceladus CR3BP. Using the same methodology, it is also possible to identify resonant orbits in other restricted three-body systems; this includes systems with Saturn and some other Saturnian moon as the two primaries. Also, recall that Enceladus is in a natural 2:1 resonance with Saturn's moon Dione, and this result offers additional utility in the design of resonant orbits that frequently fly by Enceladus. If the resonance between Enceladus and Dione is exactly 2:1, then any resonant orbit computed in the Saturn-Enceladus CR3BP, one that is closed and periodic in the Saturn-Enceladus rotating frame, is also closed and periodic in the Saturn-Dione rotating reference frame. Thus, for any $p:q$ resonance between a spacecraft and Enceladus, the same trajectory possesses a $p:\frac{q}{2}$ resonance with Dione. The CR3BP model utilized to target resonant orbits still only includes the gravitational influence of a single Saturnian moon. However, it is possible to define an additional rotating reference frame that is not associated with any gravitational source. This additional rotating reference frame that facilitates orbit design for resonance with Dione is defined with a rotational period corresponding to the period of a massless satellite in circular motion around Saturn at a distance equal to that of Dione's semi-major axis.

The natural resonance between Enceladus and Dione introduces another option in the design of resonant trajectories for a spacecraft in the Saturnian system: resonant trajectories that periodically encounter both Enceladus and Dione. Such an orbit offers an opportunity for repeated flybys of both Enceladus and Dione. It is also possible to use Dione's gravitational influence to assist in maintaining a resonant orbit. Smaller maneuvers prior to a close Dione flyby yield a larger effect on the orbit of a spacecraft.

4.4.1 Trajectory Design in the Saturn-Dione CR3BP

For resonant orbits that fly by both Enceladus and Dione, the dynamical model must be modified. This analysis uses more than one dynamical model to simulate the trajectory of a spacecraft on a resonant orbit that periodically encounters both Enceladus and Dione. First, this analysis uses the CR3BP to model the Saturn-Dione system, with Enceladus modeled as a massless satellite. Recent measurements of the masses of both Dione and Enceladus indicate that Dione is approximately 10 times more massive than Enceladus (Table 4.3) [3, 39]. Although Enceladus is currently the primary body of interest scientifically, the inclusion of Dione's gravity field is of greater dynamical import. Therefore, the restricted three-body problem used to model the behavior of a spacecraft flying near both Dione and Enceladus, is initially the Saturn-Dione CR3BP.

Isolating a trajectory to fly by both Dione and Encladus is accomplished by first using differential corrections to determine families of resonant orbits in the Saturn-Dione system. Since the desired orbits pass near Enceladus as well as Dione, the focus is placed on the families of interior resonant orbits, that is, orbits that complete more revolutions around Saturn than Dione during each orbital period. Qualitatively, the families of resonant orbits in the Saturn-Dione system appear similar to the families from the Saturn-Enceladus system, plotted in Figures 4.4-4.9.

Once families of resonant orbits are constructed in the Saturn-Dione CR3BP, individual orbits are selected that exhibit desirable characteristics. In particular, a trajectory is sought that crosses the orbit of Enceladus near perikrone, thus minimizing the relative velocity between the two bodies, and the orbit also passes relatively near Dione at apokrone. In general, a resonant orbit that is periodic in the Saturn-Dione CR3BP and crosses Enceladus' orbit, does not encounter Enceladus due to timing issues.

Recall, Enceladus' gravity field is not incorporated in the Saturn-Dione model, so the initial position of Enceladus can potentially be arbitrarily selected so that the moon lies precisely at the intersection between Enceladus' orbit and the spacecraft's orbit at the moment that the spacecraft reaches the intersection point. However, Enceladus is always assumed to be aligned with Dione at the initial time. Thus, the timing for the Enceladus

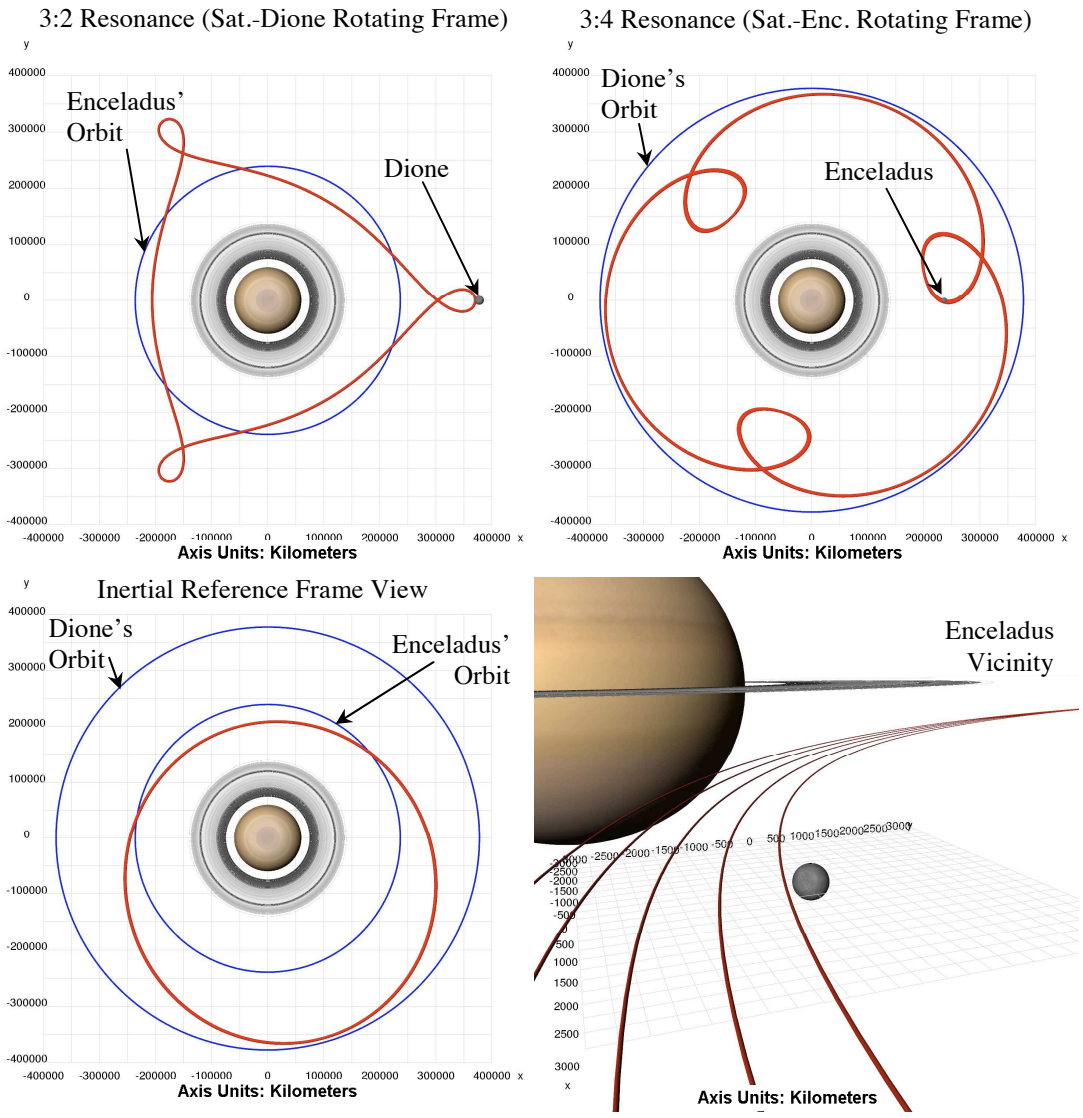

Figure 4.10 A 3:2 resonant orbit from the Saturn-Dione CR3BP; viewed also in the Saturn-Enceladus rotating frame, the inertial reference frame.

flyby is controlled by selecting the position and velocity of the spacecraft at the initial time. Once some resonant orbit is determined in the Saturn-Dione CR3BP, a complete time-history of the spacecraft motion along the resonant orbit is available. With full knowledge of the state of the spacecraft at each instant of time along the path, it is possible to target an Enceladus flyby by noting the time-of-flight from the initial state on the *x*-axis to the crossing of Enceladus' orbit. Thus, the initial position of the spacecraft is offset along the orbit such that the spacecraft crosses Enceladus' orbit at the same

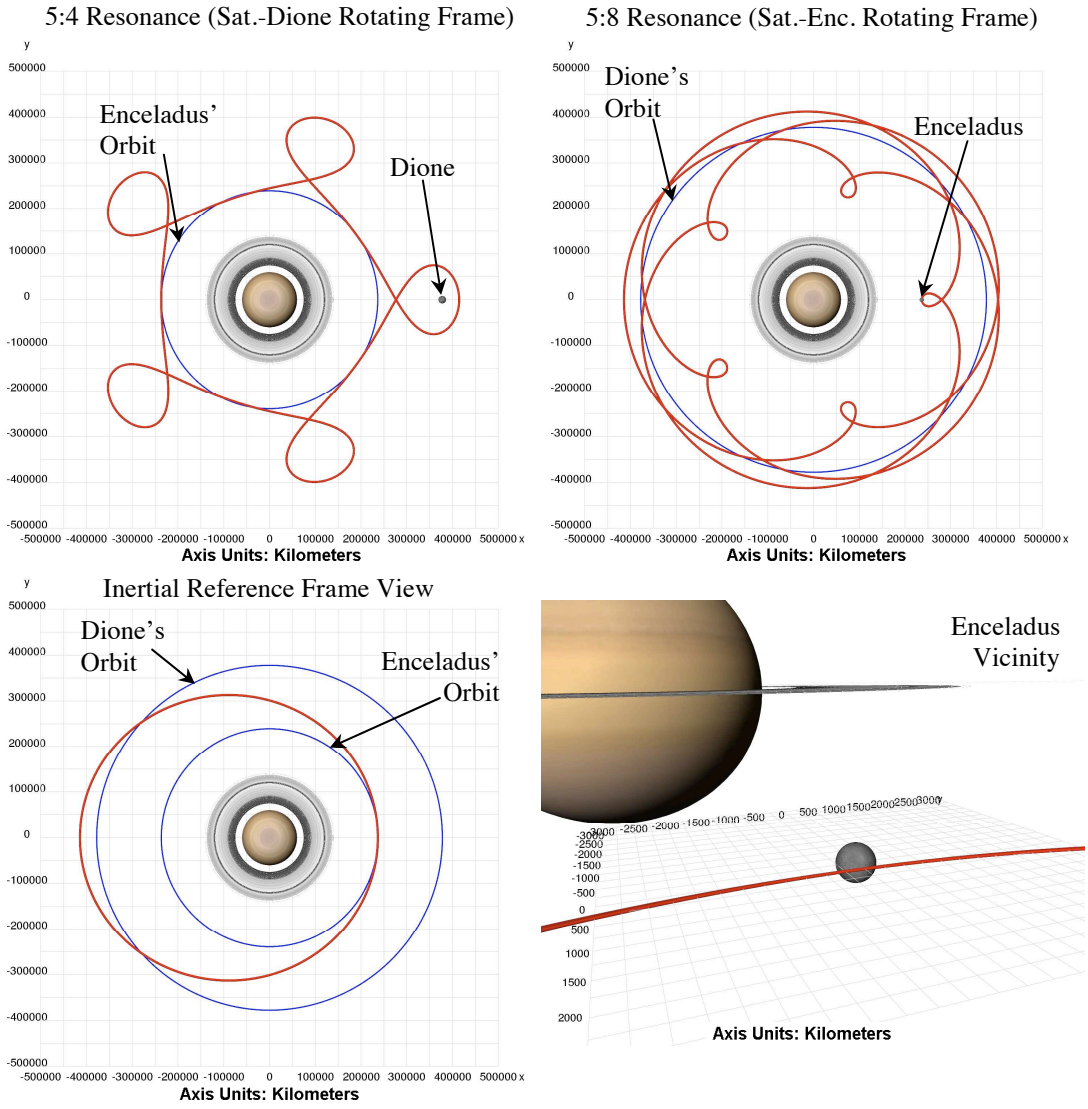

Figure 4.11 A 5:4 resonant orbit from the Saturn-Dione CR3BP viewed also in the Saturn-Enceladus rotating frame, the inertial reference frame.

moment that the moon reaches the intersection point.

As examples, orbits from three different resonant families are isolated and then further refined to ensure that flybys of both Dione and Enceladus occur. These examples originate from the 3:2, 5:4, and 4:3 resonant orbit families in the Saturn-Dione CR3BP, and the final trajectories are plotted in Figures 4.10-4.12. For each of the resonances plotted in Figures 4.10-4.12, four views of the trajectory appear; these include the Saturn-Dione rotating frame, the Saturn-Enceladus rotating frame, the inertial frame view, and

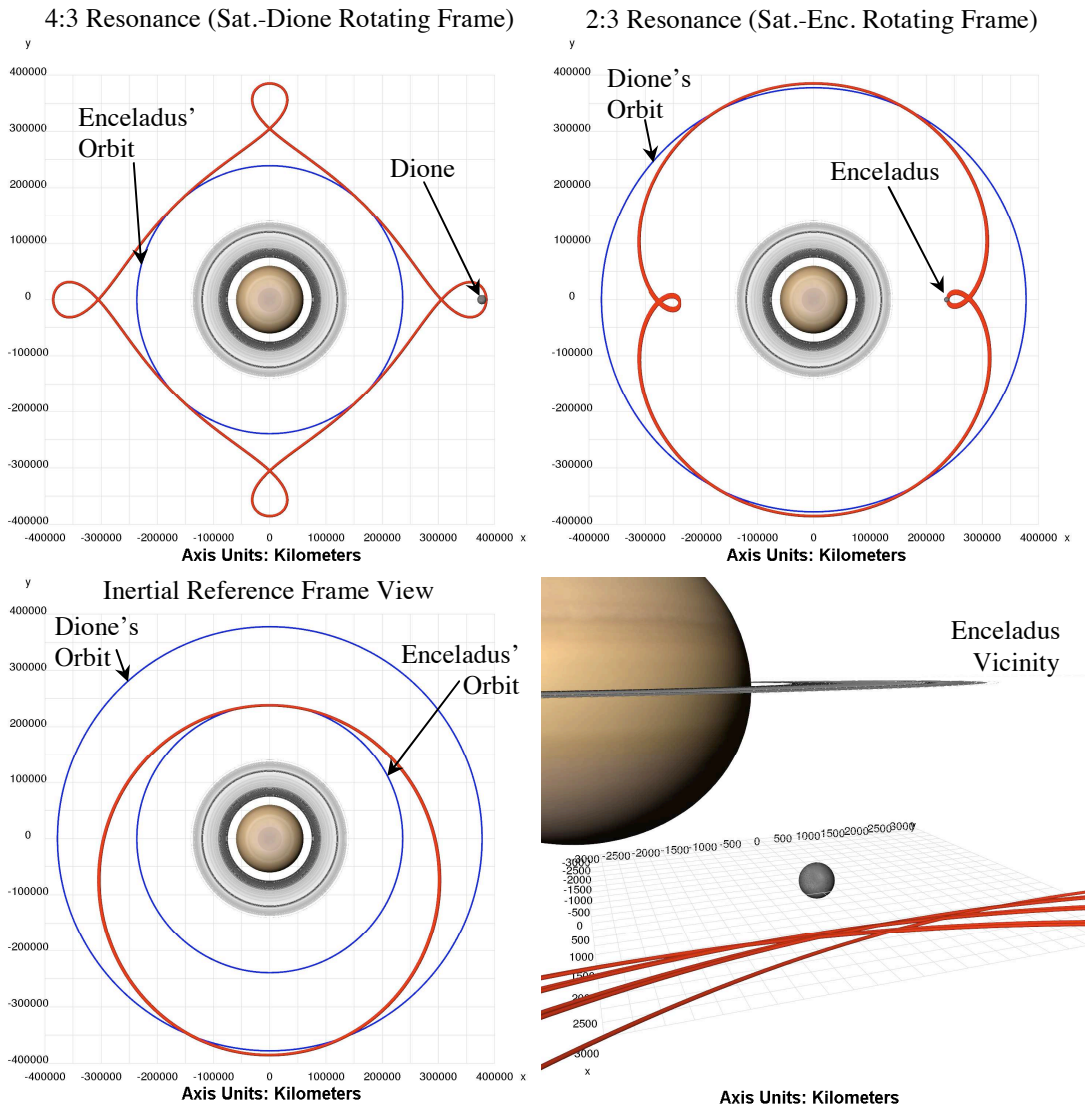

Figure 4.12 A 4:3 resonant orbit from the Saturn-Dione CR3BP viewed also in the Saturn-Enceladus rotating frame, the inertial reference frame.

finally, a perspective view displaying details of the orbits in the immediate vicinity of Enceladus. The red trajectory in each plot corresponds to the orbital motion of the spacecraft, while the blue trajectories result from the orbital motion of Enceladus, Dione, or both. To aid in their visibility, the sizes of both Enceladus and Dione are magnified by a factor of 20 in Figures 4.10-4.12. Note that none of the orbits in these figures form perfectly closed orbits in the Saturn-Enceladus rotating reference frame; the orbits in Figures 4.10-4.12 are targeted to achieve periodicity in the Saturn-Dione rotating frame to within some preset numerical tolerance. Of course, the trajectories in the Saturn-

Enceladus rotating reference frame are generally quasi-periodic due to the imprecise nature of the 2:1 resonance between Dione and Enceladus. Consequently, the quasi-periodic resonant orbits between Dione and Enceladus actually do resemble their ephemeris counterparts qualitatively; in fact, they are a better representation than perfectly periodic orbits.

4.5 A Six-Body Dynamical Model of the Saturnian System

Each of the resonant orbits in Figures 4.10-4.12 passes closer to Enceladus than to Dione. Recall that Dione's gravitational influence is included in the restricted three-body model used to correct these resonant orbits, but Enceladus' gravity is neglected. The resonant orbits in Figures 4.10-4.12 necessitate the introduction of a new dynamical model of the Saturnian system; a dynamical model that includes additional gravity fields beyond the two included in the CR3BP.

4.5.1 Natural Saturnian Satellites

The expanded dynamical model is used to design trajectories that fly by more than one Saturnian moon. As of 2008, as many as 60 natural satellites are known to exist in the Saturnian system, and are classified as moons, in addition to the countless particles that populate Saturn's rings. There is little incentive to include every one of Saturn's moons in a new dynamical model. Many of Saturn's moons are quite small and orbit far beyond the larger inner moons that are the focus of this investigation. In addition, the orbits of many of Saturn's newly discovered tiny moons are poorly defined in terms of their orbital parameters and, therefore, cannot be accurately modeled. Thus, a limited number of the most massive moons of Saturn are incorporated. With the exception of massive Titan, the gravitational influence of the remaining Saturnian satellites is only significant during a close flyby. Since these close flybys are unlikely to occur

unintentionally, the only moons that are incorporated in the model are those moons that are used as flyby bodies in the current analysis.

In this investigation, the expanded multi-body dynamical model of the Saturnian system includes only the gravitational influence of the most massive of the Saturnian satellites located within the orbit of Titan. Specifically, the moons that are incorporated into the model include: Enceladus, Tethys, Dione, Rhea, and Titan. This sampling of moons includes a wide range in terms of both orbit size and satellite mass. The masses and relevant dynamical data for each of these Saturnian moons appear in Table 4.3 [6].

Table 4.3 Physical properties of Saturn and five of its larger inner moons.

Gravitational Body	Mass (kg)	$Gm\left(\frac{km^3}{kg \cdot s^2}\right)$	Semi-Major Axis (km)	Radius (km)	Eccentricity	Inclination (degrees)
Saturn	$5.68428e^{26}$	37931207.58	-	60268	-	-
Enceladus	$1.08041e^{20}$	7.209544429	238413.5	256.3	0.005045992	0.016
Tethys	$6.17416e^{20}$	41.2001472	294977.47	529.8	0.000821697	1.0895
Dione	$1.09565e^{21}$	73.11284589	377649.63	560	0.002415667	1.0126
Rhea	$2.30691e^{21}$	153.9401336	527234.25	764	0.001252151	0.3472
Titan	$1.34544e^{23}$	8978.137176	1222276.4	2575	0.02903215	0.2949

Among the remaining Saturnian moons that are excluded from the six-body dynamical model, only Iapetus possesses a mass greater than Dione, Tethys, and Enceladus. Iapetus is ignored because it orbits approximately three times further than Titan from Saturn. No targeted flybys of moons at this distance are included. Another of Saturn's moons, Mimas, is also of comparable size to Enceladus. However, because of Mimas' close proximity to Saturn's rings, this moon is a less desirable flyby target, and it is thus ignored.

4.5.2 Formulation of the Six-Body Model of the Saturnian System

The six-body model of the Saturnian system supports simulations of spacecraft motion under the gravitational influence of Saturn, Enceladus, Tethys, Dione, Rhea, and Titan. As such, the model incorporates the gravitational influence of each of these moons

while simultaneously modeling the relative motion of these bodies under their mutual gravitational interactions. It is assumed in the formulation of the six-body model that the five Saturnian moons are in circular co-planar orbits around Saturn. As seen in Table 4.3, the orbits of all five moons actually possess an eccentricity less than 0.03, and the eccentricity of the smaller four moons is an order of magnitude smaller. The inclination of each of the moons is also less than 1.1 degrees. Thus, the physical properties of the orbits justify the simplifying assumptions in the multi-body model of the Saturnian system. In the six-body model, it is also assumed that Saturn's position remains fixed at the origin of the system and the orbits of the moons are co-planar with the ring plane of Saturn. The primary advantage of this six-body model of the Saturnian system, is that the gravitational influence of all six bodies are included continuously throughout the entire simulation.

The equations of motion for the spacecraft in the six-body system are simply an implementation of the vector form of Newton's second law and the law of universal gravitation, that is,

$$\overline{R}_S'' = -G\sum_{i=1}^{6}\frac{m_i(\overline{R}_S - \overline{R}_i)}{R_{iS}^{\ 3}}, \tag{4.1}$$

where the subscript i identifies the gravitational body of interest from the list including: Enceladus, Tethys, Dione, Rhea, Titan, and Saturn. In Equation 4.1, $\overline{R}_S$ is the vector defining the position of the spacecraft relative to Saturn and $\overline{R}_i$ similarly defines the position of the i^{th} gravitational body. A pictorial definition of the position vectors in Equation 4.1 is included in Figure 4.13. Since the position of Saturn is fixed at the origin of the six-body model, two vectors included in the summation on the right side of Equation 4.1 do not appear in Figure 4.13; $\overline{R}_6$ is of length zero and $\overline{R}_{6S}$ is identical to the vector $\overline{R}_S$.

Unlike the derivation of the traditional three-body problem equations of motion in Chapter 2, this six-body model of the Saturnian system does not incorporate

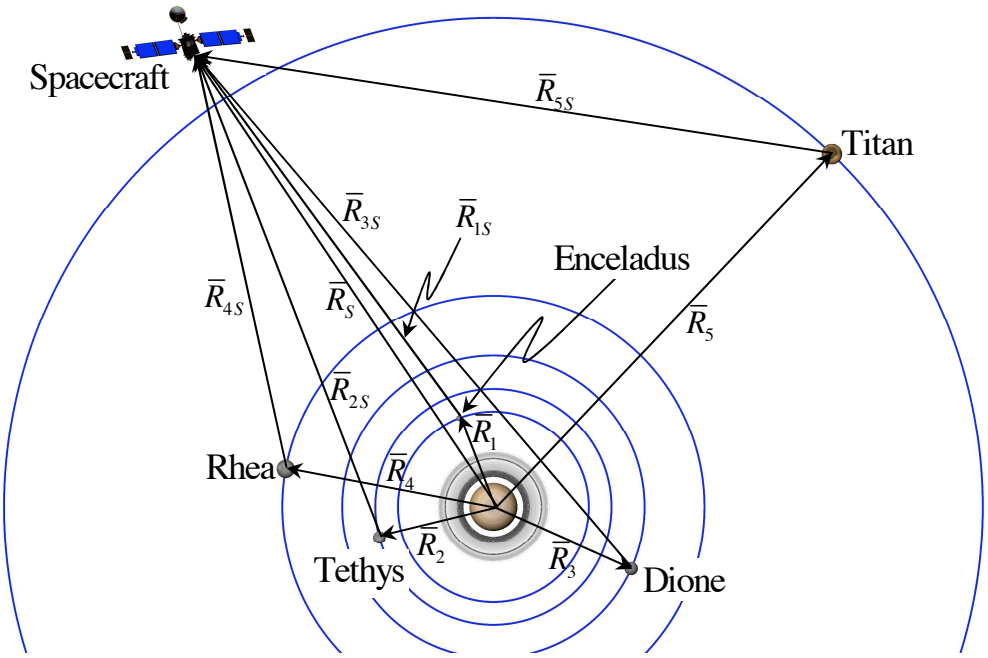

Figure 4.13 Vector definition of the six-body dynamical model of the Saturnian system.

non-dimensionalization prior to numerical integration. In addition, all integrations in this six-body model are performed relative to the inertial coordinate frame rather than a rotating reference frame, though the resulting trajectory is transformed into the rotating coordinates associated with each of the moons included in the six-body model. Unlike the rotating reference frame defined for the CR3BP, one which is centered on the barycenter, the rotating frames associated with the five moons in the six-body model are centered on Saturn; this minute difference in the origin position is only 0.02% of the radius of the moon's orbit for even the most massive body, Titan, and at least two additional orders of magnitude smaller for the other moons.

The orbits of the five moons in this six-body model are not numerically integrated. The moons are assumed to move in circular co-planar orbits around Saturn. Thus, their positions as a function of time are found analytically as,

$$x_i = a_i \cdot \cos\left(\theta_{i_0}^* + t \cdot N_i\right), \tag{4.2}$$

$$y_i = a_i \cdot \sin\left(\theta_{i_0}^* + t \cdot N_i\right), \tag{4.3}$$

where N_i is the mean motion of moon *i* and $\theta_{i_0}^*$ is an initial value of true anomaly for the orbit of each moon obtained from an ephemeris file at an arbitrary epoch to provide a realistic configuration for the moons at the initial time. An analytical definition for the positions of the moons is superior to integrating their circular motion around Saturn both because the analytical method is computationally less expensive and does not accumulate any numerical error during long simulations.

4.5.3 Quasi-Periodic Resonant Orbits in the Six-Body Model

The six-body model of the Saturnian system reflects a more physically realistic dynamical model to simulate the motion of a spacecraft as it moves along a resonant orbit that passes near both Dione and Enceladus. Recall that the resonant orbits in Figures 4.10-4.12 are the result of applying differential corrections to a spacecraft trajectory propagated in the Saturn-Dione CR3BP. As the resonant orbits in Figures 4.10-4.12 pass within a few hundred kilometers of the surface of Enceladus, it is reasonable to further examine these orbits in a model that incorporates the gravity field of Enceladus.

As the initial positions of Dione and Enceladus are not generally aligned in the six-body model, transferring the resonant orbits in Figures 4.10-4.12 to the six-body model requires careful consideration of timing. First, an inertial state along the reference resonant orbit is selected from the orbit calculated in the CR3BP. Integration in the six-body model using this selected inertial state as an initial condition generally results in a quasi-periodic resonant orbit that qualitatively resembles the trajectory from the CR3BP. However, the trajectory in the six-body model is generally not symmetric across the *x*-axis of the Saturn-Dione rotating reference frame. As a result, the trajectory precesses further from a closed trajectory than is the case when a particular perikrone or apokrone passage is forced to lie along the *x*-axis of the Saturn-Dione rotating frame. A transformation matrix rotates the initial integration state such that the resulting quasi-

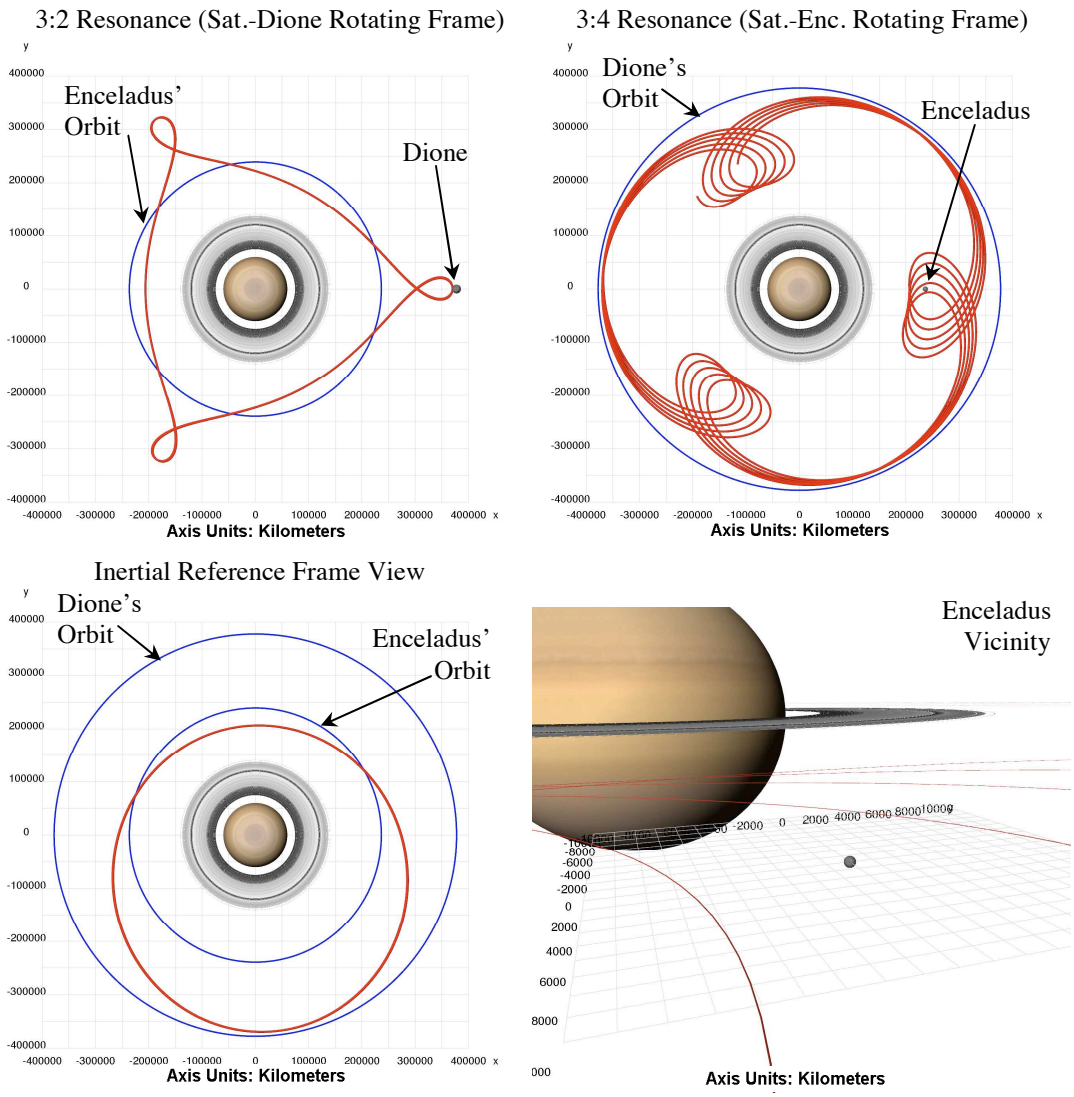

Figure 4.14 A 3:2 Dione resonance and 3:4 Enceladus resonance simulated in the six-body model of the Saturnian system.

periodic resonant orbit is nearly symmetric in the Saturn-Dione rotating frame. Once the initial spacecraft state is rotated, the perikrone of the orbit is forced to an orientation near Enceladus by altering the starting integration epoch to alter the initial position of Enceladus relative to Dione.

The trajectories in the six-body problem that result from integrating the inertial states obtained from the resonant orbits in Figures 4.10-4.12 are nearly periodic in the Saturn-

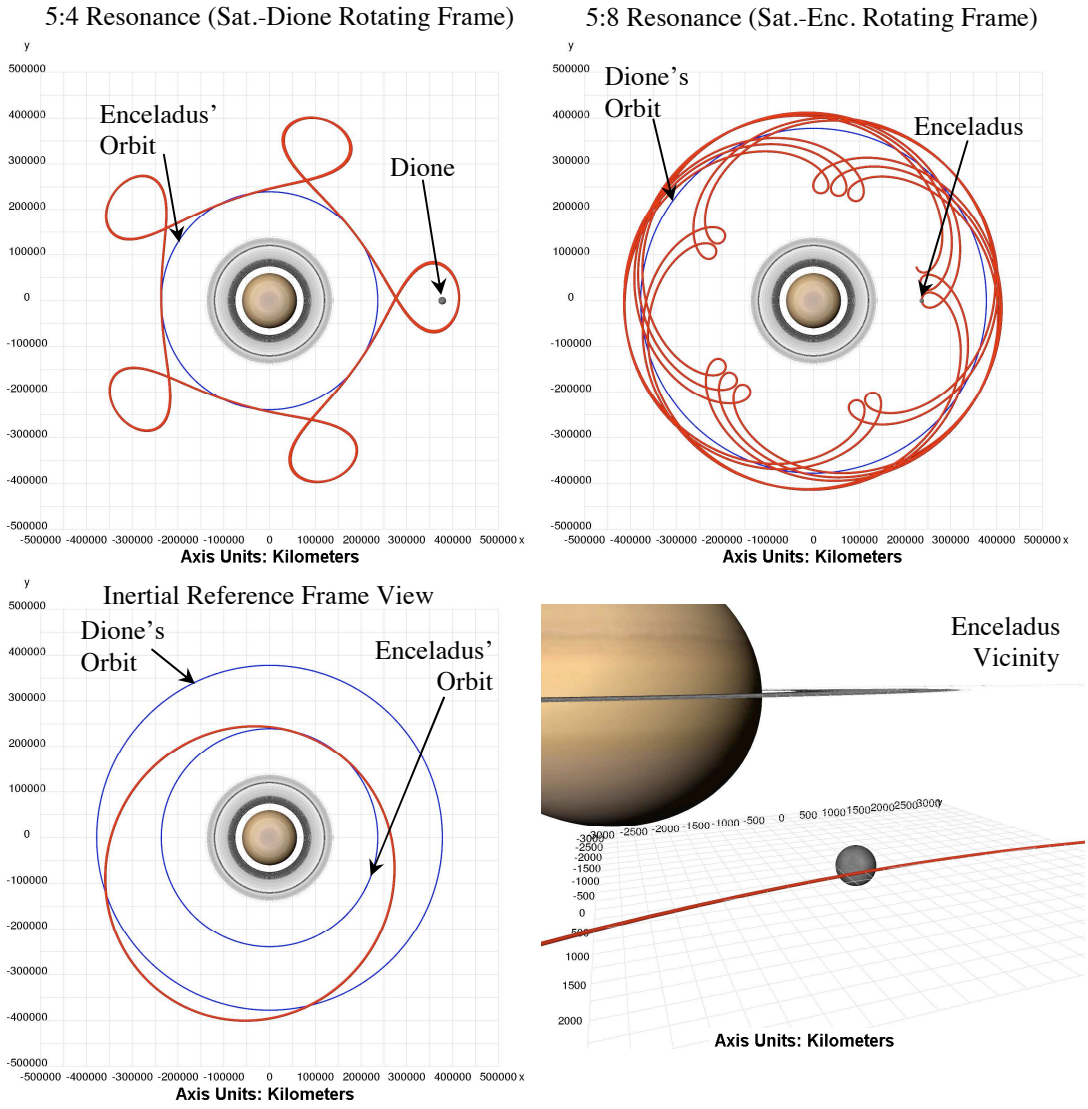

Figure 4.15 A 5:4 Dione resonance and 5:8 Enceladus resonance simulated in the six-body model of the Saturnian system.

Dione rotating frame for two of three test cases. These three examples are plotted in Figures 4.14-4.16. Note that for the 3:2 and 5:4 resonant trajectories with Dione in Figure 4.14 and 4.15, the quasi-periodic resonant orbit remains nearly closed throughout an integration period equal to ten revolutions of Dione around Saturn. The stability of these resonant orbits over an indefinite period of time is not examined in this investigation.

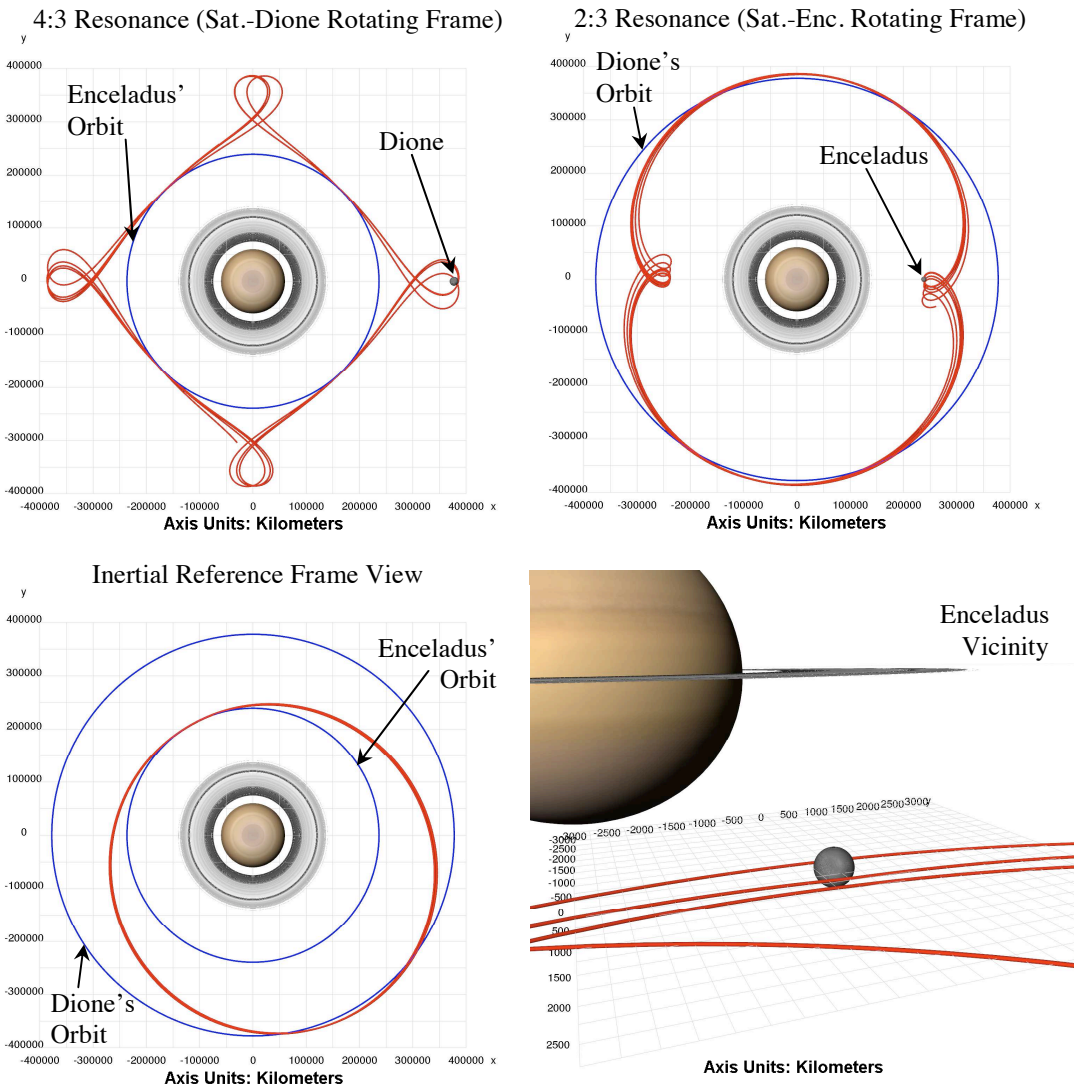

Figure 4.16 A 4:3 Dione resonance and 2:3 Enceladus resonance simulated in the six-body model of the Saturnian system.

The resonant orbits in Figure 4.10-4.12 are selected for further examination precisely because they pass close to multiple gravity fields. However, despite the additional perturbing influences in the six-body model of the Saturnian system, the conditions associated with a resonant orbit calculated in the Saturn-Dione CR3BP successfully produce a nearly closed quasi-periodic resonant orbit in the Saturn-Dione rotating frame.

Not surprisingly, the additional gravitational perturbations in the six-body problem result in trajectories in the Saturn-Enceladus rotating frame that display precession of the

perikrone loops relative to Enceladus. As a result of the precession relative to Enceladus, only a single close Enceladus flyby occurs in the 5:8 resonance plotted in Figure 4.15; the spacecraft approaches Enceladus to within approximately 600 km only once. Despite the lack of periodicity in the trajectories relative to the Saturn-Enceladus rotating frame as apparent in Figure 4.14 and 4.15, the conditions associated with these resonant orbits calculated in the Saturn-Dione CR3BP produce very nearly periodic resonant trajectories in the six-body model of the Saturnian system.

Additional insight into the multi-body nature of the dynamical interactions in the six-body model of the Saturnian system is available from the 4:3 resonant trajectory in Figure 4.16. Unlike the 3:2 and 5:4 resonant orbits in Figure 4.14 and 4.15, the computation of a nearly periodic 4:3 resonant orbit, one that retains the characteristics apparent in the trajectory plotted in Figure 4.12, is substantially more challenging in the six-body model. Although the quasi-periodic orbits relative to the Saturn-Dione rotating reference frame in Figures 4.14 and 4.15 formed nearly closed trajectories, the trajectory in Figure 4.16 lacks the same nearly-periodic structure. Instead, noticeable precession of the apokrone loops relative to Dione in the Saturn-Dione rotating frame is apparent after just 2.5 resonant periods. Interestingly, while the trajectories in Figures 4.14 and 4.15 yield only a single Enceladus flyby during numerical simulation in the six-body model, the trajectory in Figure 4.16 produces four close Enceladus flybys. This counterintuitive result is actually a consequence of an unintentional close flyby of an additional Saturnian moon included in the six-body model of the Saturnian system, that is, Tethys. During the simulation of the trajectory in Figure 4.16, the spacecraft encounters Enceladus twice and Dione once before it passes within 2000 km of Tethys. The Tethys flyby, displayed in Figure 4.17, has the unintended effect of slightly reshaping the orbit of the spacecraft following the flyby. As a result of the incidental flyby of Tethys, the 4:3 Dione resonant orbit in Figure 4.16 lacks the nearly periodic structure displayed by the trajectories in Figures 4.14 and 4.15. Note, however, that additional Enceladus flybys occur during the simulation in Figure 4.16 as a result of the small changes in the spacecraft orbit following the Tethys flyby.

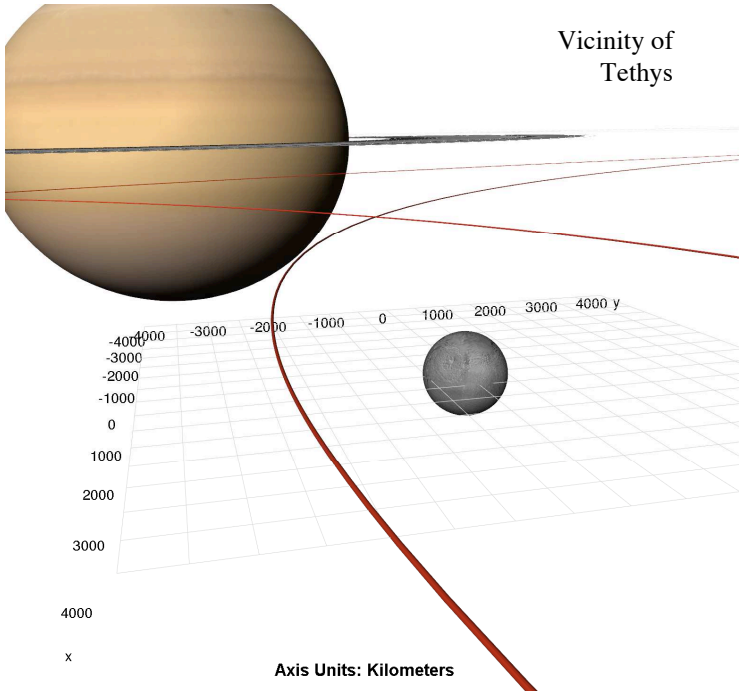

Figure 4.17 A non-targeted Tethys flyby during the simulation of the 4:3 (spacecraft: Dione) resonant orbit in the six-body Saturnian system model.

Three results from the analysis of resonant orbits in the Saturnian system are notable. First, the previously displayed resonant orbits offer a means to periodically encounter Enceladus. These trajectories yield periodic close encounters with Enceladus without the added difficulty of entering orbit around Enceladus. As such, resonant orbits are one possible alternative to entering orbit around Enceladus. Second, it is relatively straightforward to design resonant orbits in the Saturnian system that encounter multiple Saturnian moons, at least quasi-periodically. By exploiting natural resonances within the Saturnian system, resonant trajectories similar to the trajectories in Figures 4.10-4.12 offer frequent passes of multiple Saturnian moons. Based on this analysis of resonant orbits, a third observation is that these resonant solutions do exist in higher fidelity dynamical models of the Saturnian system, although strict periodicity is lost through the addition of perturbing influences. The trajectories in Figures 4.14-4.16 supply evidence that it is possible to determine resonant trajectories that encounter both Enceladus and Dione multiple times along a single ballistic trajectory.

The resonant orbits calculated in this investigation are of relatively low orbital energy when compared to orbits with apokrone beyond even the distance of Titan's orbit. To utilize one of the resonant orbits from this analysis, it is necessary to quantify the reduction in orbital energy relative to Saturn that is required to match the energy of a resonant orbit.

5. DESIGN OF SEQUENCES OF FLYBY TRAJECTORIES IN THE SATURNIAN SYSTEM

To date four spacecraft have encountered Saturn. Of those four, three spacecraft passed Saturn on hyperbolic trajectories relative to the planet: Pioneer 11, Voyager 1, and Voyager 2. Only Cassini, the fourth and most recent spacecraft to encounter Saturn, performed a large propulsive maneuver to achieve capture into orbit around Saturn. For Cassini, the Saturn orbit insertion maneuver and the follow-up maneuver to raise the perikrone altitude above Saturn's rings required 1300 kg of propellant, a full 45% of the fuel that the spacecraft carried at launch in 1997, and altered the velocity of Cassini by 1,019 m/s [51]. Cassini's initial orbit around Saturn possessed a period of 155 days [52], and on this orbit, Cassini crossed the orbital path of Enceladus at a velocity in excess of 17 km/s relative to Saturn. To enter orbit around Enceladus or to directly insert into one of the previous resonant orbits, a spacecraft entering the Saturnian system is required to dramatically reduce its orbital energy relative to Saturn to a level comparable with the desired final orbit. Some reductions in orbital energy can be accomplished with propulsive maneuvers. However, in the case of Cassini, the sum of all propulsive maneuvers through the end of the primary mission resulted in a total change in velocity of less than 2 km/s [51]. If Cassini's initial orbit around Saturn is used as an approximate baseline initial orbit for a future mission in the Saturnian system, clearly the bulk of the reduction in orbital energy relative to Saturn must result from gravity-assist flybys of Saturn's moons. All of the reference solutions presented in the Enceladus Flagship Mission Concept Study [4] incorporated gravity-assist flybys of Titan and some included gravity-assist flybys of additional Saturnian moons.

In this investigation, sequences of gravity-assist flybys of Saturn's moons are designed in a six-body model using an algorithm that incorporates a constrained local optimization routine. However, prior to the design of flyby sequences, it is first useful to

quantify the magnitude of the equivalent ΔV that can result from gravity-assist flybys of each of the Saturnian moons that are incorporated in the six-body model of the Saturnian system.

5.1 Comparison of Gravity-Assist Flybys in the Patched Conic Model and CR3BP

Although sequences of flyby trajectories are designed using a six-body model of the Saturnian system, the CR3BP is a more useful model for examining the accuracy of the patched conic approximations during the flyby trajectories. If the results of a gravity-assist trajectory simulated in a six-body model are compared to the results from a patched conic analysis, interpretation requires caution. It is not possible to definitively demonstrate whether differences between the results from the six-body and the patched conic models result from systematic errors associated with the instantaneous transition between conic frames in the patched conic case, or whether differences are due to the perturbing influence of additional gravitational sources in the six-body model. Thus, the circular restricted three-body problem is again selected as the dynamical model to quantify the effects of gravity-assist flybys. Directly comparing the results from the patched conic model to results simulated in the CR3BP allows differences resulting from the addition of the gravity field of P_2 to be isolated.

A background discussion concerning the mechanics of a gravity-assist flyby is included in Chapter 2. Recall that the three key parameters in a gravity-assist flyby include (i) ΔV_{eq}, the equivalent velocity change that results from the flyby, (ii) V_∞, the hyperbolic excess velocity of the spacecraft relative to the moon during the flyby, and (iii) r_c, the distance of the spacecraft's closest approach to the flyby body. While all three of these quantities are well defined within the patched conic model, the definition is more complex when flybys are modeled in the CR3BP. In the CR3BP, the scalar quantity V_∞, is calculated in this investigation as the difference between the inertial velocity of the spacecraft and the inertial velocity of the moon at the moment of the closest approach of the spacecraft to the flyby body. The equivalent change in velocity

that results from the flyby, ΔV_{eq}, is computed in the CR3BP as the difference between the predicted velocity of the spacecraft at the moment of closest approach to the flyby body based on two different calculations. First, the instantaneous conic orbit of the spacecraft as it enters the flyby body's Hill's sphere is used to analytically predict the velocity at closest approach. A second prediction is generated from the spacecraft state as the vehicle exits the Hill's sphere; the exit state yields conic elements and the close approach velocity is again approximated. For additional detail on the calculation of ΔV_{eq} and V_∞ in both the patched conic model and CR3BP, refer to Chapter 2.3.2.

The value of ΔV_{eq} that results from a gravity-assist flyby varies tremendously based on the size of the flyby body (Table 5.1), the distance of closest approach to the flyby body, r_c, and the V_∞ of the spacecraft relative to the flyby body. For a comprehensive understanding of the expected magnitude of ΔV_{eq} resulting from a specific gravity-assist flyby, a wide range of possible values of V_∞ and r_c are explored within the contexts of the CR3BP for encounters with five different moons: Enceladus, Tethys, Dione, Rhea, and Titan. Since the perikrone altitude of the initial spacecraft orbit is held constant, that is, r_p = 188,825 km for these simulations, the value of V_∞ for each gravity-assist flyby is modified by altering the apokrone altitude of the initial spacecraft orbit relative to Saturn; orbits with larger apokrone altitudes possess higher values of V_∞ during the simulated flybys. As many as nineteen different values of apokrone altitude, within a given range, 245,472 km < r_a < 3,560,782 km, are simulated for flybys of each of the five moons. The 19 orbits used to simulate gravity-assist flybys in the CR3BP are plotted in Figure 5.1. Only those orbits, from the 19 that appear in Figure 5.1, that cross the orbital path of a moon are used to simulate flyby trajectories associated with that particular moon. For example, all 19 orbits in Figure 5.1 are used to simulate flybys of Enceladus, but only the seven outermost orbits are used in simulations involving Titan because the remaining 12 orbits never travel sufficiently far from Saturn to reach the orbit of Titan.

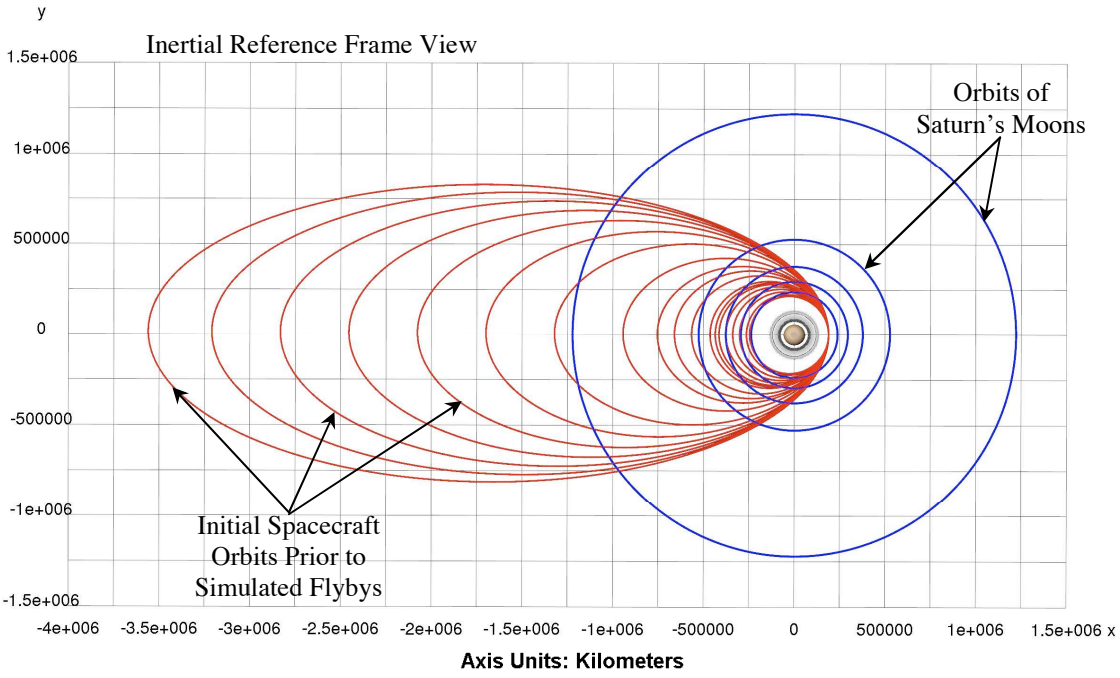

Figure 5.1 Nineteen initial spacecraft orbits utilized in simulations of gravity-assist flybys of Enceladus, Tethys, Dione, Rhea, and Titan.

The 19 orbits from Figure 5.1 result in values of V_∞ within the following range: 1 km/s < V_∞ < 10 km/s. Of course, the value of V_∞ for a particular orbit varies depending on the flyby moon. For each value of V_∞, several flyby distances, r_c, are examined. In general, r_c is modified by increments of 50 km beginning with trajectories that nearly impact the flyby body and extending to trajectories that pass just within the boundary of the Hill's sphere that is associated with the flyby body. To demonstrate a gravity-assist flyby of Titan with a fixed value of V_∞ but a variable r_c, consider the trajectories plotted in Figure 5.2. In Figure 5.2, a total of 130 gravity-assist flyby trajectories of Titan are plotted. Each of the trajectories in Figure 5.2 possesses a flyby velocity relative to Titan with approximately the same magnitude, $V_\infty \approx 6.63$ km/s. However, while the flyby velocity is held constant, the flyby altitude, r_c, varies from just 65 km above Titan's surface to the edge of the Titan Hill's sphere, some 52,000 km from the center of the

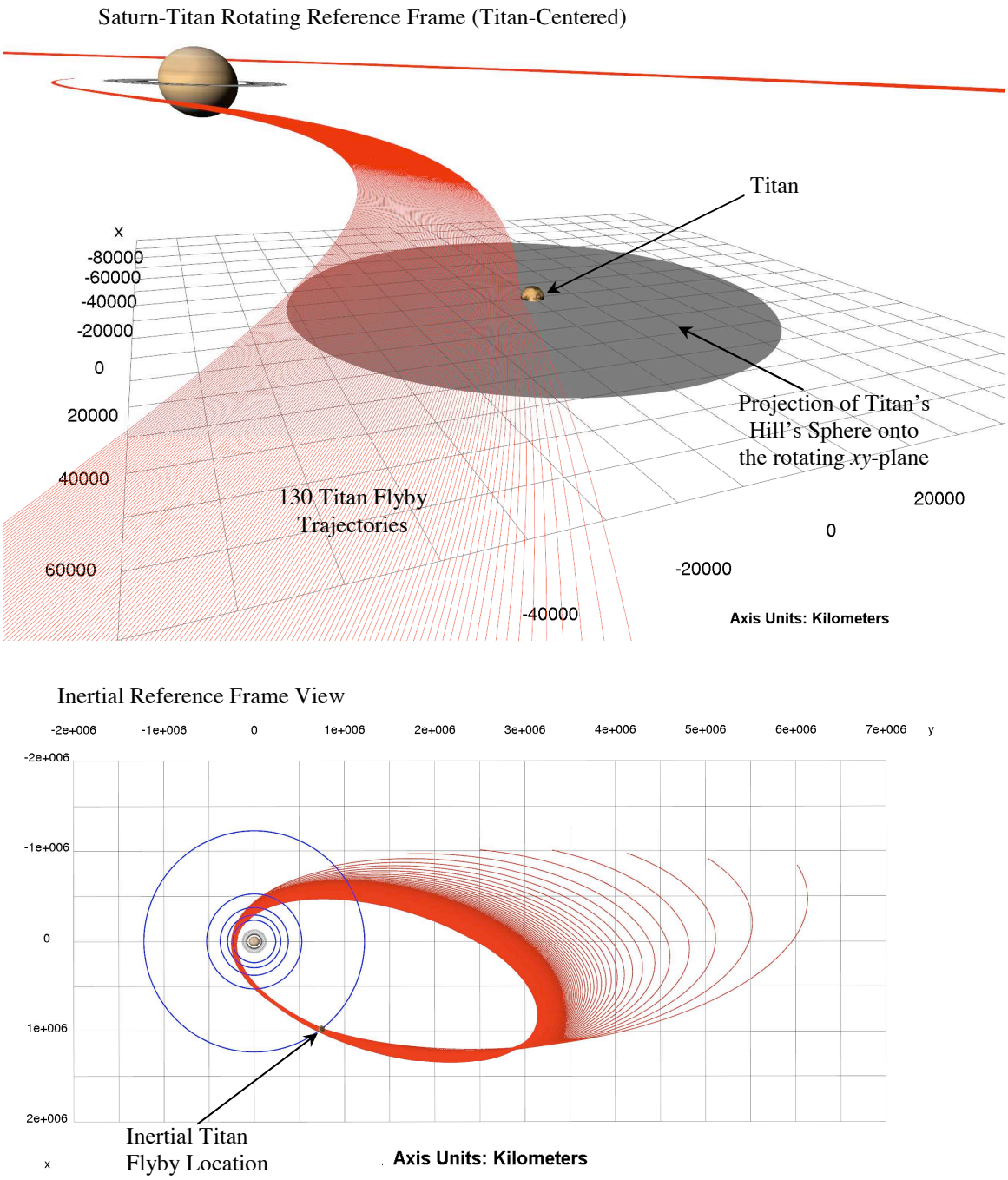

Figure 5.2 Titan flyby trajectories with various flyby altitudes, all originating from an orbit sized: r_p = 188,825 km and r_a = 3,210,022 km.

moon. The Titan Hill's sphere is projected onto the rotating frame *xy*-plane in the upper plot in Figure 5.2, and is visible as a silver disk of radius ~52,000 km. As the flyby trajectories in Figure 5.2 pass *behind* Titan in its orbital motion around Saturn, the flybys

are expected to result in an increase in orbital energy. Indeed, the lower plot in Figure 5.2 demonstrates that there is a marked increase in the apokrone distance of the spacecraft orbit, r_a, as a result of several of the Titan flybys. As expected, the increase in apokrone altitude is largest for the trajectories that pass closest to Titan, while the trajectories that pass near the very edge of the Hill's sphere are perturbed by Titan to a much smaller degree. In Figure 5.2, the orbits of Enceladus, Tethys, Dione, Rhea, and Titan appear in blue. However, note that the trajectories in Figure 5.2 result from simulations in the Saturn-Titan CR3BP; the gravity of the four inner moons is not included.

To quantify the magnitude of the velocity change, ΔV_{eq}, that results from flybys of Enceladus, Tethys, Dione, Rhea, and Titan, simulations are carried out within the CR3BP associated with Saturn and each of the five moon. In these simulation either V_∞ or r_c is held fixed while the other quantity is allowed to vary. The results indicate the potential impact of each moon in reshaping the orbit. For the trajectories plotted in Figure 5.2, the shape of the initial spacecraft orbit around Saturn is held fixed such that r_p = 188,825 km and r_a= 3,210,022 km and, as a result, the flyby velocity, V_∞, remains approximately constant regardless of the flyby altitude. In this way, the sensitivity of ΔV_{eq} to variations in flyby altitude is probed in the CR3BP. For each of the moons that are included in the Saturnian system six-body model, gravity-assist flybys at varying flyby distances, r_c, are simulated for a particular initial orbit size. The orbit of Enceladus is closer to Saturn than the orbit of Titan. Therefore, if a spacecraft trajectory crosses the orbits of both moons, then it must cross Titan's orbit at a lower V_∞ than when it crosses Enceladus' orbit. For this reason, different spacecraft orbits are used to evaluate each moon, so that values of V_∞ remain nearly constant regardless of the flyby body. The flyby trajectories represented in Figure 5.3 are selected for examination because these simulations all possess a similar value of flyby velocity, that is, $V_\infty \approx$ 5.0-5.5 km/s. This range of V_∞ values is arbitrary and is used only for uniformity in the comparisons of the gravitational

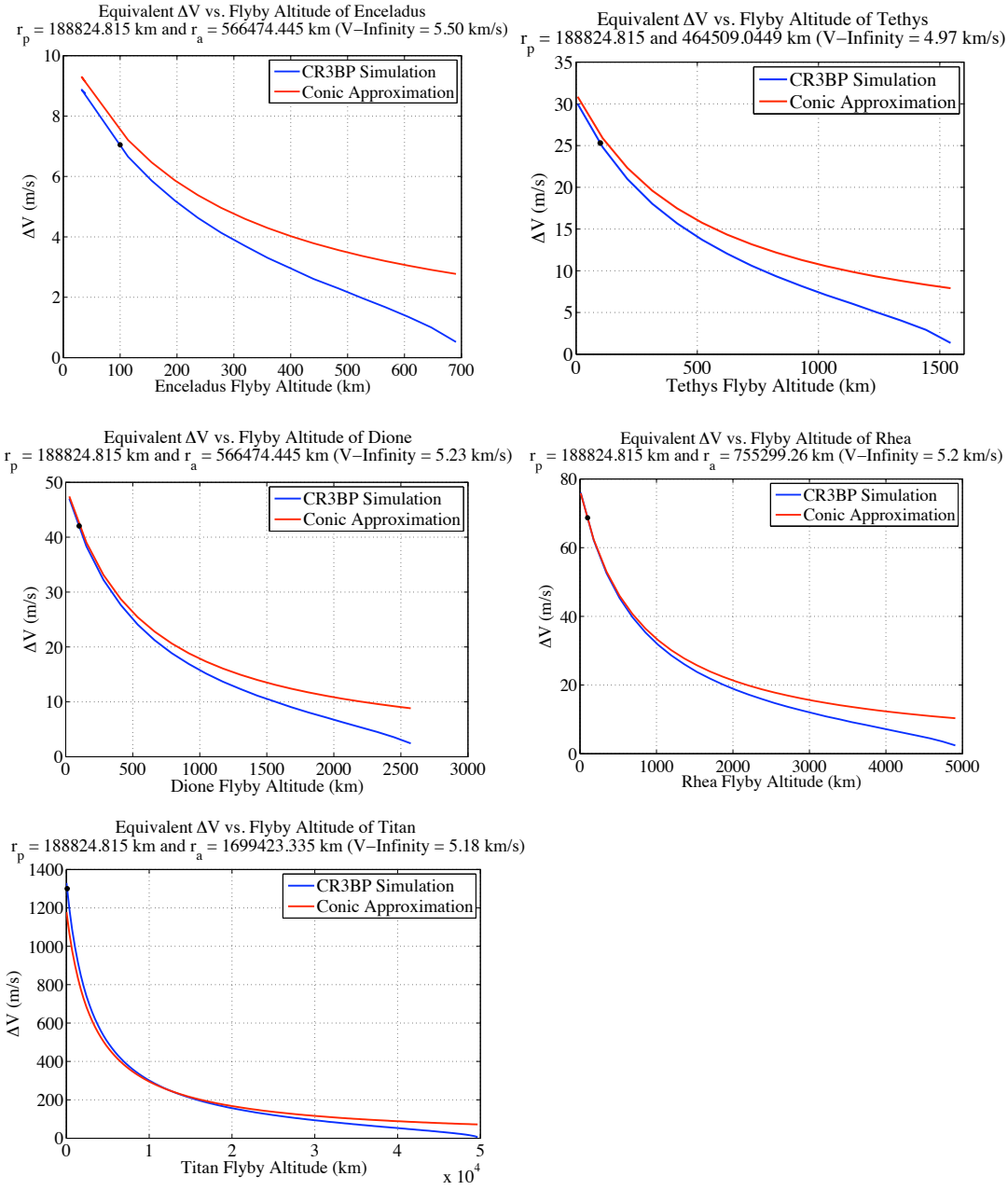

Figure 5.3 Values of ΔV_{eq} computed in both the conic and three-body models for flybys of varying altitudes relative to Enceladus, Tethys, Dione, Rhea, and Titan.

influence of each moon. In Figure 5.3, the value of ΔV_{eq} that is computed during the CR3BP simulations (Equation 2.65) is plotted in blue, while the ΔV_{eq} that is calculated from the patched conic relationship in Equation 2.63 appears in red. In Figure 5.3, note

the range along the vertical axis. The magnitude of the ΔV_{eq} values on the *y*-axis vary tremendously depending on the flyby body.

In Figure 5.3, the conic approximation for ΔV_{eq} is nearly always higher than the value calculated in the CR3BP. However, the conic ΔV_{eq} is closer to the computed value in the three-body model for low altitude flybys of each moon; the conic and three-body values of ΔV_{eq} diverge for passes at higher altitude. This result is actually quite intuitive. Recall that the three-body calculation for ΔV_{eq} is derived from the state of the spacecraft at the edge of the Hill's sphere of the flyby body (Equation 2.65). Therefore, trajectories that pass very near the flyby moon spend a longer period of time within the moon's Hill's sphere than trajectories that only graze the edge of the Hill's sphere. Since the ΔV_{eq} calculation in the CR3BP is based on the difference between the orbital state of the spacecraft as it enters and exits the Hill's sphere, sufficient time must pass between those two events for the moon's perturbing influence to appreciably affect the spacecraft trajectory. Thus, the value of ΔV_{eq} for high altitude flybys in the CR3BP approaches zero more quickly than the values of ΔV_{eq} evaluated using the conic equations.

Based on an examination of the ΔV_{eq} magnitudes in Figure 5.3, Titan is the most significant moon for use in gravity-assist trajectories. Low altitude flybys of Titan can achieve a ΔV_{eq} that is 15 times larger in magnitude than flybys of the next largest moon, Rhea. Trajectories that pass near Titan with a flyby velocity of ~5 km/s can achieve a ΔV_{eq} larger than 1 km/s. For comparison, recall that Cassini, NASA's current Saturn orbiting probe, was launched with only enough propellant to accomplish a total velocity change, ΔV_{eq}, equal to ~2 km/s over the entire 11-year prime mission, yet Figure 5.3 demonstrates that a single Titan flyby can accomplish nearly the same total ΔV_{eq} magnitude for free, that is, without expenditure of propellant.

The results in Figure 5.3 reflect the variation of ΔV_{eq} as a function of flyby altitude. However, ΔV_{eq} is also dependent on the flyby velocity, V_∞. Additional trajectories are

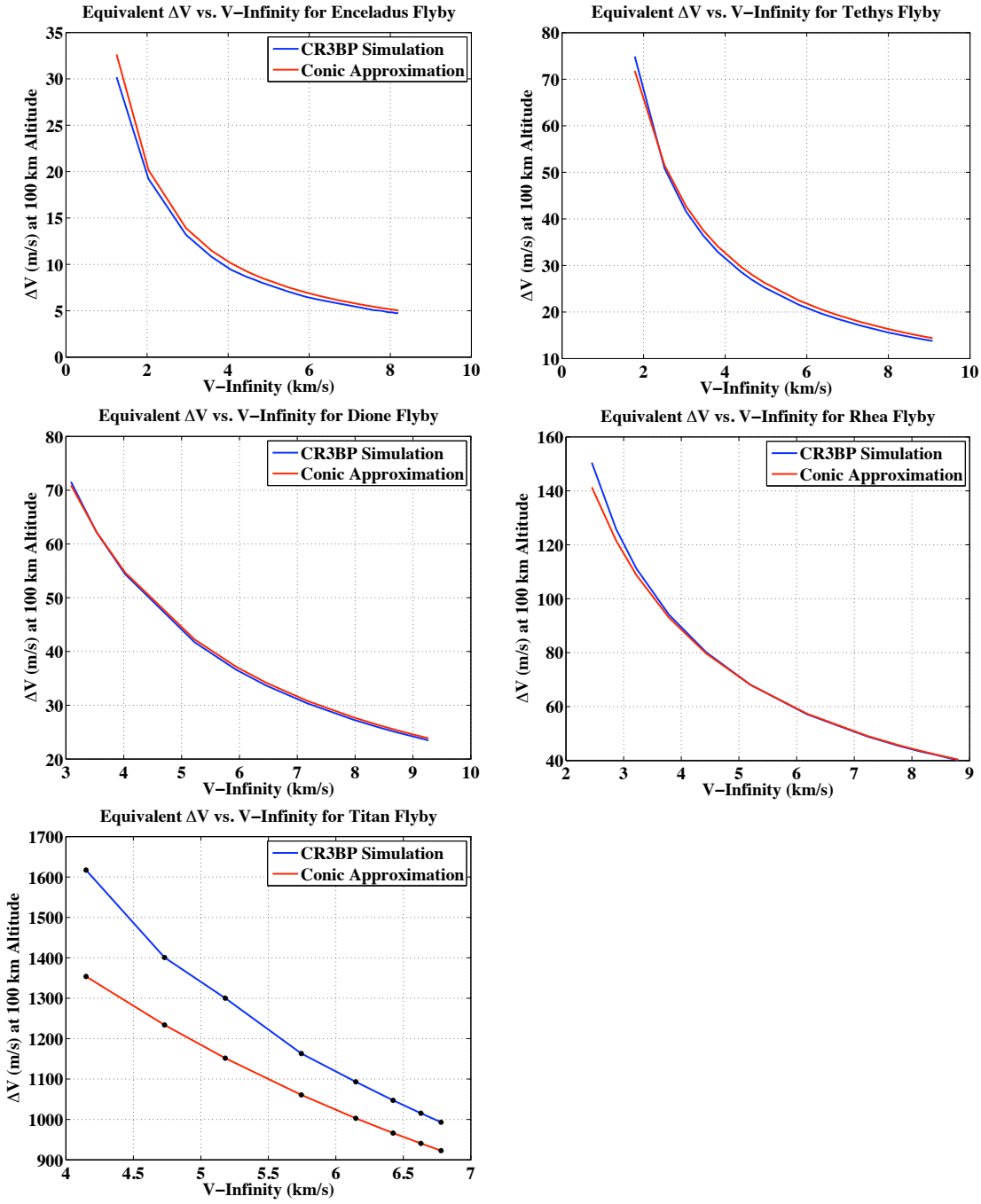

Figure 5.4 Comparison between the ΔV_{eq} associated with 100 km altitude gravity-assist flybys computed in both the patched conic and restricted three-body model for various values of V_{∞}.

simulated where the flyby altitude above each moon is fixed at 100 km and a range of flyby velocities, V_∞, are simulated. The results of these simulations appear in Figure 5.4, where the values of ΔV_{eq} computed from simulations in the CR3BP appear in blue, while the patched conic values of ΔV_{eq} calculated from Equation 2.63 appear in red.

In Figure 5.4 the trends for all five plots appear qualitatively similar, but the magnitude of ΔV_{eq} resulting from flybys of each moon vary. In general, the patched conic approximation of ΔV_{eq}, as reflected in Figure 5.4, tends to overestimate the gravitational influence of the inner Saturnian moons (i.e., Enceladus, Tethys, and Dione) while underestimating the value of ΔV_{eq} computed in the three-body simulations involving Rhea and Titan. The discrepancy between the patched conic calculation of ΔV_{eq} and the value evaluated from data produced in the CR3BP is most pronounced in the results of the flybys of Titan. This discrepancy results from the imprecise definition of V_∞ used in this analysis to represent this quantity in the CR3BP. In the three-body problem, V_∞ is assumed to be the velocity of the spacecraft relative to the flyby body at the moment of closest approach. This definition of V_∞ in the CR3BP relies on two tacit assumptions. First, that the magnitude of the velocity of the spacecraft relative to Saturn does not change appreciably during the time that the spacecraft transits the Hill's sphere of the flyby body, and secondly, that the bending angle associated with the flyby is relatively small. These assumptions are reasonably accurate for the simulated flybys of Enceladus, Tethys, Dione, and Rhea. However, recall that the flybys simulated in Figure 5.4 result from passes 100 km above the surface of each flyby body. For flybys with a close approach only 100 km above Titan, the bending angle will be relatively large for flyby velocities associated with all seven Titan-crossing orbits in Figure 5.1. Indeed, the trajectories plotted in Figure 5.2 result from simulations using the second highest apokrone altitude among those examined, and, thus, the second highest flyby velocity. Yet, the bending of trajectories immediately above Titan's surface in Figure 5.2 is clearly visible in the top plot, despite the relatively high flyby velocity. Consequently, the measure of V_∞ in the CR3BP, as described in this investigation, is not expected to agree

with the value calculated from Equation 2.63. Despite the discrepancy between the conic and CR3BP computations of ΔV_{eq}, a qualitative comparison between gravity-assist flybys in the patched conic and restricted three-body models still yields useful insight. From Figure 5.4, it is apparent that Titan can generally supply a ΔV_{eq} of at least ~1 km/s for each simulated flyby of the moon. The magnitude of ΔV_{eq} from Titan flybys is an order of magnitude larger than the effects of any other moon. However, the ΔV_{eq}'s from flybys of Tethys, Dione, and Rhea – flyby with values of ΔV_{eq} as large as 70-140 m/s – are still sufficiently large for practical use.

From an examination of flybys in terms of both patched conics, as well as simulations in the CR3BP, one last observation is useful for mission design applications. The magnitude of ΔV_{eq} that results from any flyby generally increases at a rate that is inversely proportional to flyby velocity and flyby altitude. This conclusion is in agreement with the conic calculation in Equation 2.63 and also follows from the simulations in Figures 5.3-5.4. One possible implication of the inverse relationship between ΔV_{eq} and both V_{∞} and r_c is that flybys of the smaller four moons may not be particularly beneficial to the design of a flyby sequence, unless the flyby velocity has been substantially reduced by either Titan flybys or a large propulsive maneuver. Even so, no *single* flyby of Titan or any of the other four moons yields a ΔV_{eq} of sufficient magnitude such that an arbitrarily sized initial orbit is immediately reduced to an energy level consistent with the orbit of Enceladus. Substantial reductions in orbital energy relative to Saturn, are only accomplished with sequences of flybys.

5.2 Designing Flyby Sequences in the Saturnian System

There has been a great deal of research in the design of orbital tours for planetary moon systems. Much past attention has focused on a tour of the Jovian system, with particular emphasis on Europa [32, 42-46]. However, discoveries at Saturn have recently

increased interest in Enceladus [4, 41, 47]. For previous applications, sequences of planetary moon flybys have been successfully designed by isolating a particular solution with patched conics and then correcting the trajectory in a full ephemeris model [32, 43, 44, 47-49]. This approach to planetary tour design has proven to be very robust and has been used to design the gravity-assist trajectories for several recent NASA spacecraft [32-37]. However, planetary tours proposed for future missions involve challenging new scenarios and dynamical environments that have not been previously exploited. To design trajectories that meet new complex requirements, mission designers seek non-intuitive trajectories and must explore broader regions in the solution space. Recent research has produced several examples of non-intuitive trajectories that involve repeated close encounters or orbits of several moons while requiring low propellant expenditure [42, 45, 46].

In generating new trajectories, mission design is generally approached from the same perspective, that is, identify reference solutions in lower-order dynamical models and then use corrections processes to remove position and velocity discontinuities in higher order dynamical models that may include additional non-gravitational perturbations [25, 45, 46, 53]. The goal of this method of mission design is for the final trajectory to retain the general characteristics of the trajectory designed in the simpler models. In an attempt to investigate flyby sequences from the multi-body perspective, a design method is developed that intentionally avoids patched conic assumptions, and instead focuses on computing flyby trajectories directly in the six-body model of the Saturnian system. The algorithm developed to design flyby sequences in this analysis is initiated with the minimum possible *a priori* knowledge of the expected characteristics of the flyby sequence solution. Thus, the mission designer is not biased toward known solutions or pre-determined flyby timing.

Various strategies for tour design have been pursued by a number of researchers. For example, Strange and Longuski [29] demonstrate a method of flyby sequence design in a patched conic model that identifies candidate flyby sequences based on an examination of the energetics involved in the flybys. A decided advantage of this approach is an immediate determination of a particular sequence of flybys that accomplishes some

desired change in orbital energy; that result is successfully obtained even though no initial ordering to the gravity-assist flybys is defined. However, the method by Strange and Longuski [29] does not offer phasing information so the feasibility of a particular candidate flyby sequence, given the configuration of the flyby bodies at some initial orbital epoch, is not immediately known. Alternatively, researchers including Lo and Anderson [25-27] have demonstrated sequences of gravity-assist flybys that transfer a spacecraft from some initial orbit, in resonance with the flyby body, to some alternate orbital resonance following each flyby. This method produces trajectories that periodically encounter the flyby body in a multi-body model – albeit a model that only includes the gravitational influence of Jupiter and a single moon – by targeting particular orbital resonances during each flyby. However, the method introduced by Lo and Anderson [25-27] requires prior knowledge of the precise spacecraft orbital resonances to be incorporated, both before and after a given flyby. The strategy developed in this investigation prioritizes two significant design issues: (i) this method only produces flyby sequences with feasible timing based on the initial configuration of the Saturnian moons, and (ii) knowledge of the orbit of the spacecraft prior to, or immediately following, a flyby is not required.

5.3 Design Algorithm for a Six-Body Flyby Sequence

The underlying logic of the flyby sequence design algorithm used in this investigation is relatively straightforward. Each iteration of the algorithm minimizes the closest approach distance that a spacecraft passes from some targeted flyby body. Although the initial shape and size of the spacecraft orbit are assumed to be fixed, it is possible to adjust the flyby altitude of the spacecraft by varying the initial argument of periapsis, ω, corresponding to the spacecraft orbit around Saturn. Most of the remaining details associated with the algorithm lie in its implementation.

In this investigation, the design algorithm for a flyby sequence is initialized with just three user inputs: (i) the shape and size of the initial spacecraft orbit around Saturn, (ii) the position of the spacecraft along its Saturnian orbit, and (iii) the initial position of

Saturn's moons along their orbits. Generally, the spacecraft is assumed to be located at perikrone at the beginning of each simulation, but this is not necessary. The trajectory design algorithm is independent of the initial orbital epoch of the Saturnian system; the algorithm produces solutions regardless of the initial positions of each moon.

The shape and size of the initial spacecraft orbit is specified via the perikrone and apokrone altitude of the orbit. With perikrone and apokrone altitude fixed, the orbital semi-major axis, eccentricity, and period are all uniquely defined. In addition, the orbit of the spacecraft is assumed to be coplanar with the orbits of the five moons. Since the spacecraft orbital inclination is zero, the ascending and describing nodes of the orbit are undefined. Thus, both the right ascension of the ascending node (RAAN) and argument of periapsis (ω) are undefined. For the purpose of this investigation, the inertial x-axis is selected as the reference direction from which the argument of periapsis (or argument of perikrone) is measured. The spacecraft is assumed to be located at perikrone at the beginning of each simulation, therefore, the true anomaly of the spacecraft along its orbit is defined to be zero. Note that, while the Keplarian elements associated with the initial spacecraft orbit are defined at the beginning of the flyby sequence design algorithm, these values are only used to define the initial conditions for the spacecraft; no additional conic assumptions are perpetuated throughout simulations in the six-body model.

Once the trajectory design algorithm is initialized with the shape and size of the spacecraft orbit, the orbital motion of the spacecraft is numerically propagated forward in time in the six-body model of the Saturnian system for approximately one orbital period. In general, the integrated spacecraft trajectory fails to encounter any of the five moons for some arbitrarily selected initial state. However, by varying the initial value of ω, the argument of periapsis, it is possible to rotate the orbit around Saturn such that the spacecraft is forced to cross the orbit of a targeted moon at precisely the moment that the moon is located at the intersection point. As an example, consider the two simulated trajectories plotted in the inertial frame in Figure 5.5. The simulation of both trajectories originates with the spacecraft located at perikrone of two orbits that are identical except for ω_o, the initial argument of periapsis. The orbits of each of the five moons appear as blue circles around Saturn in Figure 5.5. In the left-hand plot, the initial value of the

argument of periapsis is $\omega_o = 140^o$, while in the right-hand plot, $\omega_o = 120.82^o$. For both plots in Figure 5.5, Titan's orbital position is depicted 2.4 days after the beginning of the simulation; this is the length of time that is required for the spacecraft to reach the orbit of Titan. Along the orbit oriented such that $\omega_o = 140^o$, the spacecraft does not encounter Titan as it crosses the moon's orbit. However, by simply reorienting the orbit to $\omega_o = 120.82^o$, the spacecraft passes just above Titan's atmosphere and, as a result of the flyby, the apokrone distance of the spacecraft's orbit is noticeably reduced.

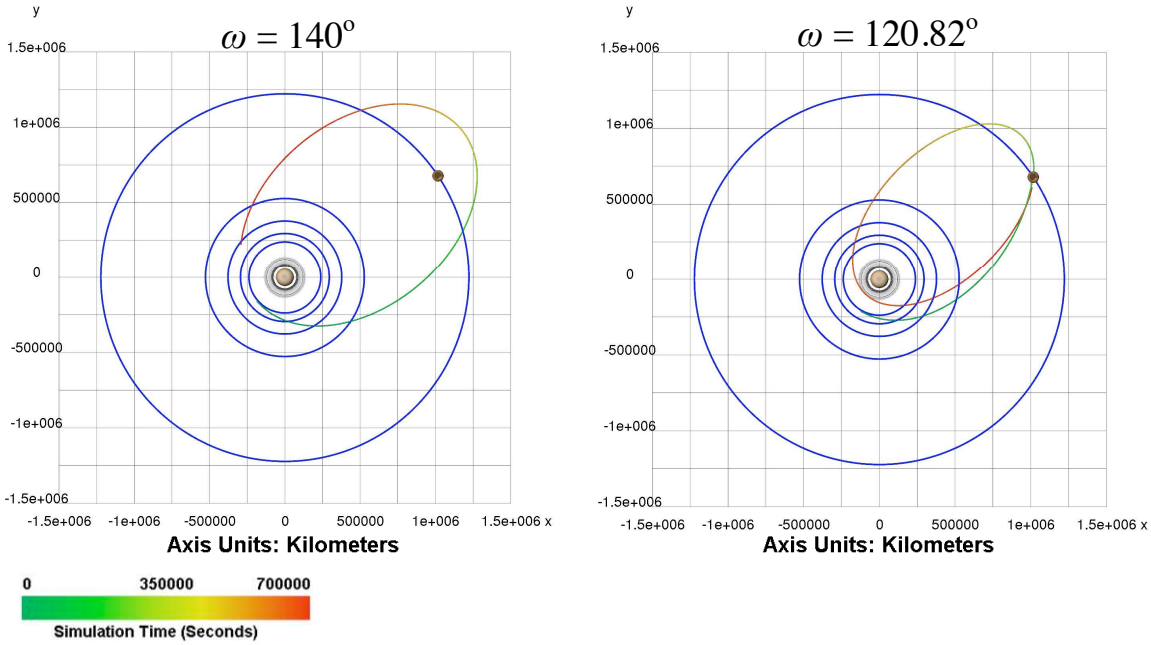

Figure 5.5 Two initial spacecraft trajectories for varying argument of periapsis values simulated in the six-body model of the Saturnian system.

In Figure 5.5, small changes in ω_o are used to isolate a *single* flyby of Titan. Once the first flyby is identified, it is also possible to target additional, future flybys of one or more of Saturn's moons by adjusting the flyby *altitude* of the first Titan flyby, such that the spacecraft orbit beyond the first gravity-assist flyby is then forced to encounter some additional target moon at a later point in the simulation. The altitude of each flyby is controlled by finely adjusting the initial value of argument of periapsis, ω_o. Theoretically, this logic can be extended to produce an infinite number of additional flybys. However, the sensitivity of the trajectory to small variations in ω_o renders long

sequences of gravity-assist flybys very difficult to compute through variations in ω_o. Although ω_o can be modified manually based on user intuition, it is more practical to automate the procedure. The process of using small variations in ω_o to target a flyby of some Saturnian moon can also be formulated as a local optimization problem.

5.3.1 Flyby Targeting Through Local Optimization

The identification of a single flyby trajectory by varying the initial argument of periapsis of the spacecraft orbit is formulated as a constrained optimization problem where the flyby altitude of the target moon constitutes the objective function to be minimized by variations in the one-dimensional design variable, ω_o. This optimization problem is formally stated as in Figure 5.6, where $r_c(x)$ is the objective function being

Optimization Problem Statement:

Minimize:

$$r_c(x)$$

Subject to:

$$g_j(x) = 1 - \frac{r_{c_j}(x)}{r_j} \le 0, \; j = 1,2,3,4,5$$

$$g_6(x) = r_{a_2}(x) - r_{a_1}(x) \le 0$$

$$0^\circ \le x \le 360^\circ$$

Where:

$$x = \omega_o$$

Figure 5.6 Formulation of the optimization problem statement used to find flyby trajectories of a Saturnian moon in the six-body dynamical model.

minimized. The objective function, $r_c(x)$, returns the altitude of the spacecraft at the point of closest approach to the targeted flyby moon, as a function of the sole design variable, x. The design variables, x, is a scalar equal to the initial argument of periapsis, ω_o. In targeting the initial flyby in a sequence of gravity-assist flybys, x is permitted to

be any angular value within the range: $0^o < x < 360^o$. The objective function, $r_c(x)$, cannot be expressed as a closed form algebraic function of the design variable, x, because the design variable is simply a result of the parameterization of the initial spacecraft orbital state, and the value of the objective function, $r_c(x)$, is evaluated as the minimum distance to the flyby body along a numerically integrated spacecraft trajectory.

This relatively simple optimization problem involves the minimization of an objective function with a one-dimensional design space. However, the optimization will converge to collision trajectories with the flyby moons unless constraints are introduced to maintain feasibility in the physical Saturnian system. The inequality constraints that appear in Figure 5.6 serve two purposes: first, the constraints prevent collisions with each of the five moons throughout the simulation, and second, an additional inequality constraint ensures that the flyby passes on the correct side of the target body to produce a reduction in the apokrone altitude of the spacecraft orbit around Saturn. As is common in the formulation of optimization problems, the inequality constraints are only violated if the value of $g_i(x)$ exceeds zero when evaluated at x. The first five constraints, those labeled $g_j(x)$ for $j \in \{1,2,3,4,5\}$, constrain $r_{c_j}(x)$, the close approach distance to moon "j," to be greater than the minimum feasible flyby distance from that moon: r_j (Table 5.1). In this formulation $j \in \{1,2,3,4,5\}$, and these five integers correspond to the five moons in the dynamical model: Enceladus, Tethys, Dione, Rhea, and Titan. The sixth inequality constraint, the constraint labeled $g_6(x)$, ensures that a flyby can only result in

Table 5.1 Physical properties of the Saturnian moons used in the optimization constraint formulation.

	"j" Value	Radius of Moon (km)	Min. Feasible Flyby Altitude (km)	r_j Value (km)	$0.8 \cdot r_{Hill_j}$
Enceladus	1	256.3	50	306.3	760.4
Tethys	2	529.8	50	579.8	1681.9
Dione	3	560	50	610	2607.0
Rhea	4	764	50	814	4664.9
Titan	5	2575	900	3475	41938.8

a reduction in the spacecraft orbital apokrone altitude and, thus, its orbital energy. The constraint $g_6(x)$ is calculated based on state vectors obtained from the integrated spacecraft trajectory, and the constraint is only violated if $r_{a_1}(x) \geq r_{a_2}(x)$. The variable, $r_{a_1}(x)$, is the instantaneous apokrone distance of the spacecraft's Saturnian orbit calculated just prior to the closest approach of the flyby body, and $r_{a_2}(x)$ is the instantaneous apokrone distance calculated from the state vector immediately after the flyby. The apokrone distances, $r_{a_1}(x)$ and $r_{a_2}(x)$, are computed solely to determine whether the flyby results in a reduction in orbital energy. Despite the unequal physical radii of the five moons used for gravity-assist flybys, the first five constraints are scaled to possess equal weights. However, the sixth constraint is not scaled because numerous trials demonstrate that convergence is achieved more quickly when violations of $g_6(x)$ are allowed greater weight than the five collision constraints.

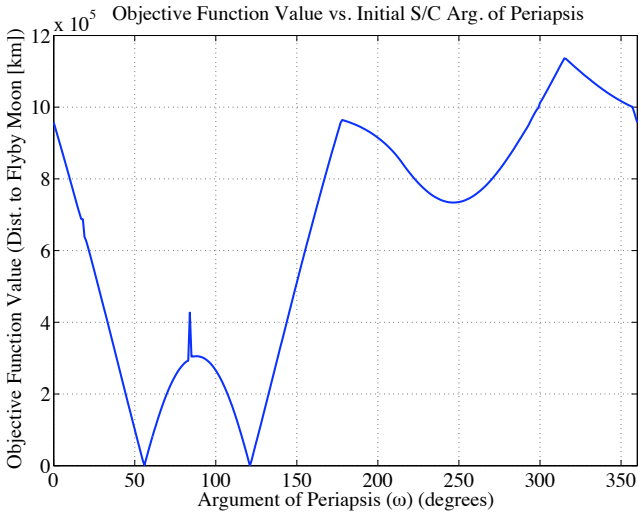

Figure 5.7 A grid search of the design variable domain associated with the flyby trajectory objective function for a single Titan flyby.

Although the objective function in this algorithm cannot be expressed as a simple algebraic function of the design variable, gradient information is used to speed the convergence of a local optimization routine. A grid search of the design variable domain associated with the objective function for a single Titan flyby appears in Figure 5.7. The

design variable domain mapping in Figure 5.7 corresponds to an initial spacecraft orbit with r_p = 244,455.28 km and r_a=1,527,845.5 km. An examination of Figure 5.7 reveals that there are two local minima with an objective function value near zero: $\omega_o = 56^o$ and $\omega_o = 121^o$. Both of these values are valid designs for flybys of Titan; one local minimum results in an outbound flyby and the other is an inbound flyby of the targeted moon. In addition to the two local minima associated with Titan flybys, there are several additional features in Figure 5.7 that are notable. Apart from the two values of ω_o associated with Titan flybys, there is also a local minimum near $\omega_o \approx 245^o$ that is *not* associated with a flyby, and as such, this local minimum is an undesirable solution. However, user intuition can generally be used to prevent convergence on a local minima that is not associated with a flyby. An additional feature that is visible in Figure 5.7 is a sharp spike near $\omega_o \approx 85^o$. This feature results from a close flyby with one of the four moons in the six-body model of the Saturnian system other than Titan. If the design variable domain is mapped at an even higher resolution than appears in Figure 5.7, additional features resulting from flybys of all of the moons in the six-body model are evident. In practice, the spikes that result from flybys of additional moons are associated with violations of the $g_1(x) - g_5(x)$ constraints in Figure 5.6. Therefore, these undesirable regions are not part of the design space.

A number of optimization algorithms can potentially be used to solve the problem formulated in Figure 5.6. The design space of the objective function in Figure 5.7 possesses relatively few local minima, and the two local minima associated with the Titan flybys have a width of convergence that is roughly equal to half the design variable domain. For this reason, the optimization algorithm selected for application in isolating flyby trajectories uses gradient information to update the optimization search direction. It is emphasized that there are *many* gradient-based constrained optimization algorithms, and some are better suited to this problem than others. However, one common and robust nonlinear programming algorithm that is available is Sequential Quadratic Programming (SQP). The SQP routine is a quasi-Newton direct method of minimizing a continuous nonlinear objective function by solving a simpler quadratic programming sub-problem. In essence, an SQP optimizer uses both numerical gradients and a numerical

approximation of the Hessian matrix of the Lagrangian function to solve a Quadratic Programming (QP) search direction sub-problem during each iteration of the SQP routine [54]. The SQP procedure is applied to the optimization problem in this investigation because the constraints are nonlinear functions of the design variable, ω_o. However, it should be noted that SQP is better-suited to problems of substantially more complexity than the minimization of a function with a one-dimensional design space. A simpler, bounded minimization routine could potentially be used to identify flyby trajectories. However, such a method is not used here because of the complexity involved in evaluating the $g_1(x)$ - $g_5(x)$ constraints. While a bounded minimization technique might require separate numeric simulations of the spacecraft motion to evaluate the constraint values, the implementation of the SQP routine accommodates the nonlinear bounds without the necessity for any trajectory simulations beyond the objective function evaluations already included. Although SQP optimization is typically used for problems of greater complexity than the trajectory design problem in this investigation, the SQP routine is still very effective in solving the optimization problem as formulated in Figure 5.6. The SQP algorithm is implemented using the "fmincon" routine available in MATLAB®.

5.3.2 Application of SQP Optimization to Flyby Trajectory Design

To illustrate the process involved in the trajectory design algorithm, the SQP routine is used to determine the value of ω_o that produces a flyby of Titan for an initial spacecraft orbit sized such that r_p = 244,455.28 km and r_a = 1,527,845.5 km. The input to the SQP routine included an arbitrarily chosen initial guess of ω_o = 180°, a design variable value that does not yield a pass close to Titan. The SQP routine converges on a trajectory that passes within 0.5 mm of the 3475 km minimum flyby altitude constraint for Titan, though this level of accuracy greatly exceeds the fidelity of the model used in simulating the physical Saturnian system. The optimal design, x^*, that results in a Titan flyby is x^*=120.819487308821°. Convergence onto the Titan flyby trajectory in Figure 5.8

requires 6 iterations of the SQP routine, involving 15 objective function evaluations, and totals less than five seconds of computation time on a desktop computer. This result could be accomplished with a simpler shooting algorithm, but this is but the first encounter in a longer flyby sequence.

It is not surprising that the flyby trajectory identified by the optimization routine is observed to skim the edge of Titan's 900 km thick atmosphere, depicted in Figure 5.8 as a transparent sphere of proper thickness relative to Titan's surface. The trajectory in Figure 5.8 is plotted in the Titan-centered Saturn-Titan rotating frame. As the flyby trajectory passes Titan on the positive y side of the x-axis, the trajectory passes *ahead* of Titan in its orbital motion around Saturn; the gravity-assist flyby results in a reduction in the apokrone distance of the spacecraft orbit around Saturn [32]. All six of the constraints are satisfied, and the constraint preventing a Titan collision is active, that is, $g_5(x^*) = 0$.

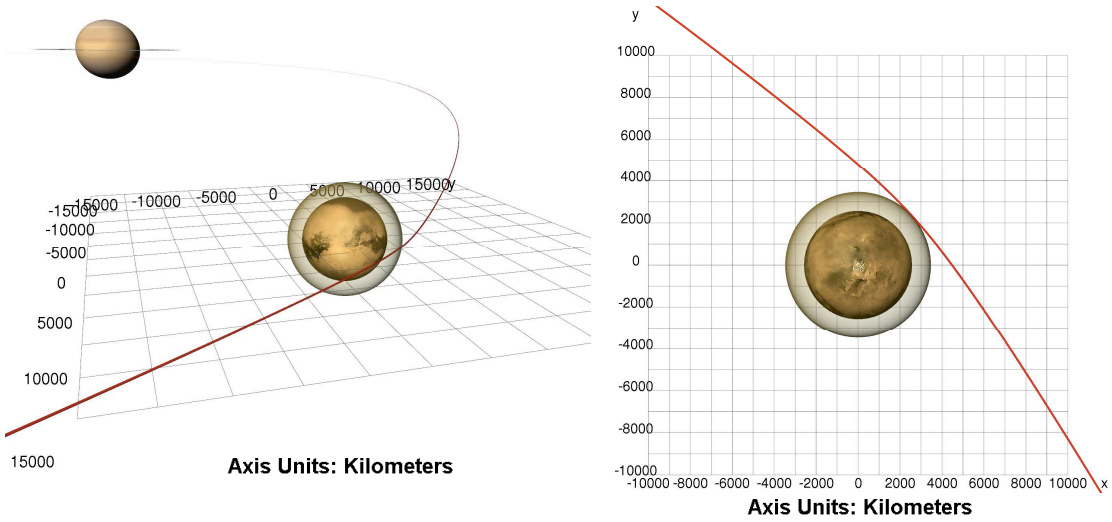

Figure 5.8 Two views of a single low-altitude Titan flyby identified using the SQP optimization algorithm.

The flyby trajectory in Figure 5.8 is optimized to pass by Titan at a height exactly equal to the minimum flyby altitude that remains feasible and the trajectory thus receives the largest possible reduction in apokrone distance. Following the Titan flyby, if the trajectory is simulated for several additional revolutions around Saturn, it is possible that the trajectory will naturally encounter additional Saturnian satellites, however, in general

no untargeted future flybys occur. Although the Titan flyby in Figure 5.8 is optimized to achieve the maximum feasible reduction in orbital energy, to build a sequence of flybys it is necessary to sacrifice the optimality of the first flyby to ensure that the trajectory of the spacecraft following the first flyby can be targeted to encounter another flyby body at a later simulation time.

A close flyby of a Saturnian moon reshapes the orbit of the spacecraft passing near the moon. However, the trajectory of the spacecraft following the flyby varies depending on the altitude that the spacecraft passes above the flyby body. By carefully modifying the altitude of one gravity-assist flyby it is possible to target additional future flybys of along the path of the spacecraft. Following the identification of a single flyby trajectory of some Saturnian moon, additional flybys are targeted by small variations in the value of x^*. Recall that x^* is equal to ω_o, the initial argument of periapsis of the spacecraft orbit. Therefore, small variations made in ω_o prior to the first flyby allow fine adjustments to the flyby altitude of the first flyby and, subsequently, flybys of additional moons that are targeted downstream.

To target a second flyby, the flyby sequence design algorithm must preserve the gravity-assist effects of the first flyby while adjusting the altitude of the first flyby to target the second flyby. Since the design of the overall flyby sequence is still expected to pass close to the first flyby target, regardless of any later flybys, the bounds on the design variable, x, are redefined for the second flyby to force the spacecraft to pass near the vicinity of the first flyby body along its path toward later flyby targets. As an example of the bounds on the design variable used to preserve the first flyby, consider the two trajectories depicted in Figure 5.9. In Figure 5.9, the red trajectory is the same optimized trajectory from Figure 5.8 that passes immediately above Titan's atmosphere. This red curve represents the closest feasible flyby of Titan and results from a design variable equal to ω_{c_1}, where "c" denotes that the design results in the "closest" feasible flyby of flyby target number "1". The blue trajectory in Figure 5.9 results from a design variable value ω_{f_1}, where the "f" indicates that the design variable ω_{f_1} results in a flyby "further" from the targeted flyby body number "1". Thus, ω_{f_1} is a trajectory that is optimized by

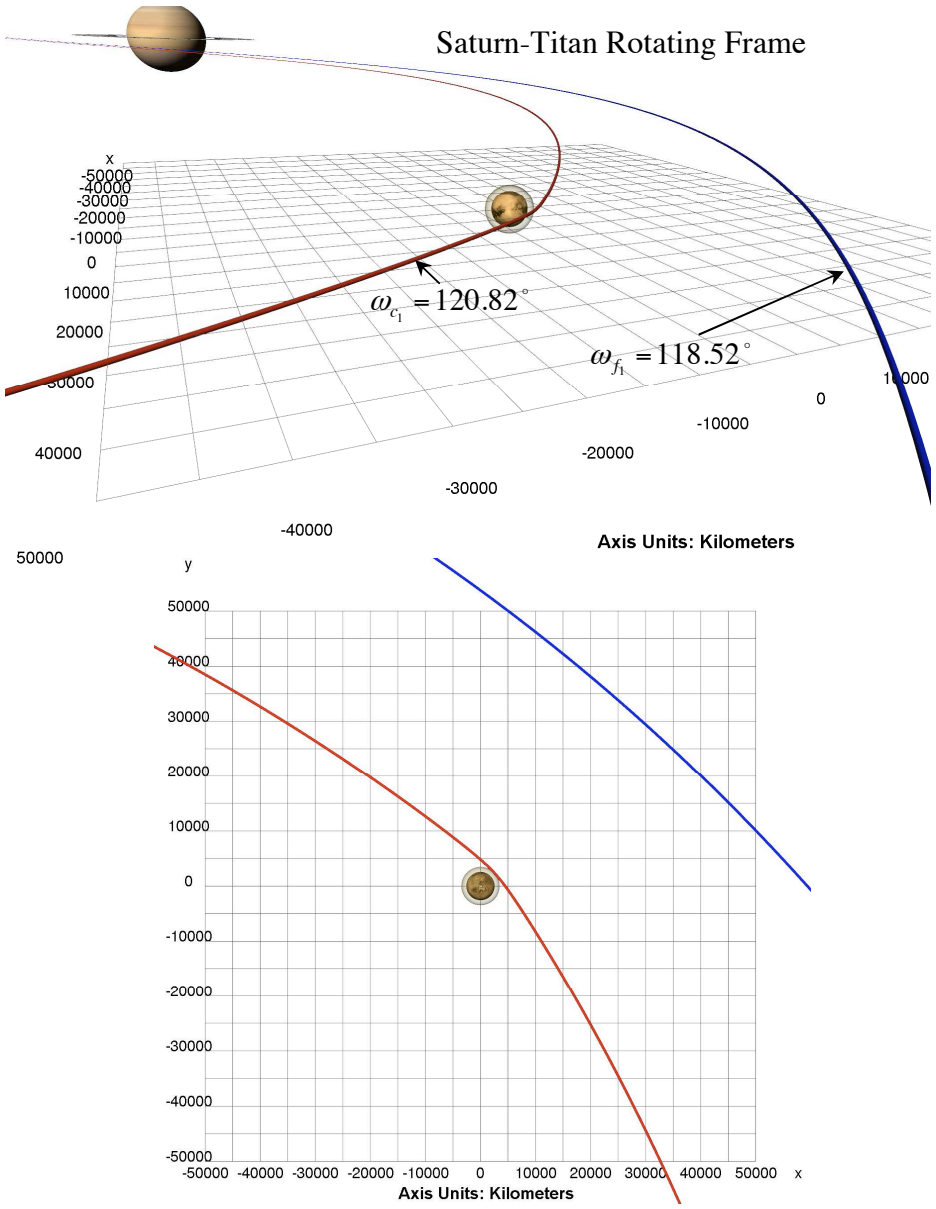

Figure 5.9 Two Titan flybys identified via SQP plotted in the Saturn-Titan rotating frame; (i) one at the minimum feasible flyby altitude (red), and (ii) one at a distance 0.8 times Titan's Hill's sphere radius (blue).

the SQP routine to pass at a distance from the moon equal to eight tenths (i.e., 0.8) of Titan's Hill's sphere radius. The more distant flyby in Figure 5.9 defines an additional bound for the design variable, x. A trajectory with an initial design value between ω_{c_1} and ω_{f_1} always passes within Titan's Hill's sphere regardless of which future flybys are included in the gravity-assist sequence. The more distant flyby in Figure 5.9 is

determined by modifying the constraints $g_1(x)$ - $g_5(x)$ such that r_j, the minimum feasible flyby altitude (Figure 5.6), is replaced with $0.8 \cdot r_{Hills_j}$, where r_{Hills_j} is the Hill's sphere radius of moon "j" (Equation 2.64). The spacecraft is constrained to pass within $0.8 \cdot r_{Hills_j}$ because this ensures that some appreciable gravity-assist effect from the flyby is preserved, however, 80% is an arbitrary value and can be replaced with any reasonable distance for each moon. The dimensional values corresponding to $0.8 \cdot r_{Hills_j}$ for each moon is included in Table 5.1.

Targeting of a flyby of an additional moon is accomplished by increasing the simulation duration to allow the spacecraft sufficient time to encounter the future target, then minimizing the closest approach distance to the desired flyby body at all simulation times *following* the first flyby. This additional targeting is subject to the more restrictive bounds on the design variable. External to the SQP routine, the design variable bounds for the second flyby are redefined as: $\min(\omega_{c_1}, \omega_{f_1}) \le x \le \max(\omega_{c_1}, \omega_{f_1})$. Using the new bounds on the design variable, the SQP algorithm targets an additional flyby of some Saturnian moon, while ensuring that the flyby of the first moon still occurs. As an example, the flyby sequence design algorithm determines a flyby of Titan followed by a flyby of Dione. Using the initial spacecraft orbit from Figures 5.8-5.9, the SQP optimization first computes the two flyby trajectories in Figure 5.9 that supply the design variable bounds for the first Titan flyby: ω_{c_1} =120.819487308821° and ω_{f_1} =118.522004684514°. Using the bounds, $\omega_{f_1} \le x \le \omega_{c_1}$, the optimization routine is directed to minimize the closest approach distance to Dione following the initial Titan encounter. Following the determination of the two Titan flybys, seven iterations and 16 objective function evaluations are required to identify the optimal design that achieves the Dione flyby: ω_{c_2} = 120.378725978734°. The trajectory that accomplishes the double flyby sequence is plotted in Figure 5.10. A Titan encounter occurs 2.4 days into the simulation, then after 2.5 revolutions around Saturn over the following 23 days, the spacecraft passes 50 km above the surface of Dione. As a result of the two flybys, the

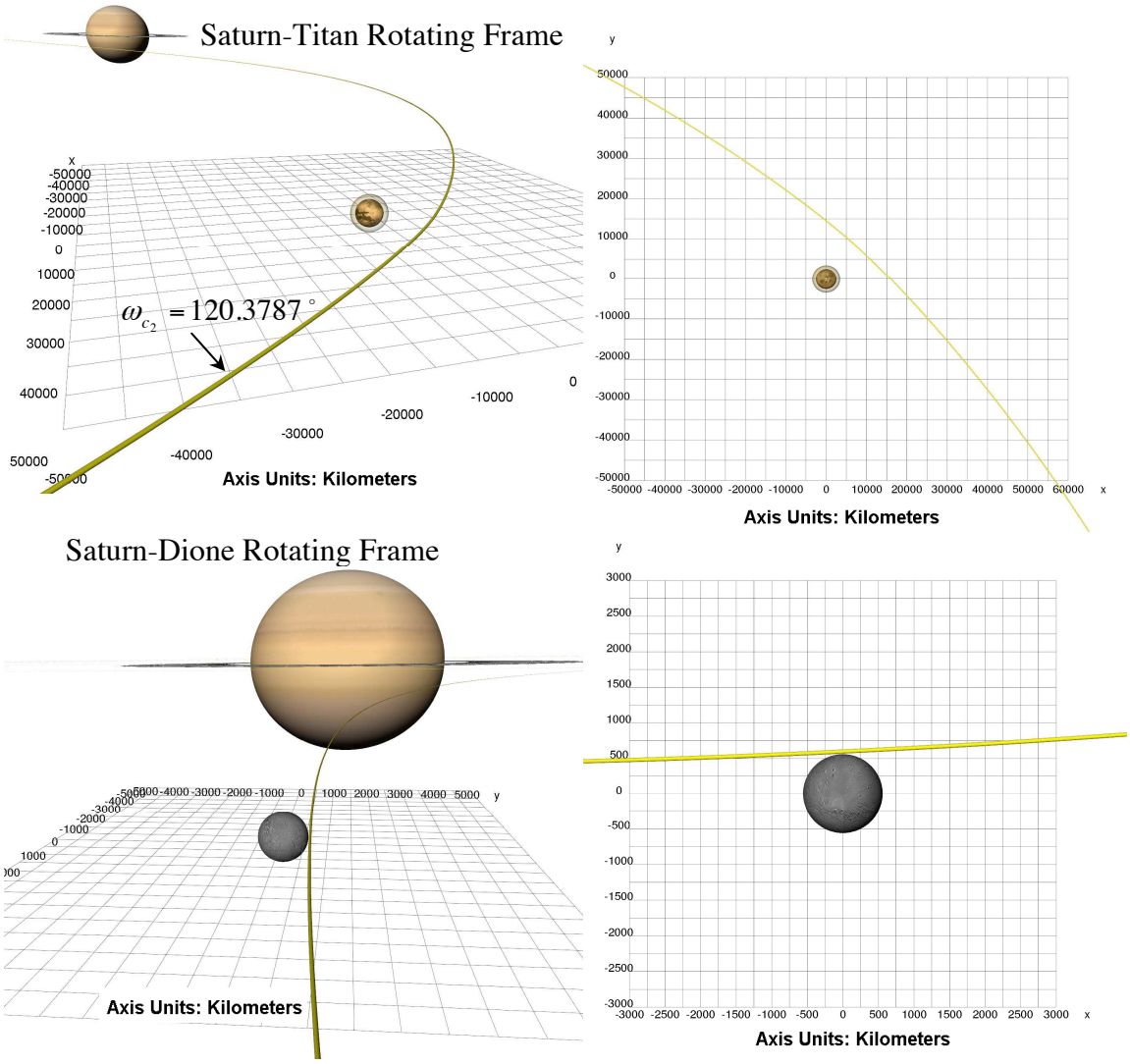

Figure 5.10 A Titan-Dione double flyby trajectory designed using SQP optimization.

apokrone distance of the spacecraft orbit is reduced by over 80,000 km, though only ~5% of that change results from the Dione flyby. Note that, as expected, the optimal design identified by the SQP routine, that is, ω_{c_2} =120.378725978734°, falls within the bounds placed on the design variable, *x*, and the close proximity of the first Titan flyby is preserved even as the second flyby is targeted.

5.3.3 Details of the Flyby Sequence Design Algorithm

In the previous section, the flyby sequence design algorithm is demonstrated to identify a single trajectory that encounters both Titan and Dione. However, Titan and Dione only serve as an example. The actual sequence of moons can be selected based on user intuition, mission design constraints, or simply as targets of opportunity. Although the Titan-Dione flyby trajectory in Figure 5.10 extends only through the second flyby, the same steps are implemented iteratively to produce a flyby sequence with an arbitrary number of close encounters with various Saturnian moons. Successive flybys of the same Saturnian moon are valid and possible outcomes from the application of the design algorithm.

To aid in the comprehension of the trajectory design algorithm, a flowchart representation of the algorithm is depicted in Figure 5.11. The ultimate objective of the trajectory design algorithm is to obtain ω_{c_i}, the initial instantaneous value of the argument of periapsis that results in the flyby sequence achieving all of the "i" targeted flybys. Each iteration of the main loop of the trajectory design algorithm in Figure 5.11 identifies both a nearby and distant flyby of the targeted Saturnian moon. In theory, the algorithm terminates when no additional flybys are desired although, in practice, the algorithm terminates when the optimization routine encounters numerical sensitivity issues or otherwise fails to converge on a trajectory that accomplishes the user-defined sequence of flyby.

In the implementation of the algorithm, an alternate formulation of the sixth optimization constraint, $g_6(x)$, may prove useful. In the problem statement in Figure 5.6, the sixth constraint is calculated simply as the difference between the apokrone altitude of the spacecraft orbit prior to the flyby and the apokrone altitude following the

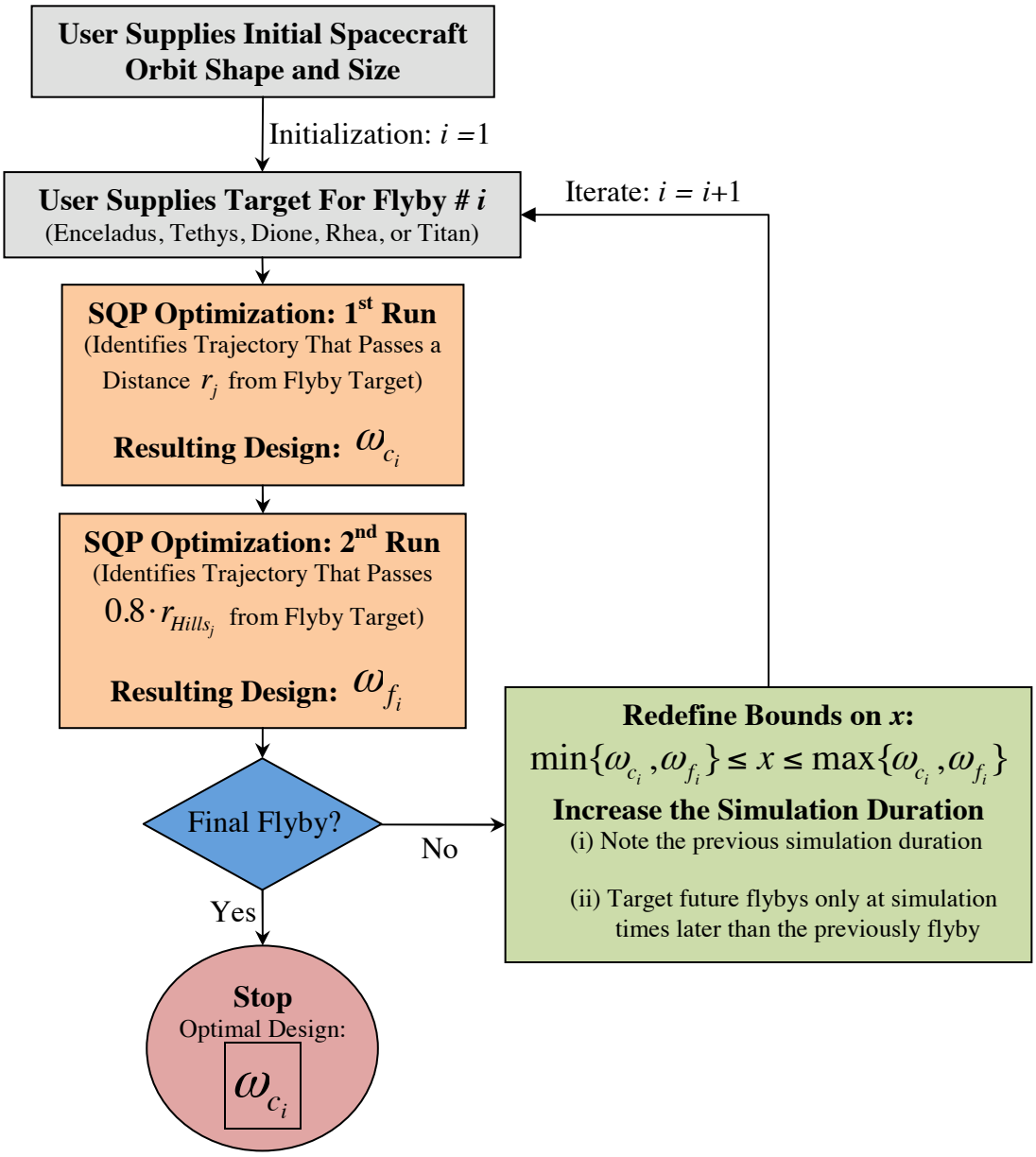

Figure 5.11 Flyby sequence design algorithm introduced in this analysis.

flyby, $g_6(x) = r_{a_2}(x) - r_{a_1}(x) \le 0$. The sixth constraint ensures that the spacecraft passes on the correct side of the flyby target so that the flyby results in a reduction in the spacecraft orbital energy. Since it is already known that flybys ahead of the target moon produce the desired result, the sixth constraint could also be formulated as follows,

$$g_6(x) = -\left[\left(\hat{R}_j \times \hat{R}_{jS}\right) \bullet \hat{z}\right] \leq 0\,, \tag{5.1}$$

where $\hat{R}_j$ and $\hat{R}_{jS}$ are unit vectors in the direction of vectors $\bar{R}_j$ and $\bar{R}_{jS}$, as defined in Figure 5.12. Both $\hat{R}_j$ and $\hat{R}_{jS}$ are calculated at the moment of closest approach to the flyby body. Recall that flyby trajectories designed in the six-body model of the Saturnian system are located entirely within the inertial *xy*-plane; this is the plane of the orbital motion of the five Saturnian moons. Since the orbits of both the spacecraft and the flyby

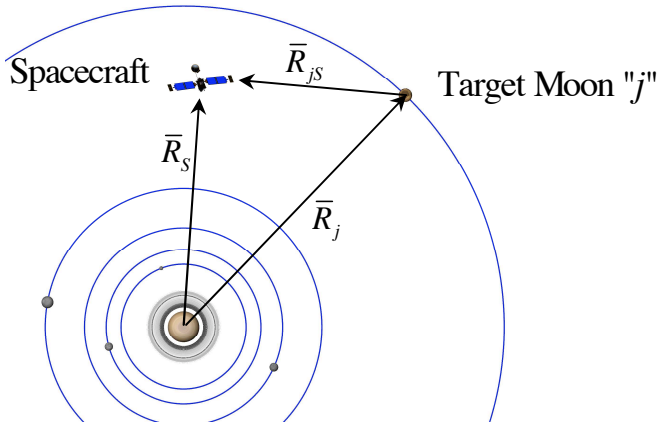

Figure 5.12 Vectors quantities used in the alternate formulation of the optimization constraint, $g_6(x)$.

moon are coplanar, the cross product $\hat{R}_j \times \hat{R}_{jS}$ results in a vector with a positive *z* component when the spacecraft passes ahead of the flyby moon at closest approach, and a negative *z* component when the spacecraft passes behind the target moon. The constraint in Equation 5.1 effectively performs a check of the sign of the *z*-component of the cross product, $\hat{R}_j \times \hat{R}_{jS}$. This alternate formulation of the sixth optimization constraint is used interchangeably with the constraint that appears in Figure 5.6. However, the formulation of the constraint in Figure 5.6 tends to achieve faster convergence, so this constraint formulation is preferred, though both constraint formulations are used in the design of flyby sequences.

5.3.4 Sample Sequence of Four Gravity-Assist Flybys

To demonstrate the capabilities of the flyby sequence design algorithm, a number of example flyby sequences are designed. Because of Titan's immense size, it is the most desirable target for gravity-assist flybys, however, a flyby sequence using only the remaining four Saturnian moons is designed as an illustration of the appearance of trajectories in the vicinity of these moons. Ultimately, to reach an orbit with apokrone below the radius of Titan's orbit, gravity-assist flybys using the other moons are required.

To ensure that flybys of Enceladus, Tethys, Dione, and Rhea are all feasible along the assumed initial orbit of the spacecraft, the initial orbit is selected with dimensions corresponding to: r_p = 244455.28 km and r_a = 1527845.5 km. The flyby sequence is selected as: Dione-Tethys-Rhea-Dione, and each of these flybys are plotted in Figure 5.13. The computational progress of the trajectory design algorithm is recorded in Table 5.2. The first three flybys are successfully identified by the algorithm within 60 seconds,

Table 5.2 Progress of flyby sequence design algorithm during demonstration trajectory design.

Flyby Body	Time to Convergence (s)	Minimum Distance to Moon on Final Trajectory (km)	Design Variable ω_o For the Optimal Design (deg)
Dione	7.3	2595.8	83.885566429415
Tethys	31.0	1653.7	83.5823891135278
Rhea	54.0	1488.7	83.5839437111511
Dione	77.8	17,860	83.5839262770679
Enceladus (Unintentional)	-	5489.2	-

and although the optimizer converges on a solution for the second Dione flyby, it is distant. Although Enceladus is not specifically targeted during this short flyby sequence, two untargeted Enceladus encounters do occur, though neither passes sufficiently close to Enceladus to receive any substantial gravity-assist effects. The flybys of Dione, Tethys, and Rhea are plotted in Figure 5.13 along with a plot showing the two Enceladus encounters, and an inertial view of the entire spacecraft trajectory. The flyby sequence

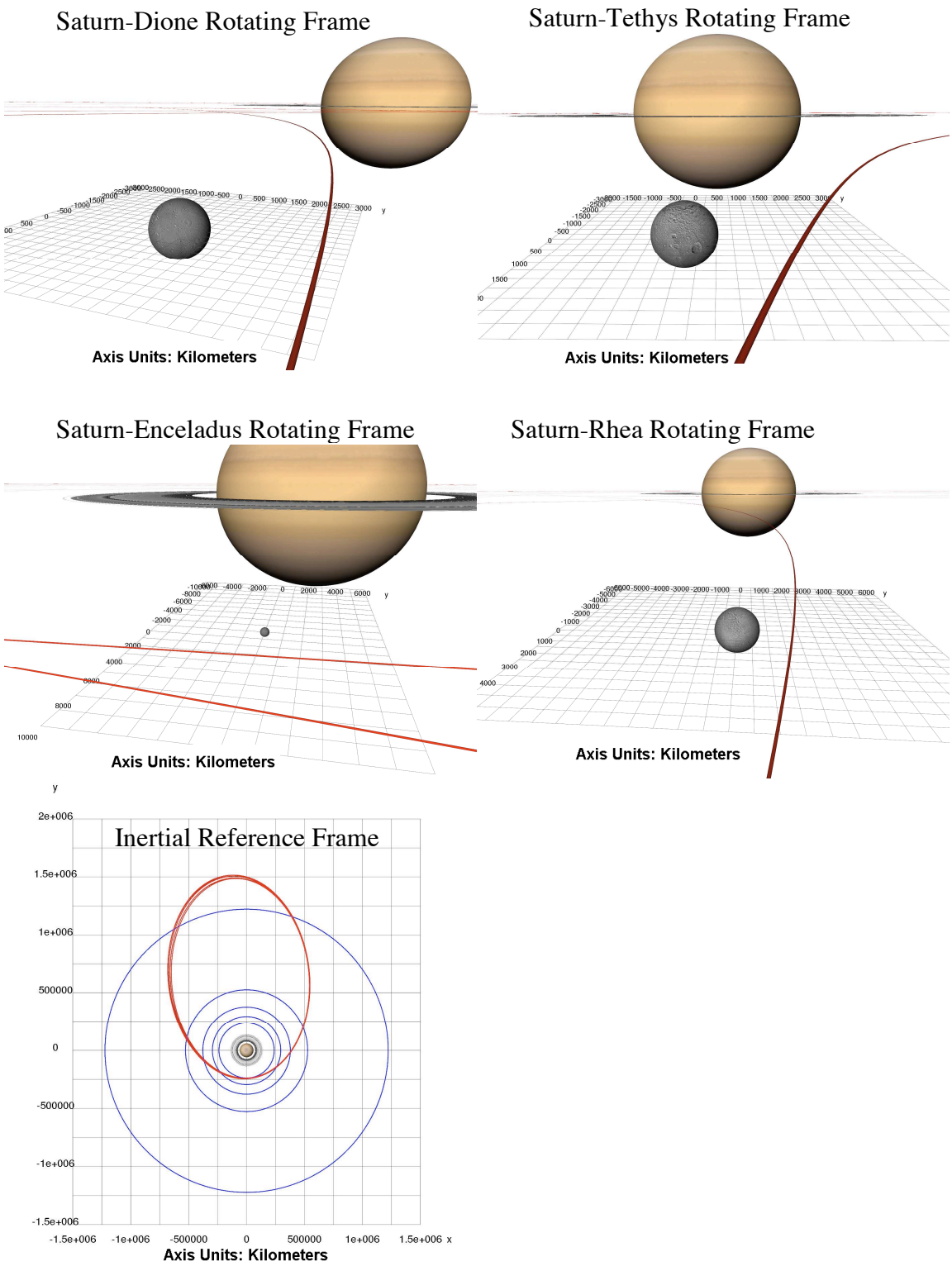

Figure 5.13 Rotating frame and inertial views of a sequence of four targeted gravity-assist flybys in the order: Dione, Tethys, Rhea, Dione.

decreases the apokrone altitude of the spacecraft's Saturnian orbit by 37,250 km during the 124-day simulation, though a further reduction of ~1,200,000 km is necessary to circularize the orbit to match the size of Enceladus' orbit. Clearly then, a sequence of flybys using only the four interior Saturnian moons requires many flybys to significantly reshape the orbit of the spacecraft. However, a parameter study to consider the trade-offs between the number of flybys and the size of additional maneuvers would yield more insight into the problem.

The trajectory in Figure 5.13 is an example of the sensitivity of the problem to small variations in the initial value of ω_o. Note that in Table 5.2, each gravity-assist flyby is achieved by varying ω_o at a level two orders of magnitude smaller than the previous flyby. Thus the values of ω_o in Table 5.2 demonstrate that numerical sensitivity may ultimately limit the length of the flyby sequences that can be designed using this method.

5.3.5 Flyby Sequence to Reduce Orbital Energy

In this investigation, the objective of a sequence of gravity-assist flybys is relatively well defined; the flybys should produce a net decrease in orbital energy relative to Saturn via a reduction in apokrone height, eccentricity, or some other characteristic of the initial spacecraft orbit. Using gravity-assist flybys accomplishes energy reductions without using additional onboard propellant.

The conic model is useful to estimate the change in the spacecraft orbit around Saturn that is necessary to approach Enceladus' energy level. If the orbit of Cassini is used for guidance, it is expected that a spacecraft in orbit around Saturn may initially travel along an orbit defined with an apokrone altitude in excess of 12,500,000 km and a perikrone distance of ~240,000 km (a size comparable to Enceladus' orbit around Saturn) [4]. Along a conic orbit of this size, the spacecraft velocity is ~18.8 km/s as it passes perikrone. At the same distance from Saturn, Enceladus travels at a velocity of ~12.6 km/s relative to the planet. To enter Enceladus orbit, the difference in relative velocity

between the spacecraft and Enceladus must be reduced to zero. Thus, a ΔV of 6.2 km/s, applied when the spacecraft is near perikrone, can circularize the spacecraft's orbit to match the orbit of Enceladus. In practice, a velocity change of 6.2 km/s is exceptionally large for spacecraft using chemical propulsion. A ΔV of this magnitude exceeds the propulsive capabilities at the destination planet of every chemical propelled interplanetary probe launched to date. Although the orbits with an apokrone distance of 12,500,000 km are beyond the scope of this investigation, repeated flybys of Titan can be used to reduce apokrone to the initial value of ~7,300,000 km used in this analysis.

The flyby sequences introduced previously in Figures 5.10 and 5.13 illustrate both the implementation and sensitivity of the flyby sequence design algorithm, yet neither of the trajectories in the previous two examples result in a substantial decrease in orbital energy relative to Saturn. However, the trajectory design algorithm can be successfully applied to the problem of reducing the orbital energy of a spacecraft to a level that more closely approaches the energy level of Enceladus' orbit. To demonstrate a more effective use of the flyby sequence design algorithm to the Saturnian system, the algorithm is applied to reduce the orbital energy of a more practical initial spacecraft orbit.

Assume that a spacecraft is initially in an orbit around Saturn with a perikrone distance of ~1,100,000 km (90% of Titan's semi-major axis) and an apokrone of ~7,300,000 km (six times larger than Titan's orbit). Using the Cassini mission [51] and the Enceladus Flagship Mission Concept Study [4] as baselines for spacecraft performance upon arrival at Saturn, it is feasible for a chemically-propelled spacecraft to achieve capture into an orbit of this size using two large propulsive maneuvers; one at the closest approach to Saturn, used to insert into an orbit with an apokrone of ~7,300,000 km, and a second maneuver peformed at apokrone to raise perikrone from a meager ~200,000 km to a distance of ~1,100,000 km from Saturn. Similar maneuvers are required to achieve Saturnian orbit regardless of any subsequent tour of the Saturnian system.

The perikrone altitude of the initial spacecraft orbit, $r_p \approx 1{,}100{,}000$ km, exceeds the orbital radius of every one of the moons incorporated in the six-body model of the Saturnian system, with the exception of Titan (Table 4.3). Titan is the only moon

accessible for use in gravity-assist flybys along the initial spacecraft orbit, and is therefore the first targeted flyby body. The simulations to quantify the equivalent ΔV resulting from flybys of each moon (Figures 5.3 and 5.4) demonstrate that gravity-assist flybys of Titan result in ΔV_{eq} values that are much larger in magnitude than flybys of Enceladus, Tethys, Dione, or Rhea. Due to the larger ΔV_{eq} values associated with Titan flybys, the gravity of this moon is used repeatedly in the flyby sequence until the perikrone of the final spacecraft orbit is approximately the same distance from Saturn as the orbit of Enceladus.

A sequence of six Titan gravity-assist flybys followed by one Dione flyby is plotted in Figures 5.14 and 5.15. The flyby sequence is divided between the two figures to aid in the visibility of trajectory details. The flyby sequence could be accomplished along a single continuous trajectory, however, the trajectories that appear in Figures 5.14 and 5.15 result from two separate applications of the trajectory design algorithm. First, the algorithm is used to produce the first two Titan flybys in Figure 5.14. Secondly, the algorithm is restarted from an initial spacecraft orbit that closely matches the size of the final spacecraft orbit in Figure 5.14 to determine the remaining four Titan flybys and sole Dione flyby. The flyby sequence in Figure 5.14 begins on a spacecraft orbit with dimensions: r_p = 1100048.76 km and r_a= 7,333,658.4 km. The flyby sequence design algorithm yields the optimal design for the two flybys in Figure 5.14 with a final value of the design variable equal to ω_o = 38.4281193908731°. The time-of-flight between the two flybys in Figure 5.14 is 168 days and, as a consequence of the ΔV_{eq} induced by each Titan flyby, the apokrone distance of the spacecraft's orbit decreases by ~5,800,000 km and the perikrone distance decreases by ~610,000 km.

An additional flyby sequence is targeted to produce a trajectory incorporating the third through sixth Titan flybys and the sole flyby of Dione; the result appears in Figure 5.15. The trajectory in Figure 5.15 including the third through seventh flybys, and originates in an initial orbit that matches the approximate size of the spacecraft's orbit following the two Titan flybys in Figure 5.14. The precise dimensions of the initial

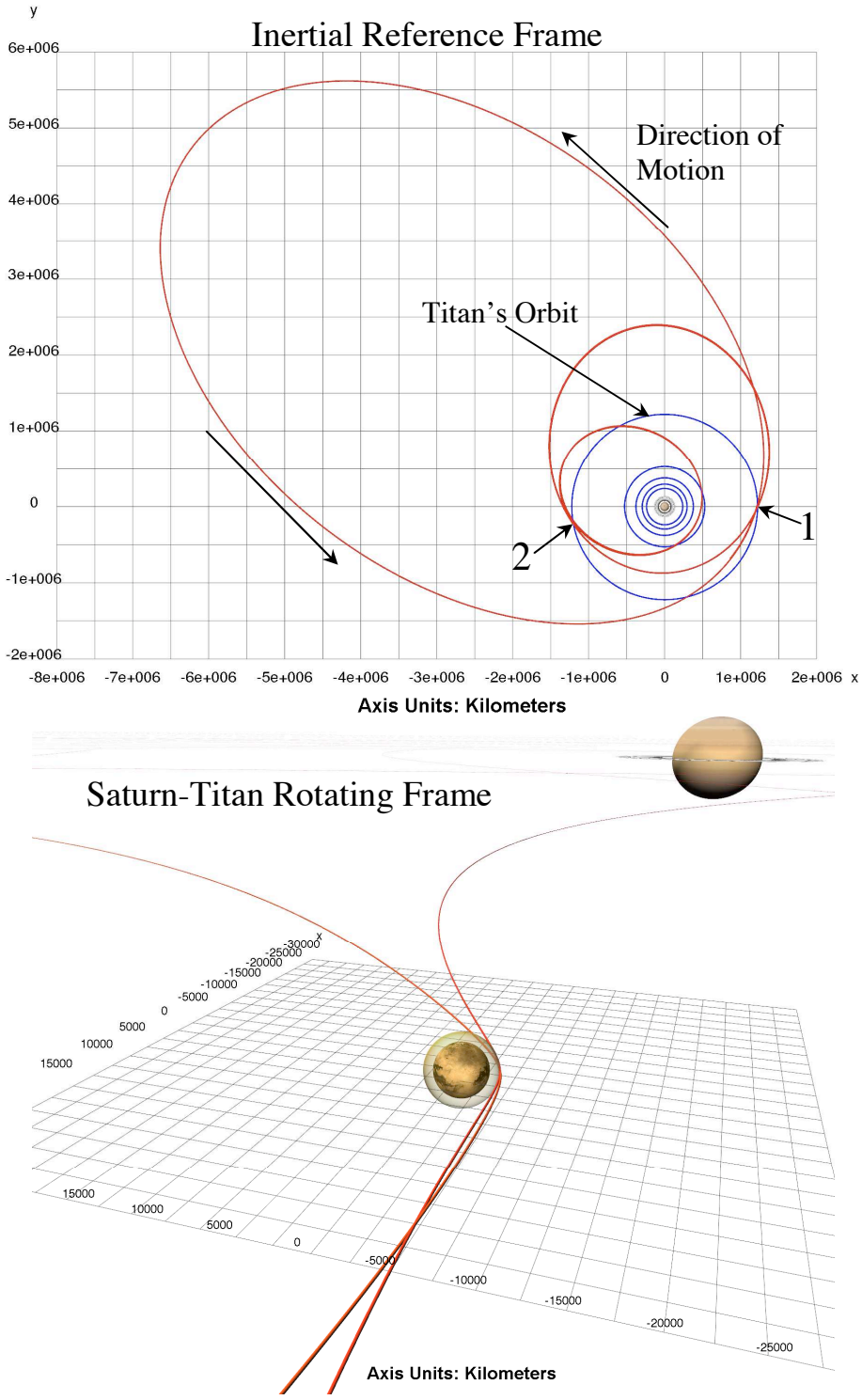

Figure 5.14 Inertial and rotating frame views of the first two Titan flybys involved in the sequence of six Titan flybys and one Dione flyby. Numeric labels denote Titan flyby locations and flyby order.

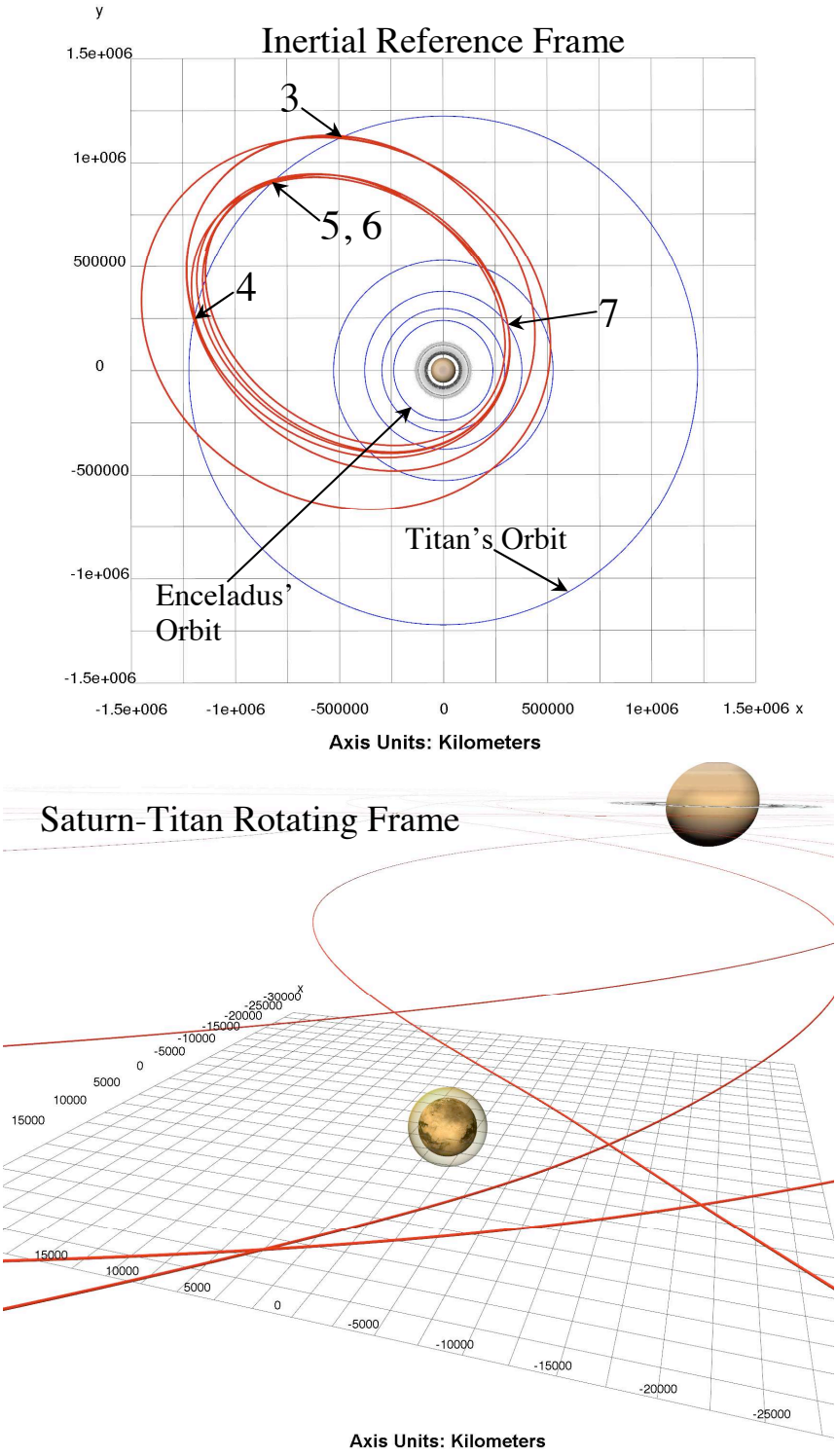

Figure 5.15 Inertial view and Saturn-Titan rotating frame views of the final four Titan flybys involved in the sequence of six Titan flybys and one Dione flyby. Numeric labels denote Titan and Dione flyby locations and the flyby order.

spacecraft orbit in Figure 5.15 are r_p = 488,910.5 km and r_a = 1,527,845.5 km. From this orbit, an argument of periapsis equal to ω_o = 273.8827955° produces four additional Titan flybys and a single Dione flyby. To be more accurate, following the two flybys in Figure 5.14, *three* additional Titan flybys and a single Dione flybys are targeted, in that order. However, prior to the final Dione flyby, the spacecraft experiences an untargeted close flyby behind Titan that actually produces a small undesired increase in apokrone distance, though the flyby sequence ultimately places the spacecraft on an orbit with perikrone very near the orbit of Enceladus.

In Figures 5.14 and 5.15, the relative sizes of the orbits of Enceladus, Tethys, Dione, Rhea, and Titan appear in the inertial frame as blue rings of proper radius, and the orbital motion of the spacecraft is plotted in red in both the inertial and Saturn-Titan rotating frames. The orbits of all six moons and the spacecraft in Figures 5.14 and 5.15 are prograde, that is, they travel in counterclockwise motion in the inertial reference frame (rotation in the +*z* direction). Titan's atmosphere is depicted in the rotating frame views of Figures 5.14 and 5.15 as the transparent sphere surrounding the moon, and the first two flybys in Figure 5.14 visibly graze the atmosphere of the moon. In both figures, arrows are used to identify the locations of the first six flybys of Titan and the final seventh flyby of Dione in the inertial reference frame.

Variations in both the perikrone and apokrone distances of the spacecraft orbit, as well as the spacecraft-Saturn separation distance, are plotted in Figure 5.16. In Figure 5.16, the orbital characteristics associated with the initial two Titan flybys are summarized on the left, and the remaining five flybys are plotted on the right. In both plots from Figure 5.16, red lines mark the temporal location of each of the seven flybys. Note that each flyby in Figure 5.16 is associated with a sharp decrease in the perikrone and apokrone distances of the orbit, with the notable exception of the final flyby of Dione, which decreases the apokrone distance without a comparable decline in perikrone distance. The qualitative difference between the Titan and Dione flybys results from the fact that the ΔV_{eq} associated with the Titan flybys is applied near apokrone of the

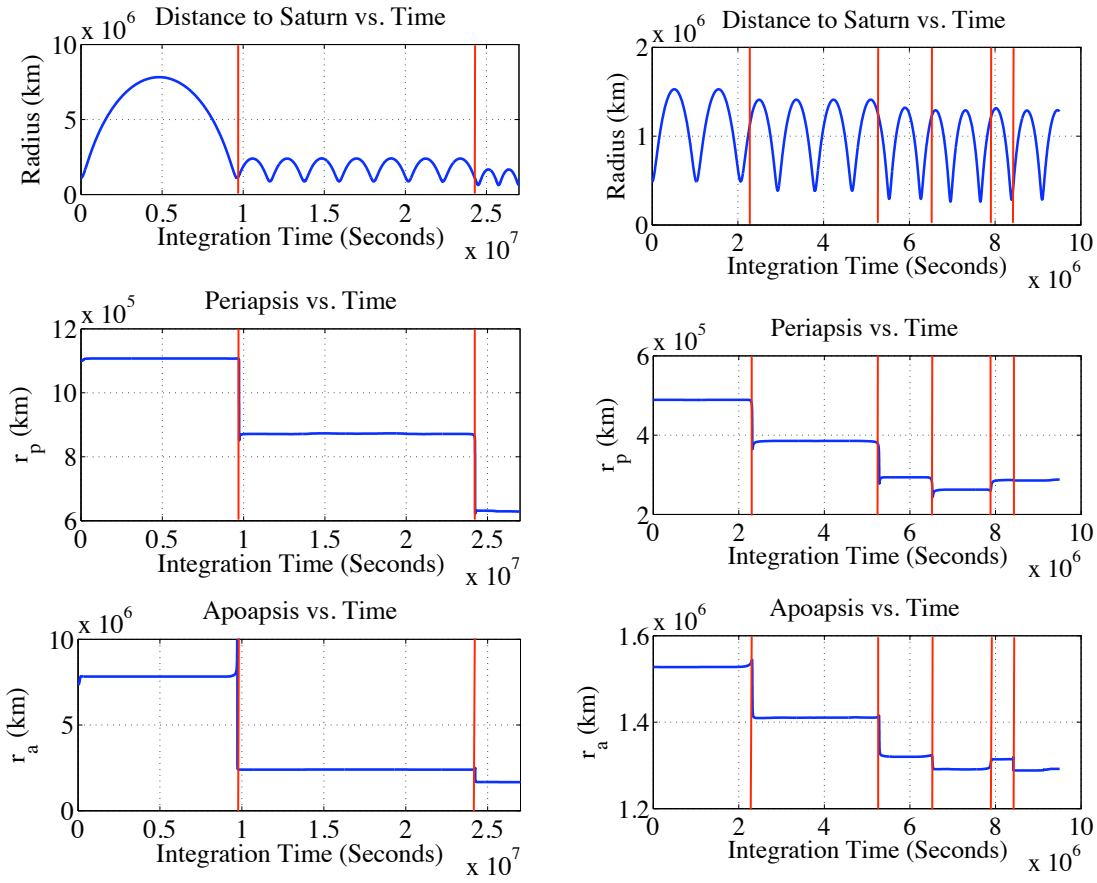

Figure 5.16 Variations in the orbital elements of a spacecraft's orbit during the sequence of six Titan and one Dione gravity-assist flybys. The first two Titan flybys on the left and the remaining four Titan flybys and sole Dione flyby on the right.

spacecraft orbit, while the Dione flyby occurs relatively close to the perikrone point along the orbit of the spacecraft.

To complete the entire sequence of seven flybys requires a time-of-flight of at least 266 days, following the first Titan flybys. The dimensions of the final spacecraft orbit at the conclusion of all seven flybys are $r_p \approx 285{,}000$ km and $r_a \approx 1{,}288{,}000$ km. Therefore, the overall reduction in orbit size as a consequence of the seven flybys corresponds to a decrease in apokrone distance of ~6,046,000 km and a decrease in perikrone distance of ~815,000 km. To accomplish this same change in orbit energy through a two-burn scheme of propulsive maneuvers – where a maneuver is first implemented at perikrone in the original orbit to reduce the apokrone distance, and a

second maneuver is performed at the apokrone of the new orbit to reduce the perikrone distance – requires an equivalent ΔV_{eq} of 3.9 km/s. Recall that the Cassini mission included a propellant budget for the entirety of its prime mission of less than 2 km/s [51], so a reduction in the required propulsive ΔV amounting to 3.9 km/s is quite substantial. By using gravity-assist flybys to reduce the propulsive ΔV requirements for a spacecraft transferring 'down' to Enceladus, it is not necessary for the mass of the spacecraft to be augmented by such a large amount of propellant mass. An increase in the ΔV_{eq} (i.e., a decrease in the required propulsive ΔV) is gained only at the cost of an increase in the time-of-flight associated with the trajectory, since the transfer from the large Saturnian orbit to the final, smaller orbit after the seventh flyby can be accomplished ballistically.

Table 5.3 Approximate propulsive ΔV_{eq} associated with transferring the spacecraft from an orbit sized $r_p \approx 285{,}000$ km, $r_a \approx 1{,}288{,}000$ to a desired final orbit.

Desired Final Spacecraft Orbit	Required ΔV_{eq} (km/s)
Enceladus Orbit	4.38
2:3 Resonant Orbit	2.97
5:8 Resonant Orbit	2.79

The final spacecraft orbit following the seven flybys in Figures 5.14 and 5.15 does not deliver the spacecraft to precisely the orbital energy of Enceladus. Instead, a propulsive maneuver or additional flybys of Saturn's inner moons are required to reduce or eliminate the remaining relative velocity between Enceladus and the spacecraft as it approaches the orbit of Enceladus. The required additional propellant cost to transfer a spacecraft to three final spacecraft orbit options appears in Table 5.3. The results in Table 5.3 are based on the approximate propellant costs to apply a single maneuver near perikrone in the conic model to reduce the spacecraft velocity at perikrone ($r_p \approx 285{,}000$ km) to the speed that matches the perikrone velocity along the desired final orbit. As listed in Table 5.3, an additional ΔV_{eq} of 4.38 km/s is required, beyond the effects of the seven gravity-assist flybys, to insert the spacecraft into a circular Enceladus orbit.

However, the cost to transfer the spacecraft to the 5:8 or 2:3 resonant orbits depicted Figures 4.15 and 4.16 are smaller than the cost to transfer the spacecraft to an Enceladus orbit; the cost to transfer to the 5:8 resonant orbits is just 2.79 km/s, compared to the 4.38 km/s cost to circularize the orbit. Thus, while the specific sequence of gravity-assist flybys depicted in Figures 5.14 and 5.15 does not complete the transfer to Enceladus, this relatively simple flyby sequence accomplishes a large fraction of the required velocity reduction necessary to arrive at the orbital energy that is required to utilize the Enceladus orbits from Chapter 3 or the mean motion resonant orbits in Chapter 4.

5.3.6 Advantages and Disadvantages of the Flyby Sequence Design Algorithm

The flyby sequence design algorithm developed in this analysis possesses several advantageous features. First, the optimization algorithm requires minimal user-supplied information. The optimization algorithm does not require a reference solution, user supplied Saturnian moon encounter dates/times, or prior knowledge of the instantaneous Keplarian orbit of the spacecraft either before or after the flyby. This flyby trajectory design algorithm also offers the option for a high level of user interactivity. In this analysis, the algorithm is generally not provided a specific list of flyby targets prior to the construction of the flyby sequence. Instead, a flyby trajectory returned by the optimization algorithm is propagated beyond the simulation time associated with the known flyby, and the rotating reference frames of each of the five flyby moons are inspected to determine whether the natural dynamics of the Saturnian system result in any future close approaches without additional targeting. This method of identifying potential flyby targets, based purely on the natural dynamics of the Saturnian moons and spacecraft, is possible because the algorithm is sufficiently flexible to allow the user to select flyby targets during the course of the design process.

Because this trajectory design algorithm accomplishes design directly in the six-body model, the solutions returned by the algorithm are of higher fidelity. Although the Saturnian moons are assumed to move in circular orbits around Saturn in the six-body dynamical model, the optimization algorithm does not depend on this assumption.

Consequently, it is relatively easy to add the eccentricity of the orbits for each of the moons, and to incorporate the physical true anomaly of each moon from an ephemeris file to further increase the accuracy of the results. However, the trajectory design algorithm is formulated based on the assumption that the orbits of the five moons are coplanar. Note that if even small displacements in z position are introduced into the model for either the orbits of the moons or the spacecraft, then targeting flybys of Saturnian moons is generally not possible through the minimization of a single initial orbital parameter, ω_o, since there is additional dependence on orbital inclination.

Although there are several insightful and useful features in the trajectory design algorithm developed in this analysis, the method also includes a number of limitations. The most serious issue associated with the algorithm is the sensitivity of spacecraft trajectories with multiple flybys to small variations in ω_o. Of course, this characteristic frequently surfaces in numerical algorithms applied to nonlinear problems in astrodynamics. However, building sequences of flybys that include more than six or seven flybys is difficult as the level of variation in ω_o approaches the numerical level of precision. Modification of the algorithm to a process based on multiple shooting could improve the performance.

Another limitation of this method of designing flyby trajectories is the computational inefficiency of the algorithm as the duration of numeric propagations increases. Using the optimization routine to identify a single flyby trajectory only requires a few seconds to complete. However, as additional flybys are targeted, the duration of the numerical integration steps during each objective function evaluation increases. Unfortunately, the runtime of the algorithm increases as additional flybys are targeted, both because each function evaluation requires a longer numerical integration, and as the sensitivity of the problem increases, the SQP algorithm requires additional iterations to converge on a solution. The computational expense associated with this trajectory design algorithm would be less of a disadvantage if the trajectory design method were *not* so interactive. Generally, it is inconvenient for a user to interact with the algorithm, if adding a single additional flyby requires several minutes to determine a feasible solution.

6. CONCLUSIONS

6.1 Summary

The problem of developing trajectories to support a mission to Enceladus is examined. In particular, the investigation is focused on spacecraft motion once it has been delivered to the Saturnian system. The transfer from the vicinity of Titan to Enceladus is considered using multi-body dynamical models of the Saturnian system. This investigation includes an overview of several dynamical regimes encountered by the spacecraft. Several multi-body mission design tools are used in this investigation and the historical development of multi-body dynamical models is discussed. The derivation of many of the mathematical tools to compute periodic solutions in the CR3BP is presented. Mean motion orbital resonance and the mechanics of gravity-assist flyby trajectories are also examined to facilitate the application of both dynamical phenomena to mission design in the Saturnian system.

With an appropriate level of dynamical and mathematical background, trajectories in the vicinity of Enceladus are examined within the context of the Saturn-Enceladus circular restricted three-body problem. With this dynamical model, a number of periodic orbits in the vicinity of Enceladus are identified, including families of Lagrange point orbits known as Lyapunov and halo orbits, as well as other periodic orbits of Enceladus. The strong perturbing influence of Saturn on Enceladus orbits is demonstrated through several simulations of initially circular orbits around the moon.

As an alternative to entering an orbit around Enceladus, several spacecraft orbits that share a mean motion resonance with Enceladus are generated that offer relatively low velocity flyby reconnaissance of the moon. Families of resonant orbits in the Saturn-Enceladus CR3BP are presented, as well as examples of resonant orbits in the Saturn-

Dione CR3BP that include periodic close flybys of both Dione and Enceladus. Resonant orbits generated in the Saturn-Dione CR3BP are propagated in a six-body dynamical model of the Saturnian system to examine the sensitivity of the orbits in a higher fidelity model and the characteristics of quasi-periodic resonant trajectories that pass near both Dione and Enceladus.

An algorithm for designing sequences of gravity-assist flyby trajectories in a multi-body model of the Saturnian system is developed. The trajectory design algorithm uses a constrained local optimization routine to adjust a single design variable associated with the initial spacecraft state that results in a gravity-assist flyby of a user-defined target moon. The purpose of this algorithm is the reduction of the orbital energy associated with a spacecraft's orbit to a level that more closely matches the energy level of Enceladus' orbit around Saturn. Sequences of flybys are constructed using this optimization algorithm.

6.2 Recommendations for Future Work

This investigation serves as an overview of the Enceladus transfer problem, and as such, several aspects of this analysis merit a more detailed examination. On the topic of orbiting Enceladus, the most significant simplifying assumption in using the CR3BP to model the dynamical system is neglecting the perturbing influence of Saturn's oblate gravity field as well as the gravity harmonics of Enceladus. Saturn in the most oblate planet in our solar system and, as such, the J2 component of Saturn's gravity field is fully expected to generate a significant perturbing influence within the Saturnian system. Enceladus also possesses a non-spherical gravitational potential. For this reason, it remains of interest to examine the orbits around Enceladus in the CR3BP including the impact of the additional perturbing influences of the full gravity harmonics of Saturn and Enceladus. With a more physically realistic model of the gravity fields of both Enceladus and Saturn, the maximum feasible orbital inclination for a science orbit can be further probed and an understanding of the stability of the Enceladus science orbits can be expanded.

The resonant orbits in this investigation periodically or quasi-periodically encounter Enceladus without substantial changes to the spacecraft orbit. However, it is also possible to use gravity-assist flybys to switch orbital resonances with the flyby body. Although not explored in this investigation, it would be a worthwhile extension of the resonant orbit analysis. Neither the stability nor instability of mean motion resonant orbits are examined in this analysis, however, previous work has demonstrated that by applying dynamical systems theory to the Jupiter-Europa system, it is possible to achieve ballistic capture into a Europa orbit from an orbit in mean motion resonance with Europa [25-27]. Applying these techniques [25-27] to the Saturnian system in general, and to the resonant orbits in the Saturn-Enceladus system in particular, would constitute a particularly meaningful extension of this investigation.

As currently formulated, the flyby sequence design algorithm developed in this investigation is limited in computing extensive sequences of flybys of the Saturnian moons. The utility of the optimization-based algorithm in designing flyby trajectories is demonstrated in this investigation. However, the optimization problem in mission design can be reformulated to address some of the limitations. Alternative strategies are warranted to respond to the most challenging aspects of the problem: the sensitivity of the problem to small variations in the design variable, and the inefficiency of the optimization process for long sequences of flybys.

6.3 Concluding Remarks

As a result of this investigation, numerous potential solutions to the Enceladus transfer problem are illuminated. These solutions range from Lagrange point orbits and perturbed circular orbits around Enceladus that could be used for global mapping of the moon's surface, to orbits around Saturn that share mean motion resonances with both Dione and Enceladus, thus providing close flybys of each moon at relatively low velocity and at periodic intervals. In addition to the Enceladus science orbit options, gravity-assist flyby sequences to reduce the orbital energy of a spacecraft relative to Saturn are also introduced, as well as a technique to identify these solutions. While, the particular

solutions identified in this analysis result from an examination of the problem strictly from a multi-body perspective, these orbits and trajectories are solutions to the very real physical problem of sending a spacecraft to Enceladus, and the solutions are ultimately independent of the model use. However, this investigation also offers *dynamical* insight into the problem of transferring a spacecraft to Enceladus; this addition to the understanding of the multi-body nature of the Saturnian system goes beyond the identification of point solutions to the Enceladus transfer problem. Ultimately, the dynamical insight is a first step in the open-ended dynamical problem of multi-body mission design in the Saturnian system.

LIST OF REFERENCES

LIST OF REFERENCES

[1] A. J. Verbiscer, R. G. French, and C. A. McGhee, "The Opposition Surge of Enceladus: HST Observations 338-1022 nm," *Icaraus*, Vol. 173, pp. 66-83, 2005.

[2] D. P. Cruikshank, "Near-Infrared Studies of the Satellites of Saturn and Uranus," *Icaraus*, Vol. 41, pp. 246-258, 1980.

[3] C. C. Porco, P. Helfenstein, P. C. Thomas, A. P. Ingersoll, J. Wisdom, R. West, G. Neukum, T. Denk, R. Wagner, T. Roatsch, S. Kieffer, E. Turtle, A. McEwen, T. V. Johnson, J. Rathbun, J. Veverka, D. Wilson, J. Perry, J. Spitale, A. Brahic, J. A. Burns, A. D. DelGenio, L. Dones, C. D. Murray, and S. Squyres, "Cassini Observes the Active South Pole of Enceladus," *Science*, Vol. 311, No. 1393, pp. 692-710, August 2006.

[4] A. Razzaghi, A. A. Simon-Miller, D. A. Di Pietro, and J. R. Spencer, "Enceladus Flagship Mission Concept Study," Prepared for NASA's Planetary Science Division, August 2007.

[5] K. Reh, "Titan and Enceladus $1B Mission Feasibility Study Report," JPL Document: D-37401 B, Prepared for NASA's Planetary Science Division, January 2007.

[6] D. Harper and D. B. Taylor, "The Orbits of the Major Satellites of Saturn," *Astronomy and Astrophysics*, Vol. 268, No. 1, pp. 326-349, 1993.

[7] V. Szebehely and H. Mark, *Adventures in Celestial Mechanics*, John Wiley and Sons, Inc., New York, New York, second edition, 1998.

[8] J. Barrow-Green, *Poincaré and the Three Body Problem*, Vol. 11 of History of Mathematics. Providence, Rhode Island: American Mathematical Society, 1997.

[9] V. Szebehely, *Theory of Orbits: The Restricted Problem of Three Bodies*, Academic Press, Inc., New York, New York, 1967.

[10] H. Poincaré, *Les Méthodes Nouvelles de la Mécanique Celeste*, Vol II, Paris, Gauthier-Villars, 1893.

[11] K. C. Howell, "Families of Orbits in the Vicinity of the Collinear Libration Points," *Journal of the Astronautical Sciences*, Vol. 49, No. 1, pp. 107-125, January-March 2001.

[12] R. W. Farquhar and A. A. Kamel, "Quasi-Periodic Orbits About the Translunar Libration Point," *Celestial Mechanics*, Vol. 7, pp. 458-473, 1973.

[13] K. C. Howell, "Three-Dimensional, Periodic, 'Halo' Orbits," *Celestial Mechanics*, Vol. 32, pp. 53-71, 1984.

[14] R. W. Farquhar, "The Control and Use of Libration-Point Satellites," NASA TR R-346, 1970.

[15] J. V. Breakwell and J. V. Brown, "The 'Halo' Family of 3-Dimensional Periodic Orbits in the Earth-Moon Restricted 3-Body Problem," *Celestial Mechanics*, Vol. 20, pp. 389-404, 1979.

[16] R. W. Farquhar, "The Flight of ISEE-3/ICE: Origins, Mission History, and a Legacy," *Journal of the Astronautical Sciences*, Vol. 49, No. 1, pp. 23-73, January-March 2001.

[17] H. Franz, P. Sharer, K. Ogilvie, and M. Desch, "WIND Nominal Mission Performance and Extended Mission Design," *Journal of the Astronautical Sciences*, Vol. 49, No. 1, pp. 145-167, January 2001; Paper AIAA 98-4467, AIAA/AAS Astrodynamics Specialist Conference, Boston, Massachusetts, 10-12 August 1998.

[18] V. Domingo, B. Fleck, and A. I. Poland, "The SOHO Mission: An Overview," *Solar Physics*, Vol. 162, pp. 1-37, 1995.

[19] P. Sharer and T. Harrington, "Trajectory Optimization for the ACE Halo Orbit Mission," Paper AAS 96-3601, AAS/AIAA Astrodynamics Specialist Conference, San Diego, California, 29-31 July 1996.

[20] C. L. Bennett, M. Bay, M. Halpern, G. Hinshaw, C. Jackson, N. Jarosik, A. Kogut, M. Limon, S. S. Meyer, L. Page, D. N. Spergel, G. S. Tucker, D. T. Wilkinson, E. Wollack, and E. L. Wright, "The Microwave Anisotropy Probe Mission," *Astrophysical Journal*, Vol. 583, pp. 1-23, January 2003.

[21] M. Lo, B. G. Williams, W. E. Bollman, D. Han, Y. Hahn, J. L. Bell, E. A. Hirst, R. A. Corwin, P. E. Hong, K. C. Howell, B. Barden, R. Wilson, "Genesis Mission Design," Paper 98-4468, AIAA/AAS Astrodynamics Specialist Conference, Boston, Massachusetts, 10-12 August 1998.

[22] D. W. Dunham and R. W. Farquhar, "Libration Point Missions, 1978-2002," *Proceedings of the Conference Libration Point Orbits and Applications*, Aiguablava, Spain, G. Gomez, M. W. Lo and J. J. Masdemont (editors), pp. 45-73, 10-14 June 2002.

[23] K. Ogata, *Modern Control Engineering*, Prentice Hall, Inc., Upper Saddle River, New Jersey, fourth edition, 2002.

[24] A. E. Roy and W. M. Ovenden, "On the Occurrence of Commensurable Mean Motions in the Solar System, II. The Mirror Theorem," *Monthly Notices of the Royal Astronomical Society*, Vol. 115, pp. 296-309, January 1955.

[25] R. L. Anderson, "Low Thrust Trajectory Design for Resonant Flybys and Captures Using Invariant Manifolds," Ph.D. Thesis, University of Colorado, Boulder, Colorado, 2005.

[26] R. L. Anderson and M. W. Lo, "The Role of Invariant Manifolds in Low Thrust Trajectory Design (Part II)," Paper AAS 06-190, AAS/AIAA Astrodynamics Specialist Conference, Providence, Rhode Island, 16-19 August 2004.

[27] M. W. Lo, R. L. Anderson, T. Lam, and G. Whiffen, "The Role of Invariant Manifolds in Low Thrust Trajectory Design (Part III)," Paper AAS 06-190, AAS/AIAA Astrodynamics Specialist Conference, Tampa, Florida, 22-26 January 2006.

[28] Broucke, R. A., "The Celestial Mechanics of Gravity Assist," Paper AIAA 88-4220, August 1988.

[29] N. J. Strange and J. M. Longuski, "Graphical Method for Gravity-Assist Trajectory Design," *Journal of Spacecraft and Rockets*, Vol. 39, No. 1, pp. 9-15, February 2002.

[30] C. D. Murray and S. F. Dermott, *Solar System Dynamics*, Cambridge University Press, Cambridge, United Kingdom, 1999.

[31] J. M. Deerwester, "Jupiter Swingby Missions to the Outer Planets," *Journal of Spacecraft and Rockets*, Vol. 3, No. 10, pp. 1564-1567, October 1966.

[32] L. A. d'Amario, L. E. Bright, and A. A. Wolf, "Galileo Trajectory Design," *Space Science Review*, Vol. 60, pp. 23-78, 1992.

[33] E. J. Smith and R. G. Marsden, "Ulysses Observations from Pole-To-Pole: An Introduction," *Geophysical Research Letters*, Vol. 22, No. 23, pp. 3297-3300, 1995.

[34] F. Peralta and S. Flanagan, "Cassini Interplanetary Trajectory Design," *Control Engineering Practice*, Vol. 3, No. 11, pp. 1603-1610, 1995.

[35] A. A. Wolf and J. C. Smith, "Design of the Cassini Tour Trajectory in the Saturnian System," *Control Engineering Practice*, Vol. 3, No. 11, pp. 1611-1619, 1995.

[36] J. V. McAdams, D. W. Dunham, R. W. Farquhar, A. H. Taylor, and B. G. Williams, "Trajectory Design and Maneuver Strategy for the MESSENGER Mission to Mercury," *Journal of Spacecraft and Rockets*, Vol. 43, No. 5, pp. 1054-1064, October 2006.

[37] Y. Guo and R. W. Farquhar, "New Horizons Mission Design for the Pluto-Kuiper Belt Mission," Paper AAS 02-4722, AAS/AIAA Astrodynamics Specialist Conference, Monterey, California, 5-8 August 2002.

[38] J. N. Spitale, R. A. Jacobson, C. C. Porco, and W. N. Owen, Jr., "The Orbits of Saturn's Small Satellites Derived From Combined Historic and Cassini Imaging Observations," *Astronomical Journal*, Vol. 132, pp. 692-710, August 2006.

[39] R. A. Jacobson, "The Orbits of the Major Saturnian Satellites and Gravity Field of Saturn from Spacecraft and Earth-Based Observations," *Astronomical Journal*, Vol. 128, pp. 492-501, July 2004.

[40] C. Roddier, F. Roddier, J. E. Graves, and M. J. Northcott, "Discovery of an Arc of Particles Near Enceladus' Orbit: A Possible Key to the Origin of the E-Ring," *Icaraus*, Vol. 136, pp. 50-59, 1998.

[41] R. P. Russell and M. Lara, "On the Design of an Enceladus Science Orbit," Paper AAS 08-7072, AAS/AIAA Astrodynamics Specialist Conference, Honolulu, Hawaii, 18-21 August 2008.

[42] R. P. Russell and T. Lam, "Designing Capture Trajectories to Unstable Periodic Orbits Around Europa," Paper AAS 06-189, AAS/AIAA Space Flight Mechanics Meeting, Tampa, Florida, 22-26 January 2006.

[43] T. S. Sweetser, R. Maddock, J. Johannesen, J. Bell, P. Penzo, A. Wolf, S. Williams, S. Matousek, and S. Weinstein, "Trajectory Design for a Europa Orbiter Mission: A Plethora of Astrodynamic Challenges," AAS Paper 97-174, AAS/AIAA Space Flight Mechanics Meeting, Huntsville, Alabama, 9-12 February 1997.

[44] C. Uphoff, P. H. Roberts, and L. D. Friedman, "Orbit Design Concepts for Jupiter Orbiter Missions," *Journal of Spacecraft and Rockets*, Vol. 13, No. 6, pp. 348-355, 1976.

[45] G. J. Whiffen, "An Investigation of a Jupiter Galilean Moon Orbiter Trajectory," Paper AAS 03-544, AAS/AIAA Astrodynamics Specialist Conference, Big Sky, Montana, 3-7 August 2003.

[46] S. D. Ross, W. S. Koon, M. W. Lo, and J. E. Marsden, "Design of a Multi-Moon Orbiter," Paper AAS 03-143, AAS/AIAA Space Flight Mechanics Meeting, Ponce, Puerto Rico, 9-13 February 2003.

[47] R. P. Russell and N. J. Strange, "Planetary Moon Cycler Trajectories," Paper AAS 07-118, AAS/AIAA Space Flight Mechanics Meeting, Sedona, Arizona, 28 January – 1 February 2007.

[48] R. P. Russell and C. A. Ocampo, "Systematic Method for Constructing Earth-Mars Cyclers Using Free-Return Trajectories," *Journal of Guidance, Control, and Dynamics*, Vol. 27, No. 3, pp. 321-335, June 2004.

[49] R. P. Russell and C. A. Ocampo, "Geometric Analysis of Free-Return Trajectories Following a Gravity-Assisted Flyby," *Journal of Spacecraft and Rockets*, Vol. 42, No. 1, pp. 138-151, February 2005.

[50] D. V. Byrnes, J. M. Longuski, and B. Aldrin, "Cycler Orbit Between Earth and Mars," *Journal of Spacecraft and Rockets*, Vol. 30, No. 3, pp.334-336, 1993.

[51] T. Burk, "Attitude Control Performance During Cassini Trajectory Correction Maneuvers," *Proceedings of the AIAA Guidance, Navigation, and Control Conference*, San Francisco, California, 15-18 August 2005.

[52] L. Spilker, (Ed.), "Passage to a Ringed World," NASA Report: SP-533, October 1997.

[53] D. V. Byrnes and L. E. Bright, "Design of High-Accuracy Multiple Flyby Trajectories Using Constrained Optimization," Paper AAS 95-307, AAS/AIAA Astrodynamics Specialist Conference, Halifax, Nova Scotia, Canada, 14-17 August 1995.

[54] J. S. Arora, *Introduction to Optimum Design*, Elsevier Inc., London, United Kingdom, 2004.